Engineering and the Environment

UNIVERSITY OF Southampton

Design Report

FEEG6013 Group Design Project

37

Spacecraft Propulsion Systems

Design, Manufacture and Test of a Microwave Neutraliser for Ion Thruster Operations

Electric propulsion for spacecraft offers greater efficiency and requires less propellant than conventional chemical rocket thrusters. Electric thrusters have a wide range of applications, such as long-duration orbital manoeuvres, interplanetary transfers, and satellite station keeping. Gridded ion thrusters produce thrust by ionising propellant and using electric fields to accelerate the ions. However, they require an additional component, a neutraliser, to prevent the build-up of charge on the thruster.

The aim of this project was to develop, manufacture, and test a neutraliser for XSEPT, the gridded ion thruster project under development by the University of Southampton. Secondary objectives were to use additive manufacturing to produce components where possible, and to test various designs of the neutraliser components.

Both the thruster and the neutraliser operate using an innovative method known as Electron Cyclotron Resonance (ECR). This uses a tailored combination of microwaves and powerful magnetic fields to ionise the propellant. ECR has the potential to greatly increase the operational lifetime compared to traditional neutralisation methods. The project is the first European thruster to make use of ECR.

The design process involved using COMSOL Multiphysics to model the magnetic and electric fields in the neutraliser, Python scripts to characterise and predict the overall performance of the neutraliser, and ANSYS to perform thermal and structural analysis.

The neutraliser components have been entirely manufactured by the EDMC at the university, bar a heat-treatment process undertaken externally by Kepston Ltd. Several minor manufacturing tasks were performed by members of the GDP team.

Group Members:

ID Number	Name	ID Number	Name
26766841	Joseph Edwards	25939297	Marcus Collier-Wright
25917323	Richard Jones	26266415	Alessandro Arno
26878682	Sam Reeve	27495329	Wojciech Zakrzewski
26811006	Peter Turner	27019764	Maria Sevilla

Primary Supervisor: Dr Angelo Grubisic

Co-Supervisor: Dr Min Kwan Kim

Submitted on: 17/05/2018

The Design

This report documents the design process that was followed to design, construct and test a working Electron Cyclotron Resonance Neutraliser, for integration with a Microwave Gridded Ion Thruster.

The exploded render below shows each component of the Neutraliser design. Each component was developed using a range of analysis methods and simulations, depending on the role and requirements.

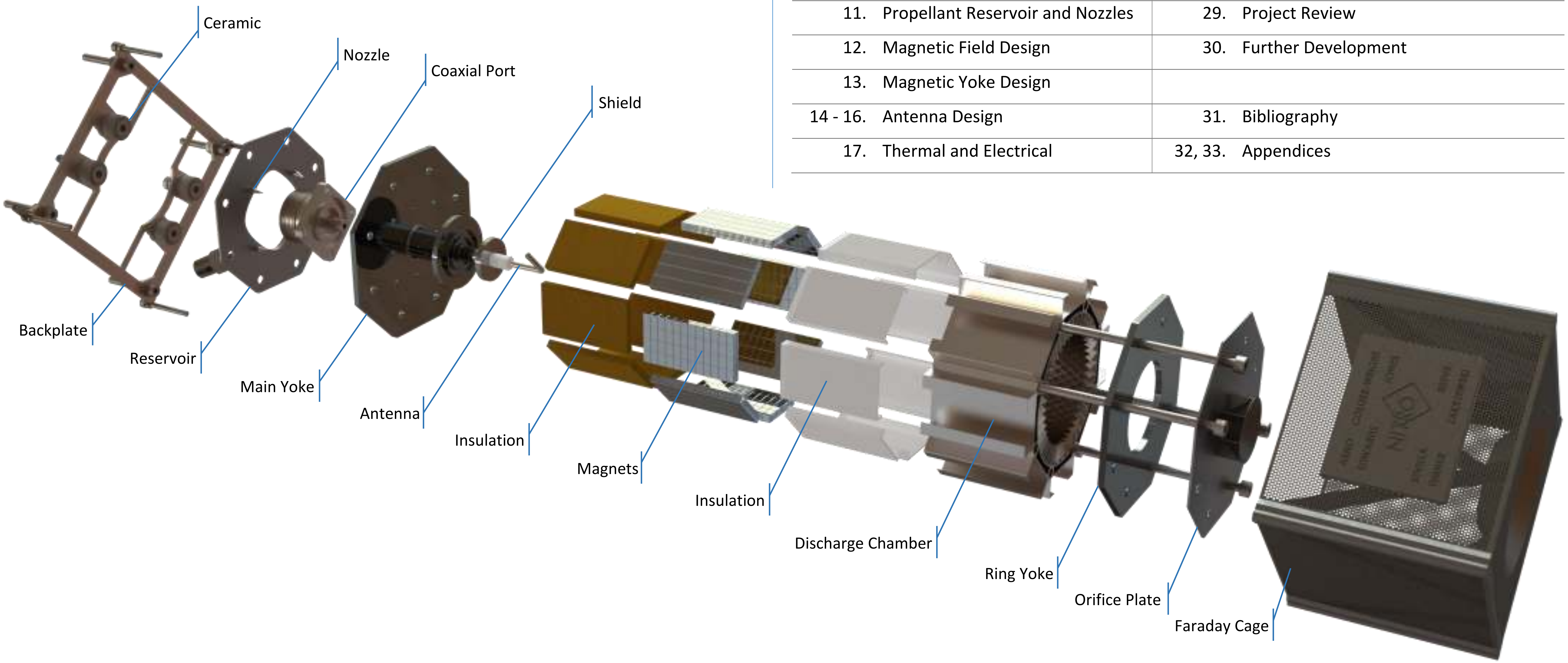

Project Introduction

To understand the role and requirement of a Neutraliser, its place within Spacecraft Propulsion needs to be understood.

History

Since orbit was achieved in 1957 by Sputnik 1, the first artificial satellite, the potential of the space environment has continued to be explored and developed. Major milestones in the earliest days include the first human spaceflight by Yuri Gagarin, the launch of probes venturing out of Earths sphere of influence, achieving flybys of Venus and Mars, and the historic Apollo missions which allowed humankind to set foot on another celestial body. In recent years, probes, rovers and landers have explored planets, moons, comets and asteroids, with Voyager 1 reaching interstellar space and leaving our solar system as recently as 2012. This exploration, and the information and data gained because of it has allowed insight into the very beginnings of our solar system and the formation of planet Earth. As the exploration of space grew, so too did the commercial market for platforms capable of providing a service from space. The possibility of long-distance communications via telecommunications satellite was popularised as far back as 1946 by Arthur C. Clarke [1]. In 1962 the first experimental telecoms satellite, Telstar 1, was launched by the National Aeronautics and Space Administration (NASA), capable of relaying television, telegraphs and telephone calls across the Atlantic. This was developed commercially soon after, with the first commercial telecoms satellite launched in 1965. Space offers the provision of an environment which has only just begun to be fully realised.

Spacecraft uses and requirements

Spacecraft have more use than simply crewed spaceflight, as the scope of use is vast and continually growing. Imaging, meteorology, internet and communication provision, navigation, remote sensing, atmospheric monitoring and astronomy are but a few of the services that are delivered frequently in everyday life. These services offer data and information that enhance and optimise operations for businesses, governments and individuals [2]. With the growth of a more connected society comes the requirement to facilitate more data, more information and more connection - all for a lower price. Many of the space-based services used in daily life utilise large scale platforms in a geostationary orbit (GEO). These are advantageous as they remain 'fixed' over a specific location above the Earth's surface, meaning that ground-based transmitters and receivers can remain fixed facing a specific direction at all times. This lowers the cost of access by lowering the cost of the ground segment to users, typified in the satellite dish receivers on found on many homes. Much of the cost is moved to the design, launch and operations of the satellite itself.

Spacecraft Propulsion

Launching a satellite to orbit is currently done by traditional chemical rocket propulsion. This can be found in several different forms, from the SpaceX Falcon 9 utilising liquid Oxygen and Kerosene [3], the Space Shuttle which combined liquid hydrogen and liquid oxygen to reach orbit in 6 minutes [4] and, at its most crude, the common firework. Chemical propulsion is currently the best way to reach space due to the high thrust available, however the total performance is limited by the energy released during typical combustion. Once in space, it is an inefficient method of propulsion because of the low specific impulse. Specific impulse (I_{SP}) is a measure of how effectively a rocket utilises propellant and is defined more accurately as the total impulse per unit propellant weight consumed. Chemical rockets are used because they are capable of very high impulse at the cost of a very high flow rate. Once in space, the requirement for high thrust is less pressing and instead focusses on reducing the total mass launched. Electric propulsion offers a highly efficient solution, capable of achieving enormous changes in velocity at the expense of a very small amount of propellant. Mass saving can bring the cost down significantly in launching a satellite, which passes on cost savings to the customer user base and opens new business possibilities in areas previously thought too expensive.

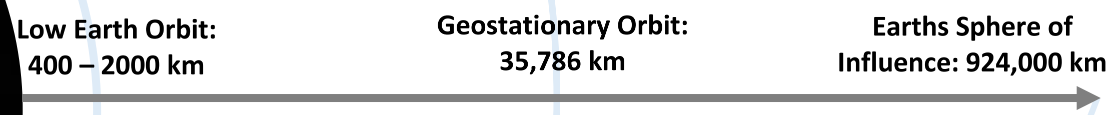

Figure 1 - A visual representation of possible orbits

Application of Electric Propulsion

Electric propulsion (EP) has only been fully embraced in recent years, with the first all-electric commercial satellite operational as of 2015 [5]. Satellites such as GOCE have used Ion propulsion systems in low earth orbit (LEO) [6] to assist in orbit profile and raising, geostationary platforms utilise electric propulsion to reach and maintain their designated orbit, whilst interplanetary probes such as Deep Space 1 and Dawn have used the high-velocity change available through the use of electric propulsion to visit asteroids outside of Earths sphere of influence, with the size of orbits visualised in Figure 1. Whilst each of these examples completes a different mission objective, electric propulsion was selected due to its performance in key areas. Recent geostationary satellites have achieved a structural-to-fuel mass percentage of 80%, compared to 40-60% of non-fully-electric, whilst NASA's NEXT ion thruster was tested for 51000 hours without failure, demonstrating the longevity of these thrusters [7]. Increasing the lifetime of geostationary platforms is of interest as it offers an extension in operational lifetime, increasing revenue for satellite operators and bringing down the overall cost. Fundamentally, electric propulsion offers better performance for medium to long duration missions, and in some cases is the only feasible option. It is better suited to unmanned probes over crewed spacecraft as human spaceflight requires higher thrust propulsion due to the shorter flight times and limited consumables available.

Application

As the use of EP increases, the focus remains on improving the performance of thrusters. There are several types varying in design and size. Gridded Ion Thrusters (GIT) offer the highest specific impulse and longest operation times, at a scale useful for satellite operations.

Gridded Ion Thrusters can be grouped into three types; Kaufman, RF and Microwave [8]. All produce thrust by ionising propellant, typically xenon, and accelerating the ions through a series of charged screens to high velocity. The differences in type are due to how the electrons are generated. The most common, the Kaufman type thruster, uses a hollow cathode filament to generate electrons within the discharge chamber and ionise the propellant. RF types use an oscillating electromagnetic field at a frequency coupled with the electrons to ionise the propellant. Finally, Microwave GIT's generate an electric field at microwave frequencies. This microwave energy induces resonant heating of electrons in the magnetic field, generating a plasma under the correct conditions. As all these thrusters generate thrust through the acceleration of positive ions away from the system, and without a form of neutralisation the thruster would build up a net negative charge. This would result in the emitted ion current being drawn back towards the thruster, reducing performance and damaging components.

Application of a Neutraliser in EP

The most common solution is to use an external neutraliser cathode to generate electrons outside of the thruster. This serves to neutralise the beam current and keep the system at net zero charge. However, hollow cathodes are limited in their life to around 28,000 hours [9] and as such cannot meet the requirements for lifetime demanded by the newest generation of GITs, and long duration missions [10], with research being undertaken into better quantifying the lifetime and failure. As a single point of failure, they are unpredictable and risk-heavy components. A microwave neutraliser offers an improved solution over traditional hollow cathodes, as it can be installed in pairing with a microwave gridded ion thruster as shown in Figure 3, requiring only propellant feed and microwave power between the two propulsion sub-systems. This system has been demonstrated on the Hayabusa mission, carried out by the Japanese Aerospace Exploration Agency, with each 'mu10' thruster producing 8mN of thrust [11]. A Microwave Gridded Ion Thruster (under the title 'XSEPT') is currently being developed by the University of Southampton, aiming to better the performance of the mu10. As part of this, there is the need to develop a suitable microwave neutraliser that integrates with the design and serves to meet the performance of XSEPT in its neutralisation current. Ignition marked the first successful test of an additively manufactured Neutraliser (Figure 2) intended for thruster operations in Europe. Whilst research and testing has been undertaken by NASA and JAXA separately, there is an opening for new research utilising novel design solutions made possible with the availability of 3D metal printing. By designing the neutraliser for manufacture using 3D printing, increasingly complex geometries can be achieved over traditional manufacturing techniques. The complex design required to facilitate Electron Cyclotron Resonance, the phenomenon that allows the microwave neutraliser to generate electrons, needs to balance magnetic field strength, electric field propagation, and physical design. 3D printing reduces manufacturing constraints, serving to reduce mass in certain components, improving performance through improved geometries, and reducing waste through efficient material usage.

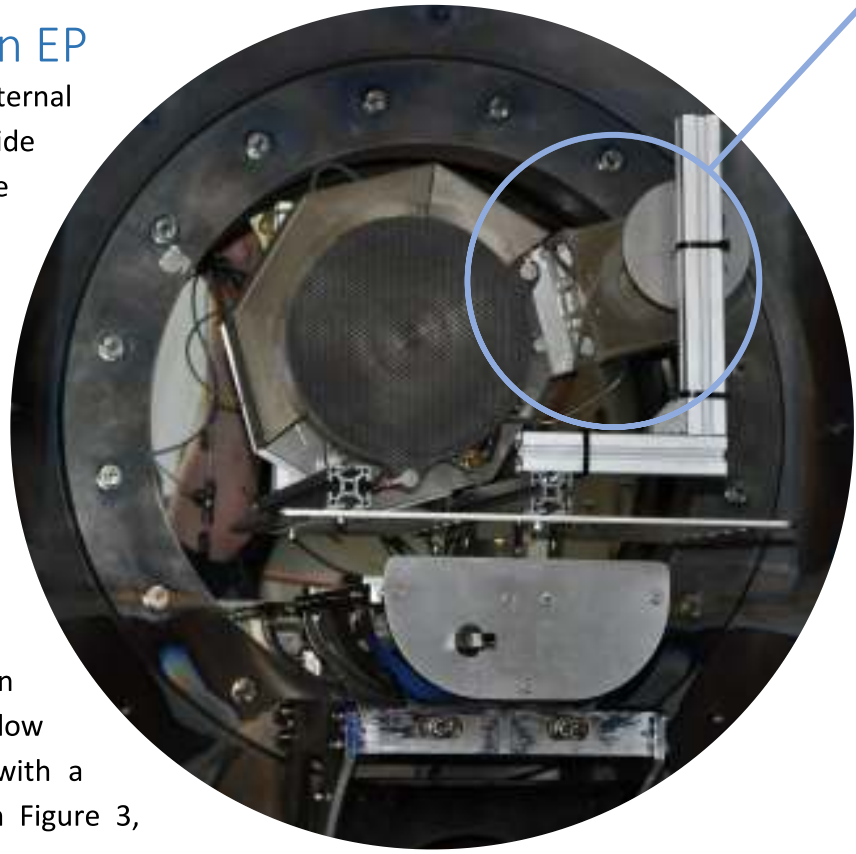

Figure 3 - The Thruster and Neutraliser assembly ready for testing

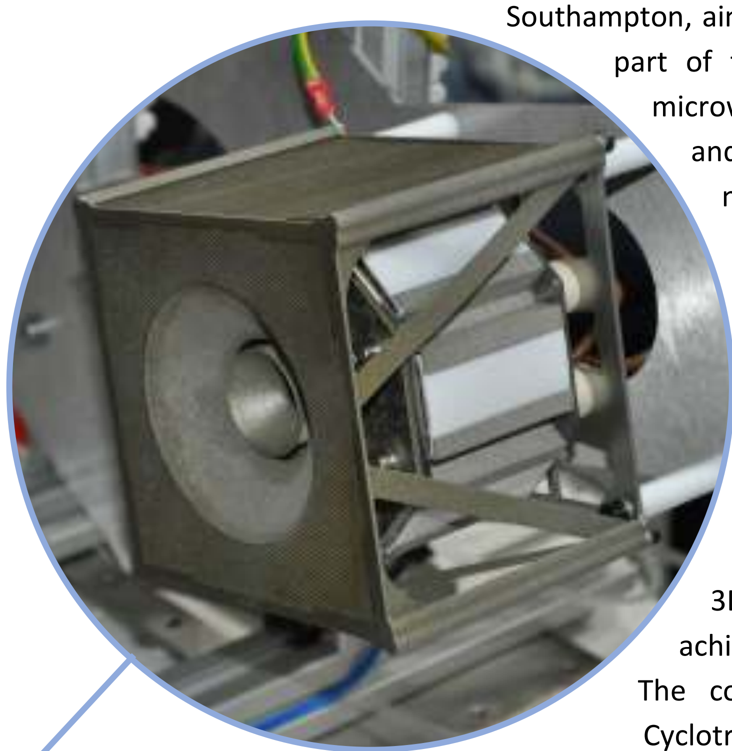

Figure 2 - Neutraliser attached to the test plate

What this can change

Most current thruster types use dated heritage designs that, whilst have demonstrated their reliability, do not take advantage of updated designs and manufacturing techniques. The University of Southampton is well placed to develop novel designs, facilitating improved performance and reduced costs over traditional thruster designs, through the manufacturing and testing facilities available. The long-term goal of this is to achieve direct integration into the design of a low-cost, long-endurance propulsion system for a geostationary telecommunications platform, and set the University of Southampton apart in its development of innovative solutions for spacecraft propulsion. Geostationary satellites require a minimum of 50 meters per second of velocity change (or delta-V) per year to account for Luni-Solar perturbations alone, added to the Earth triaxiality perturbation, and any additional station keeping duties [12]. Newer platforms built as fully software-defined spacecraft have the ability to change their coverage remotely [13], which offers the possibility of selling on a satellite in orbit. Moving the satellites' coverage location across large distances would require a shift in orbital position, and further provision of delta-V. The total delta-V available defines the lifetime of a satellite. The provision of a long-life propulsion system offers the potential to extend operational lifetimes beyond what is currently possible. A Microwave Gridded Ion Thruster and Neutraliser offer a long-term propulsion solution for future satellites.

What is ECR and why use it?

The primary failure mechanism in existing Ion Thrusters and Neutralisers is the failure of Hollow Cathodes in both major components, as hollow cathode failure can occur after long-term operation due to physical erosion of the internal channel. Such behaviour limits typical Ion thruster cathodes to a life of around 28,000 hours which is insufficient for missions requiring more than three years of continuous operation [9]. Using Electron Cyclotron Resonance (ECR) as an alternative method for electron production allows for electrodeless plasma production through the combination of matched Magnetic and Electromagnetic Fields, resulting in the elimination of the hollow cathode. The removal of the hollow cathode also results in other simplifications, as a cathode heater and corresponding power supply are no longer needed. These components are replaced by one microwave generator which can be used for both the main thruster and the neutraliser [14].

Electron Cyclotron Resonance is the process by which electrons absorb energy from an electromagnetic field. In this case, a 2.45GHz Microwave generator was used, as this is the frequency being used by the XSEPT Thruster and integration was a key aim. Resonance occurs when this frequency matches with the cyclotron frequency of the electrons trapped in a permanent magnetic field. Equating the angular frequency with the electron cyclotron frequency through the following equation shows that our resonant magnetic field strength is fixed at 0.0875 T.

$$\omega = 2\pi f = \frac{eB}{m_e}$$

$f = Frequency\ of\ Microwave\ Discharge$
$B = Magnetic\ Field\ Strength$
$e = Elementary\ charge$
$m_e = electron\ Mass$

When free electrons are subjected to a perpendicular magnetic field, they follow a circular motion about the magnetic field lines defined by the Larmor radius, in accordance with Fleming's Left-Hand Rule [15]. This electron can follow a helical motion if it possesses a velocity component along the magnetic field line, as shown in Figure 4. By placing magnetic yokes at either end of these field lines to increase the strength we can create a magnetic mirror to trap the electrons by reflecting them back along the field lines in the opposite direction. For free electrons in regions where the magnetic field strength equals 0.0875 T, the gyration period is synchronous with the frequency of the alternating microwave discharge, causing resonance. This process of resonance continuously increases the kinetic energy of the electrons in these regions, to a point where they are capable of ionising the propellant. These are known as Primary Electrons.

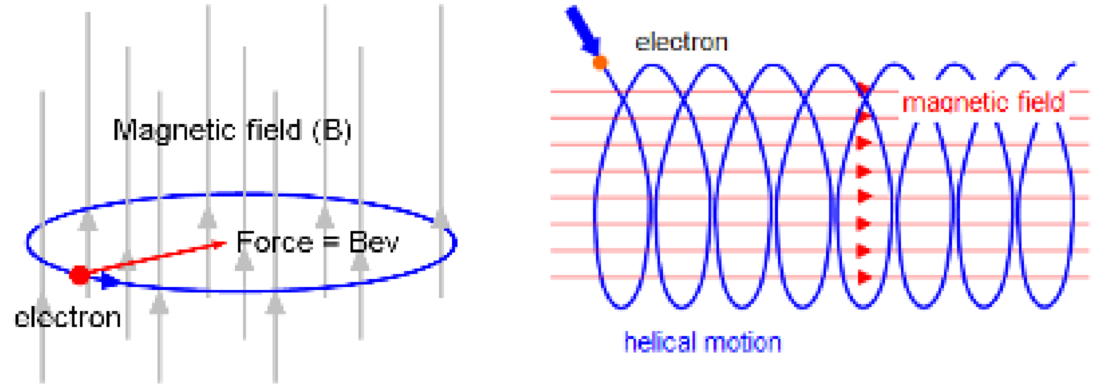

Figure 4 - Motion of free electrons in a perpendicular magnetic field [15]

As these high energy free electrons travel between the end of the magnetic mirror they will collide with neutral propellant atoms. As the kinetic energy of the electron is greater than the primary ionisation energy of the propellant, an ionisation event can occur, knocking one electron off the neutral atom.

The original energy of the Primary Electron prior to the ionisation process is now split between the two electrons involved in the ionisation process (the original high energy primary electron and the electron which has been removed from the neutral) [16]. These electrons do not now have enough energy to carry out another ionisation process however they still possess more energy than an electron that is combined with an atom. These free electrons are classified as 'Thermal Electrons'. The required input energy to produce a Primary Electron using ECR, when compared with producing one via a DC discharge, is significantly reduced. A comparison of the required energy can be seen in Figure 5.

For a current to be produced by the neutraliser, some of the negatively charged electrons are extracted out of the neutraliser by the positively charged exhaust plume of the Ion Thruster. The remaining ions formed by the ionisation process inside the neutraliser are then attracted to the relative negative charge of the discharge chamber walls. Upon collision with the walls, ion recombination occurs by removing an electron from the wall to revert the ion back to a neutral. This neutral propellant atom can then be ionised again, and the process continues.

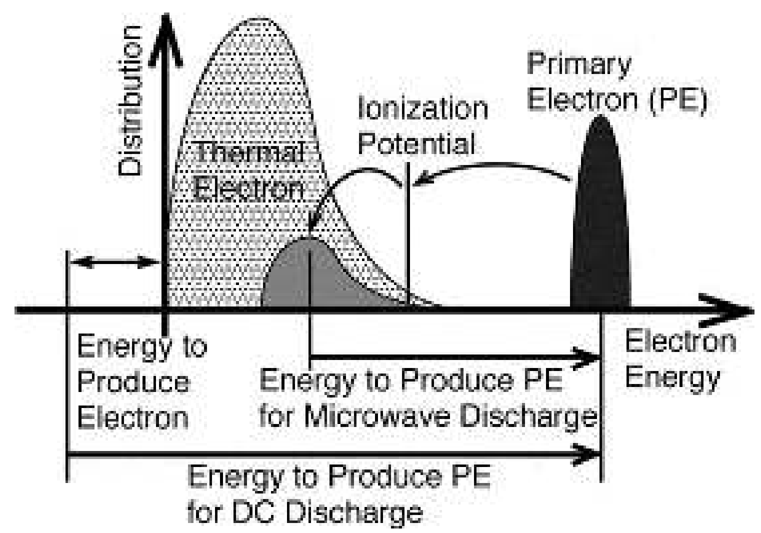

Figure 5 - Energy required for production of a primary Electron [16]

Design Brief

This project has been built upon the groundwork set out by the 2016/17 Group Design Project 'Argon Electron Cyclotron Resonance Gridded Ion Thruster' which defined the operational parameters of the complete thruster assembly and made preparations for the installation of ground support equipment.

The overarching objective of the XSEPT thruster project, being led by Dr Angelo Grubisic at the University of Southampton, is to develop a working microwave gridded ion thruster propulsion system with the aim of future use aboard geostationary satellites. To do this effectively, both the thruster and neutraliser components need to be developed in tandem, to ensure seamless integration as a complete propulsion system. This project takes on the design of a neutraliser, working to the specifications and design space determined by the original thruster design. The aims of the project are detailed in the table below.

Specifications

The design specifications of the neutraliser, defined by the project aims, are as follows:

- The Neutraliser should aim to produce a beam current of 1 Amp.
- The Neutraliser should be capable of integrating with the thruster design space.
- The Neutraliser should be designed to use argon as the propellant.
- The Neutraliser's propellant flow rate should be minimised to reduce the impact on the overall specific impulse.
- The Neutraliser should be designed to operate with a microwave power supply of 2.45GHz.

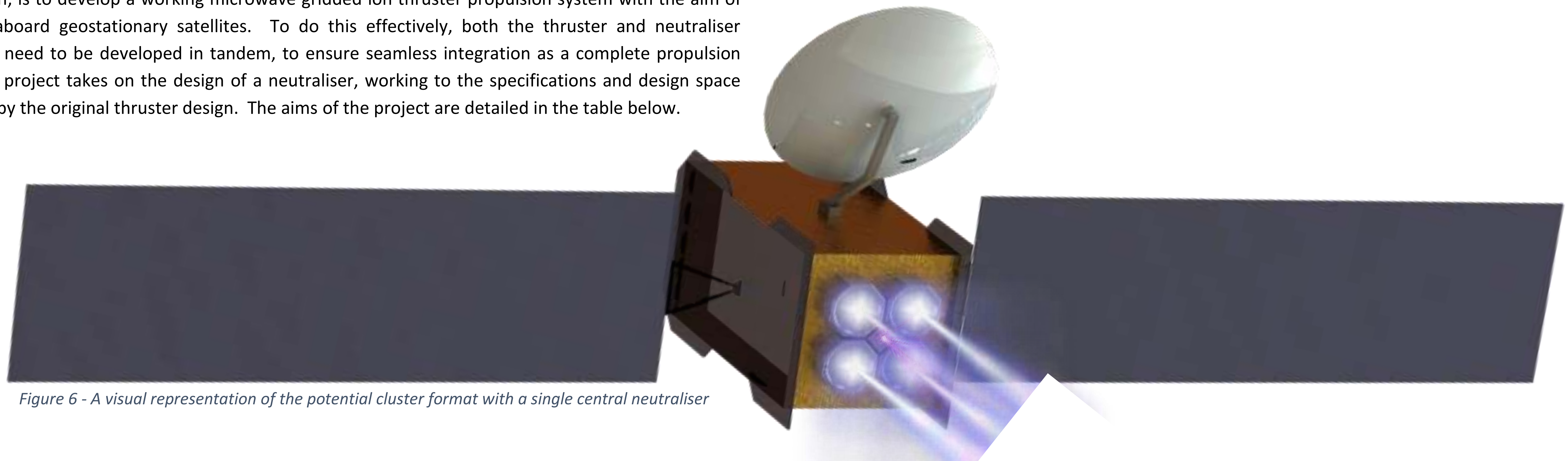

Figure 6 - A visual representation of the potential cluster format with a single central neutraliser

Design a Microwave Neutraliser using Electron Cyclotron Resonance that generates and holds a plasma capable of producing an electron current.	Test the Neutraliser in the David Fearn Electric Propulsion Laboratory under vacuum conditions.
The primary aim is to be able to ignite and sustain a plasma within the neutraliser. Because of this, the specific conditions required for achieving ECR, are the top drivers that specify the design of the discharge chamber, electric field and magnetic field. The challenge of this aim was quantifying and verifying the models in which a number of assumptions have to be made up until testing the final design, during which measurements can be taken and modelling assumptions corrected.	Because of the difficulty in modelling and predicting the behaviour of ECR generated plasma, reaching testing was identified as a must-achieve aim. To achieve this, material selection was a crucial consideration during the design phase to ensure safe operation under vacuum conditions. This related to operational problems of plasma generation in a vacuum, such as sputtering, material deposition and temperature control. Along with the microwave power supply, simplifying the connections to the electrical and propellant supplies during the design phase allowed for quick testing changes to maximise test efficiency.
Manufacture as many components as possible using additive manufacturing.	Integrate the neutraliser with the Thruster assembly for full system testing.
Additive manufacturing has progressed significantly in quality in recent years. It offers advantages over traditional manufacturing for bespoke parts with short production runs by offering reduced component cost and reduced manufacturing time. Designing the Neutraliser with consideration to the current limitations of this manufacturing type has allowed us to take advantage of the benefits by reducing material costs whilst attempting to reduce the wait time for components. An additional benefit is the complex geometry allowed by the additive manufacturing process.	The final aim of the project is to complete the integration with the thruster. This defined the performance specifications of the neutraliser and our design space, with the intention to allow the neutraliser to fit within a group of thrusters as shown in Figure 6. As the specific impulse of the assembled propulsion system depends on both the thruster and neutraliser, integration with the thruster has been a consideration from the start of the design process. This is, as of the submission of this report, the only incomplete aim, as the thruster requires additional testing for ignition point and range of operation.

Design Process

The design process was outlined in the early phases of the project, to identify the key milestones and critical points in the timeline. The objective was to reach testing of the neutraliser as this would confirm the design work undertaken throughout the project. The main concern was manufacturing lead time, which was considered and accounted for in the project planning phase (Appendix A).

1. Identify Research

The first stage was to identify previous research into the use of ECR as a form of electron generation, the application of ECR in neutralisers, and in doing so develop an understanding of the scope of the project. The Japan Aerospace Exploration Agency (JAXA) has exemplified the application of microwaves in the 'mu10' thruster, demonstrating the feasibility of pursuing the research of a larger microwave neutraliser with increased neutralisation current. Understanding the processes that were required for the successful generation of plasma and sustained operation was also key as the drivers as these processes would feed directly into the design phase.

2. Requirements

The requirements outlined the design scope. A significant consideration was the integration with the XSEPT thruster being developed in parallel with the neutraliser by David Hoffman, a PhD student. This design had been set during the GDP project run during the 2016/17 academic year [17] and therefore defined the minimum requirements for neutralisation current, as well as informing our design space. Integration with the thruster was to be a consideration from the start of the project. It was also an opportunity to investigate novel design solutions utilising selective laser melting (SLM) additive manufacturing and the complex structures achievable using this manufacturing method. Considering the limitations of SLM manufacturing throughout the design phase served to minimise unforeseen issues during manufacture and assembly.

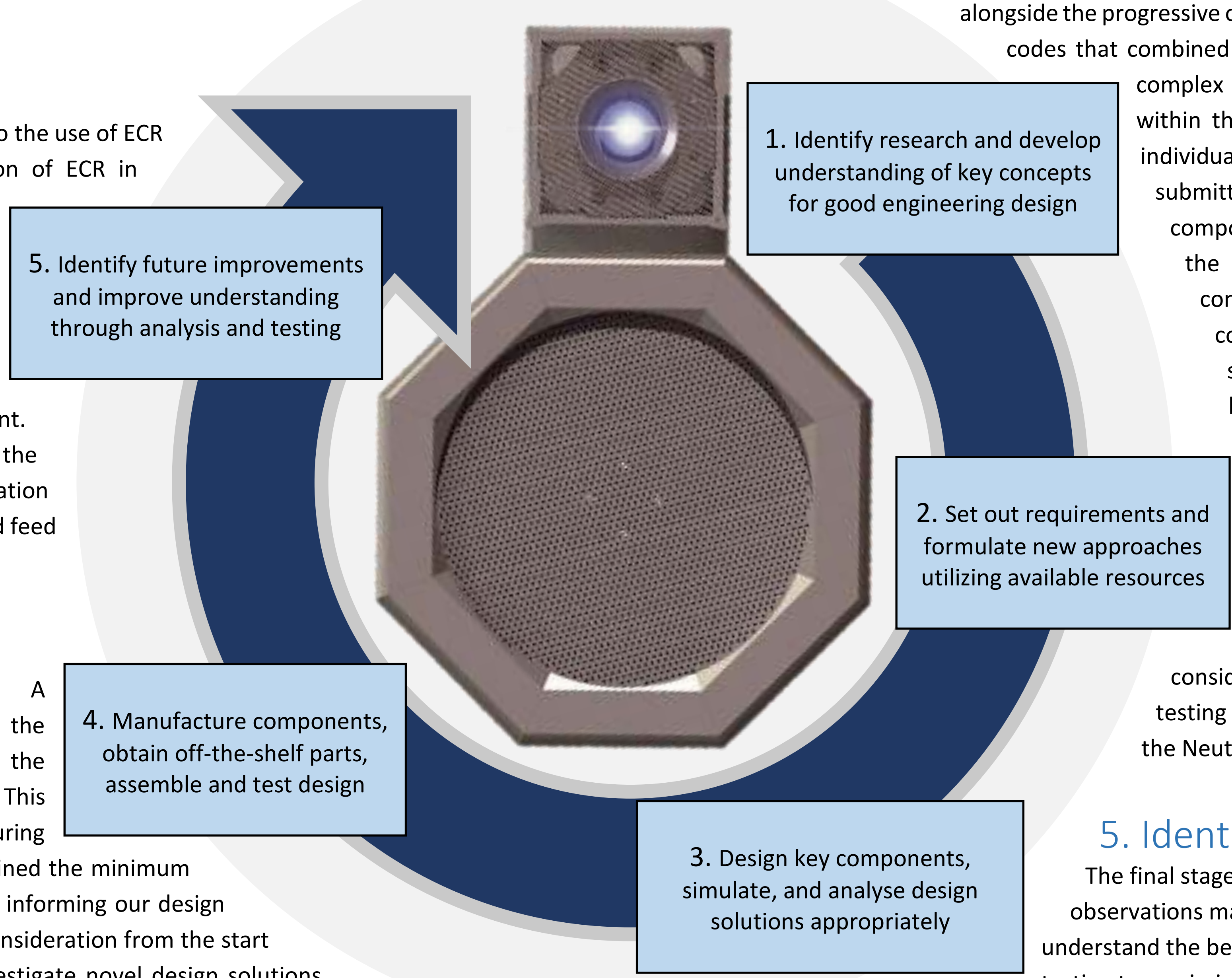

3. Design, simulation and analysis

As the design specification was prepared, a semi-analytical study was implemented to formulate a design capable of successfully performing to specification. The first phase was design, creating initial models that could then be passed on for analysis. Certain areas of importance, such as the magnetic field and electric field, could be developed separately for the initial design and verification of the simulations, before introducing shared elements to combine the studies. Because of the need to submit the designs for manufacture early in the project, simulation tools were developed alongside the progressive optimisation of the design. These included bespoke codes that combined data from several studies to better quantify the complex ECR process and plasma generation occurring within the discharge chamber. By bringing together the individual analysis for each component, the final design submitted for manufacture accounted for each component interacting with the entire system. To keep the project within budget, the assembly was considerate of the available off-the-shelf components. For components such as ceramic spacers, designing for readily available sizes brought the cost down considerably.

4. Manufacture and Test

Moving to manufacture was a critical milestone in the project. Timing this well to ensure the parts were manufactured with time to assemble and operate the neutraliser was a large consideration from the start of the project. Reaching testing was critical to assess the design and analysis of the Neutraliser.

5. Identify Improvements

The final stage has been to analyse the test data and review the observations made during testing. This has allowed us to better understand the behaviour of the Neutraliser and make changes to testing to maximise performance. By reaching testing and analysing the results appropriately, we are better able to make recommendations going forward. The long timespan of iteration allowed only one cycle, and further work should be done utilising the experimental data and the simulation and physical models purpose-built for this project.

The Discharge Chamber

The discharge chamber is the volume in which the discharge will occur and provides a surface for ions to recombine with electrons. The surface area inside the neutraliser discharge chamber needs to be maximised and was optimised by using a gridded structure, with the purpose of providing sufficient wall current to maintain the desired neutraliser current.

Requirements:

- Ability to produce 1 amp of wall current.
- Sufficient spacing between grids to prevent shielding of the grid surface by the plasma sheath.
- The grids should not interfere with other sub-components inside the chamber.

Background

By maximizing the surface area available for ion recombination, a key process to facilitate ECR, it is possible to reduce the ion density required to produce a given current. This in turn reduces the mass flow rate required. 3 different concepts were modelled: straight fins, curved fins (Figure 10) and grid fins (Figure 7). The grid design was chosen for further analysis as this was found to be the most spatially efficient.

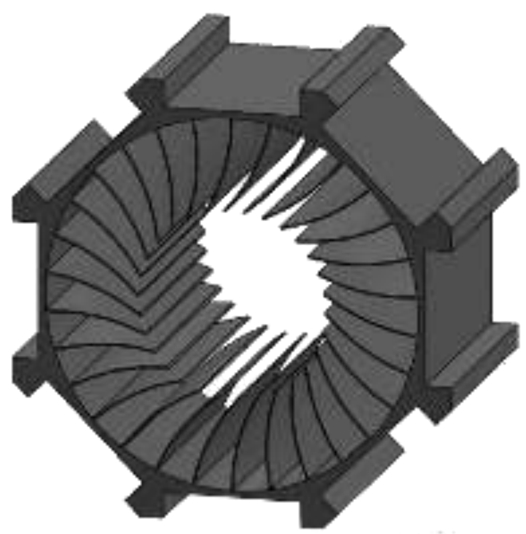

Figure 7 - Early curved fin concept design

Ions are attracted by the locally lower potential at the wall, where they will form a boundary region in which there is a higher density of ions than of electrons [18]. This boundary region is known as the plasma sheath, illustrated in Figure 8. Due to a short analysis period, time constraints did not allow full modelling of the size of the sheath, and instead, it was assumed to be no more than 20 times larger than the Debye length of the plasma. This assumption was derived from literature, and including a 4 times safety factor [19].

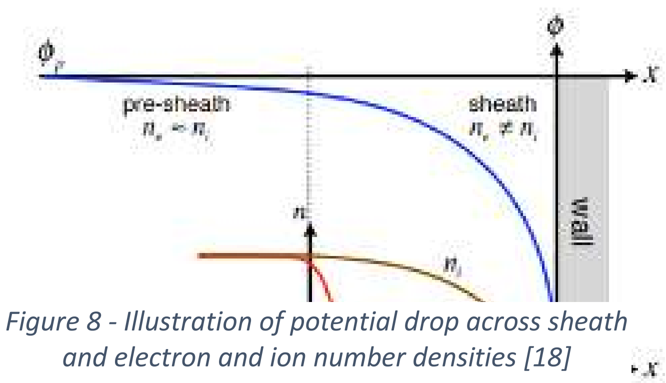

Figure 8 - Illustration of potential drop across sheath and electron and ion number densities [18]

$$\text{Debye Length, } \lambda_d = \sqrt{\frac{\varepsilon_0 k_b T_e}{q_e^2 n_e}}$$

The wall current could be estimated using the Bohm speed, i.e. the speed of ions moving through the sheath to the wall, as well as the ion density and surface area of the walls [18].

$$v_{i,sheat} = v_b = \sqrt{\frac{k_b T_e}{M_{arg}}}, \quad I_w = \frac{1}{2} A_s n_i q_e v_b$$

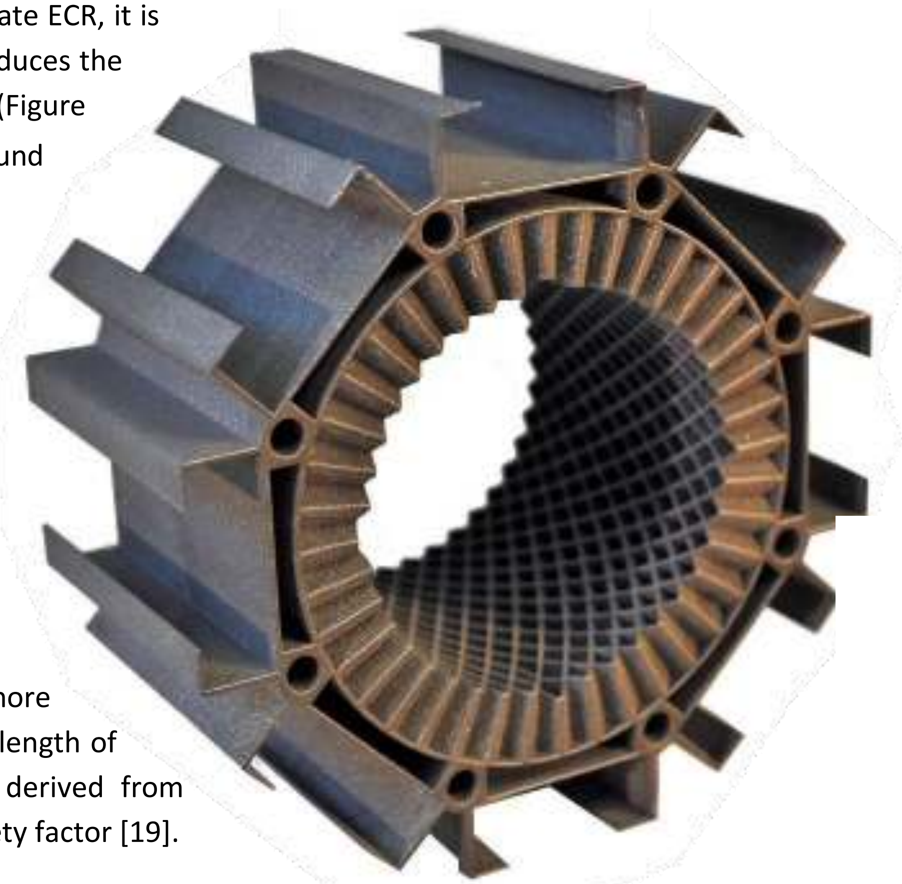

Figure 10 - The internal fin structure of the final discharge chamber

Design Process

An iterative design process was followed to maximise the surface area while ensuring the walls of the gridded structure were visible to the plasma inside the discharge chamber. The complicated geometry was very time consuming to manipulate using CAD, so to facilitate this process the surface area of the grids was modelled mathematically as a function of grid length and separation between the grids. Similar functions were set up in Python to compute grid separation as a function of surface area and grid length. The equations below show the mathematical model used to generate the structure and verified using measurements from the CAD model.

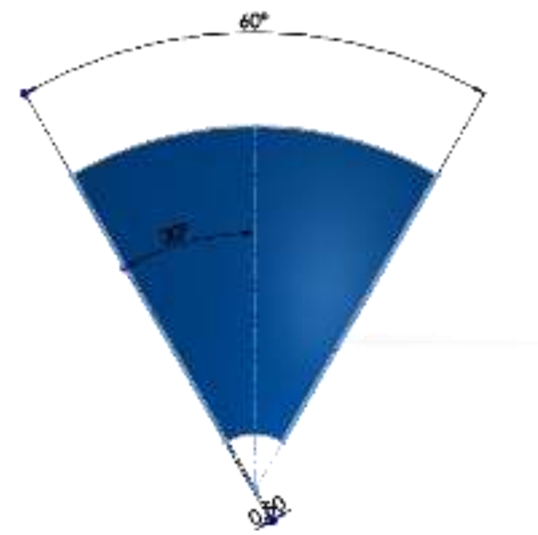

Figure 9 - A single grid seen from above the 60-degree angle represents θ_L

$$A_{s,grid} = \int_{R_{in}}^{R_{out}} \left(\frac{4X_n L_C}{\sin \phi_f} - \frac{2nT_L}{\cos \phi_f} \right) dR$$

$$\phi_f = \tan^{-1}\left(\frac{L_c}{\theta_L R}\right)$$

$$X_n = \frac{2\pi R_{in}}{T_L s_{min} \cos \phi_f}$$

- n: number of intersections between all single fins, this is used to estimate the area lost by fins overlapping
- L_c: Length of Chamber in meters
- ϕ_f: angle of the fin from the bottom plane, this varies radially along the fins, assumed to be constant along length of chamber for the sake of this estimation, shown in Figure 11
- X_n: Number of iterations of the X shaped pattern used to create the gridded structure, this is a function of the minimum fin separation
- T_L: thickness of the fins, in this case 0.3mm as it was the minimum thickness that we could safely manufacture using the printer
- s_{min}: minimum separation between the horizontal corners of each grid, as this as the smallest distance.
- θ_L : the angle used to create the geometry, shown in

UNIVERSITY OF Southampton

Script Process

Due to constraints with other components inside the chamber, the inner radius (radius of the grid tips from the centre of the chamber) was set at 50mm which simplified the optimisation to a single variable.

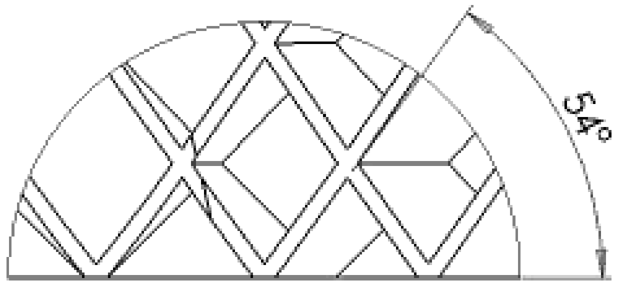

Figure 11 - close-up of fin geometry, angle between floor and fin is ϕ_f, can observe the radial variation of this angle

The process followed is illustrated below, and was carried out in an iterative manner:

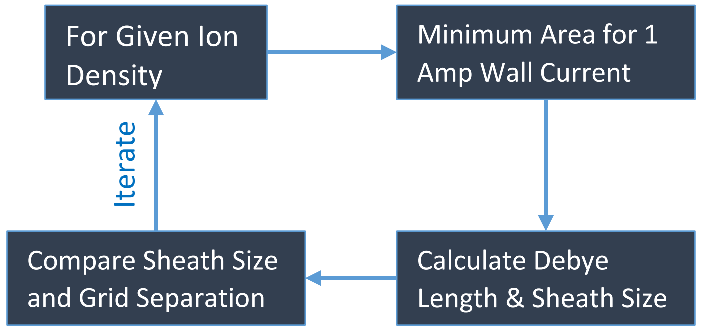

1. Starting at critical density (i.e. max possible number density) the Debye length and Sheath size were calculated
2. At this same density, the surface area to obtain 1 Amp of wall current and the corresponding grid separation were calculated.
3. The sheath size and grid separation were compared. If the former was smaller than the latter then the ion density was reduced by a small interval, and steps 1 to 3 were repeated.
4. The script would stop iterating once the sheath size was greater than the grid separation.

Figure 12 shows surface area variation against ion density, as well as corresponding sheath sizes and grid separations in the same ion density range.

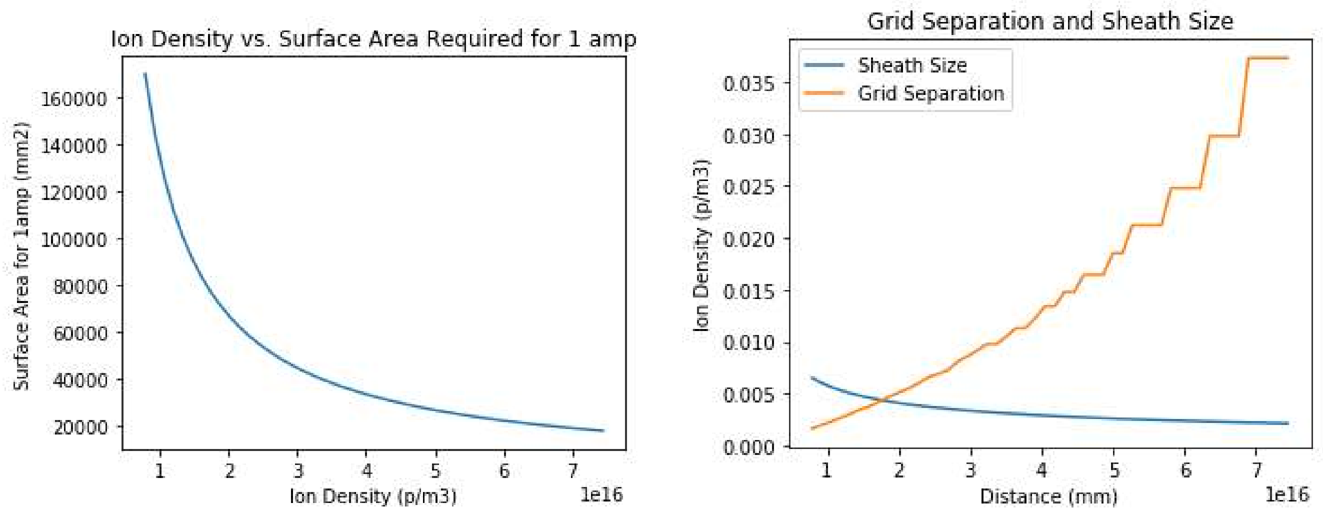

Figure 12 - Plots showing variation of required surface area, grid separation and sheath size against ion density

Final Design

This process gave a range of functional designs. The design simulating the minimum ion density is the optimal choice as this corresponds to the lowest required flow rate through the neutraliser. Once the rough operating range was calculated, the lower values were investigated in more depth and verified using CAD models before settling on the final design described below:

- Total Surface Area (including Orifice Plate and Yoke): 93308 mm^2
- Grid Separation: 3.5mm
- Minimum Ion Density: 2.71E16 n.m^{-3}

Using this design, the mass flow calculations could be completed for a range of orifice sizes, which would be compared against the electric potential encroachment into the neutraliser for those same orifice sizes. This process is described in the Orifice Plate design section.

The main issue with this process is it assumes the neutraliser ECR regions will be capable of maintaining the ion density required to make the grids functional, something which is extremely difficult to ascertain with any confidence before the part is tested.

Additional Considerations

The outside of the chamber had to be designed to accommodate the correct number of magnets, the magnet insulation and PTFE sleeves that would sit around the magnets to prevent metal on metal contact with the chamber walls, as well as interfacing with other components. This slot is shown in Figure 13.

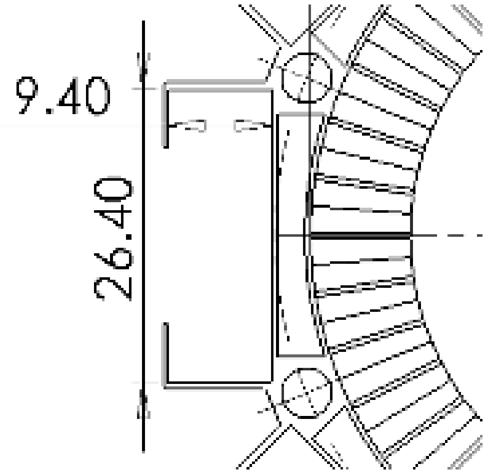

Figure 13 - Close up of magnet mounting slots

Because the structure would be held together with bolts running through the entire length of the chamber a small gap was left between the inner chamber and the magnet racks.

This had the combined benefit of providing a thermal stand-off between the plasma in the chamber and the magnets, as well as providing a significant mass saving. The walls were kept as thin as possible to reduce material cost so, like the grids, were kept at a 0.3mm thickness to ensure their manufacturability. Additionally, the angle of the grids from the bottom plane had to be larger than 45 degrees at any position.

Small cut-outs had to be made at the base of the grids, shown in Figure 14, where they would interface with the iron yoke. This prevents interference between the innermost ends of the grids and the inlet nozzles, allowing for manufacturing tolerances.

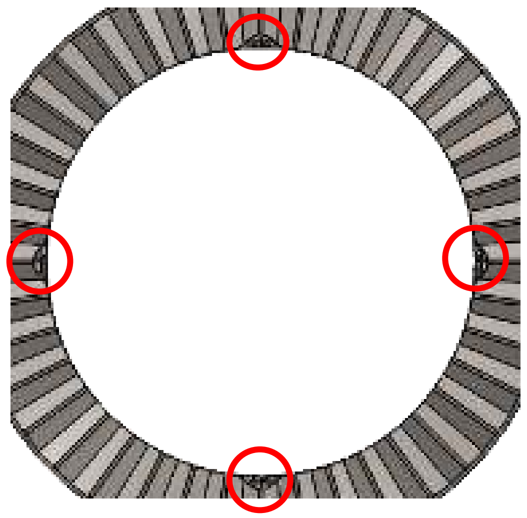

Figure 14 - bottom view of neutraliser grids with nozzle cutouts circled in red

UNIVERSITY OF Southampton

Orifice Plates

The neutraliser orifice accommodates the required release of electrons in order to sufficiently neutralise the main thruster ion beam. Figure 15 shows the Project NITRO orifice plate during assembly.

Requirements

There are several important considerations associated with the main trade-off of orifice design. The dimensions must be large enough to allow sufficient electric field potential visibility (ie. to allow an adequate release of electrons to be drawn towards the positive electric field of the thruster ion beam) and the orifice dimensions must also accommodate a sufficient back pressure within the neutraliser to ensure the appropriate plasma density is maintained during operation.

Figure 15 - Assembly of the orifice plate attached to chamber

The primary main assumptions were implemented within a series of python scripts, generated as a simplified method of identifying a number of unknown quantities within the neutraliser. The variations in specific impulse were calculated for all various orifice sizes and ion number densities, to determine the incremental drop in performance of the system provided by the neutraliser, as well as the associated mass flow within the system. The values suggested by the various Python scripts were combined with the preliminary results obtained from COMSOL to identify a range of appropriate orifice dimensions.

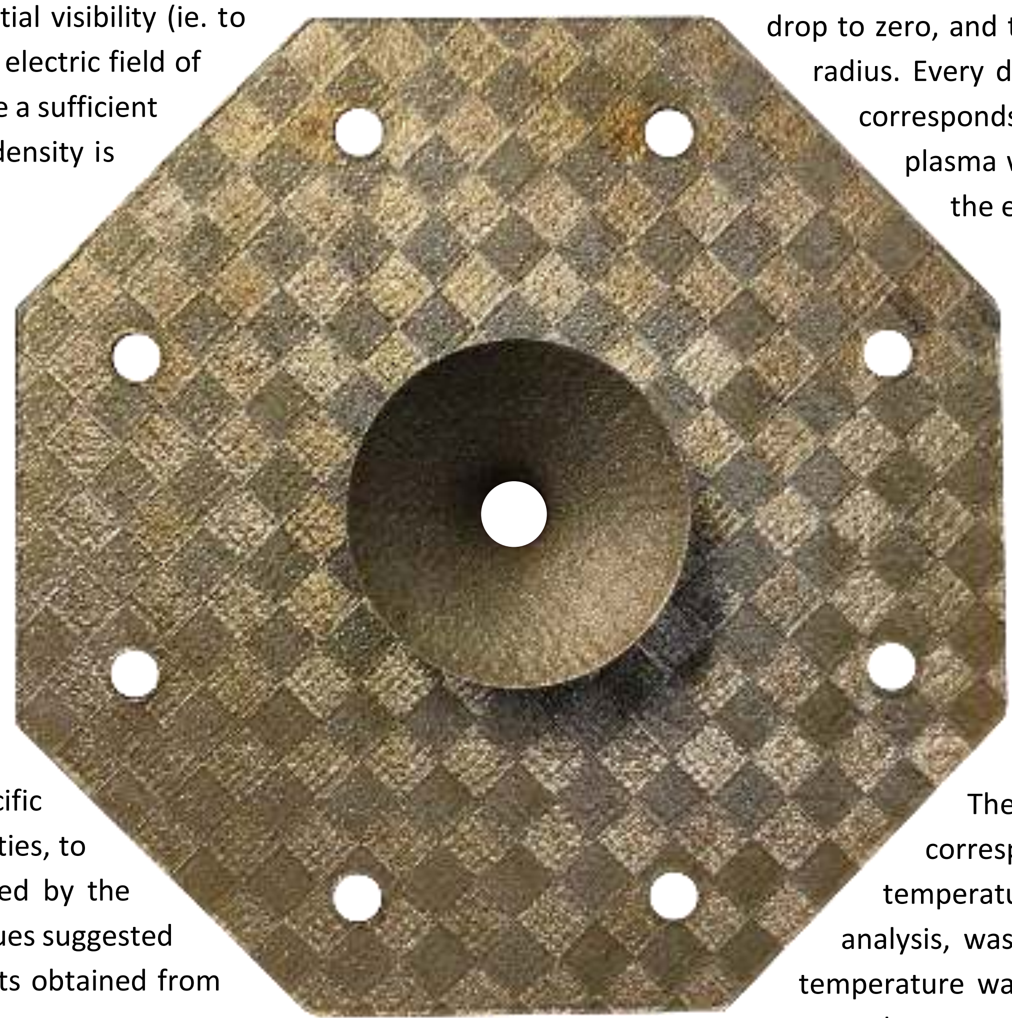

Figure 16 - One of three printed orifice plates

Python scripts

The first steps taken in constructing the chamber flow python script were primarily determining the maximum possible ion number densities within the discharge chamber, for both comparison of the discharge characteristics and analysis of the requirements needed in achieving a sufficient plasma density.

Key Assumptions

The main assumptions taken into consideration throughout the course of the neutraliser orifice design were as follows:

1. The maximum possible achievable plasma density within the neutraliser is referred to as the 'critical density'.
2. Upon ignition of the neutraliser, it is assumed that the plasma will only see around two-thirds of the entire discharge chamber fin surface area.
3. The Debye radius of the electrons within the neutraliser can be described as the length over which the electric potential recognised by the particles within the plasma will subsequently drop to zero, and the Debye sheath is the resultant sphere of this associated with this radius. Every distance of 1 Debye radius further from the source of the potential corresponds to a drop in 1/e of the associated electric potential. The sheath of the plasma within the neutraliser is assumed to be around 20 times the value of the estimated Debye radius.

As the chamber pressure would be easily fulfilled due to the low flow rate requirement, it was decided that multiple orifice sizes would be tested to maximise data collection, as well as ensure adequate 'field visibility' between the neutraliser and thruster beams. The preliminary Excel grid data geometry was combined with the local number densities and associated ionization fraction assumed within the discharge chamber, giving a much clearer idea on the appropriate chamber pressure to maintain the critically dense plasma required within the neutraliser during operation.

Chamber pressure

The chamber pressure was determined using a sum of ideal gas laws corresponding to the ion, electron and neutral number densities and temperatures. The ion temperature, similarly with other cases of ion thruster analysis, was assumed to be around 0.1eV (around 1160.5K), and the electron temperature was set at around 5eV [20]. It was agreed with Dr. Grubišić that the neutral temperature of the plasma was to be assumed as roughly 500K. The maximum ion number density within the plasma was also determined as a function of the input frequency provided by the microwave power supply at 2.45GHz, giving a number density of around 7.45×10^{16}.

Specific impulse

The gridded ion thruster specific impulse was set as 5500s to determine the change in the overall system specific impulse caused by the neutraliser. These trends were plotted to subsequently determine this associated I_{SP} drop over a range of orifice sizes. This was then iterated through the estimated number densities to yield the minimum surface area to accommodate both the Debye radius and the required fin separation. Figure 17 represents the overall specific impulse of each system for varying orifice plate radii, where it can be seen that the most significant drop in I_{SP} is brought about between the 2mm and 3mm radius configurations. This intrinsically set a limitation on how large the orifice was to be made in terms of loss of overall system specific impulse when considering both the thruster and neutraliser

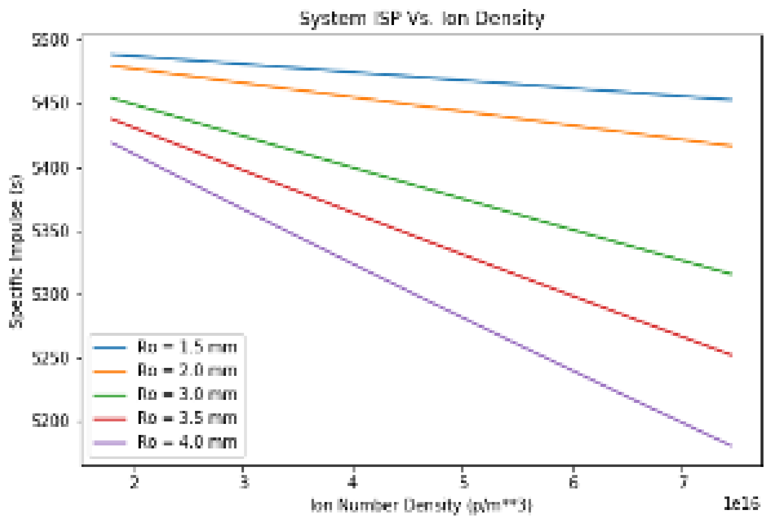

Figure 17 – The change in system specific impulse at different ion densities

COMSOL Simulations

COMSOL, a Multiphysics software, was used as the first method of replicating the electric field potential between the orifice and the thruster ion beam. The first simulations undertaken continued the work carried out by the GDP group who initiated the project [17]. A 2D plot version of the neutraliser outline was made based on our preliminary designs, and an electrostatics simulation was carried out along a constant y-value running from the start of the chamber to the location of the orifice. A charged plate was then placed at 10cm from the orifice location, in order to simulate the positive electric potential of the thruster beam. The preliminary results were used to visually determine the penetration of the beam potential into the discharge chamber. Further analysis was then carried out on the electrostatic potential behind the orifice (within the chamber) to determine the 'cut-off' point at which the potential field visibility is inadequate. The simulation was run for 9 different orifice diameters, ranging from 2mm to 10mm in 0.5mm increments, for a visual analysis of the electric field penetration into the orifice. The results suggested that a minimum orifice diameter of 6mm would allow adequate field recognition. The design process then continued with the idea of manufacturing 3 separate orifice plates for testing, each with a different orifice size. Shown in Figure 18 are 2D representations of both the electric potential distribution and the electric field around a 6mm orifice during operation of the neutraliser, essentially providing a more accurate visual representation of the penetration of the thruster beam potential past the orifice and into the discharge chamber. The beam voltage was then increased to 100V for further analysis, as well as to simulate the effect of the neutraliser's operation around multiple thrusters. It can be observed from the zoomed field strength plot that the 6mm orifice offers a significant amount of field visibility, as a positive electric potential can be seen both at and around the orifice.

6mm orifice 7mm orifice 8mm orifice

Figure 18 - 2D simulations of electric field through the orifice

The values of the potential recognised within the chamber were then extracted from COMSOL as a series of CSV files, and a simple Python script was written to process the data and plot the necessary correlations.

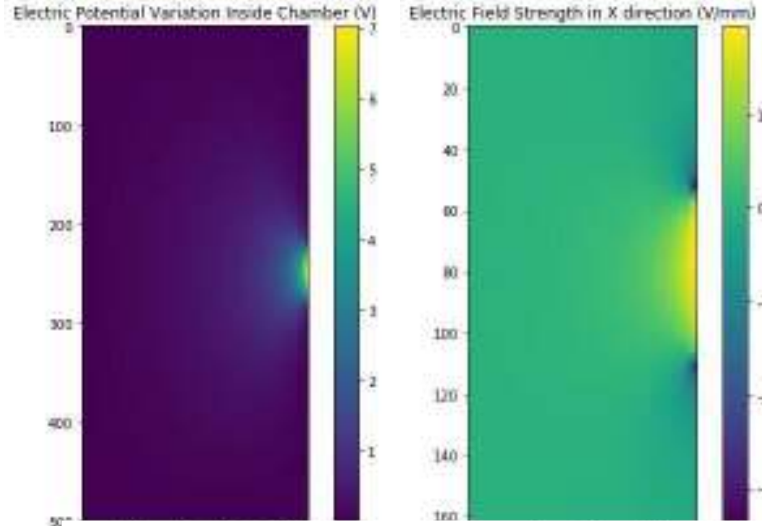

Figure 19 - Electric Potential Variation (left) and Electric Field Strength (right)

The electric potential was then plotted against chamber position, shown above in Figure 19, to determine the range of electric potentials recognised within the neutraliser for varying orifice sizes. The correlation seen within the electric field strength plot shown in Figure 20 gives a more accurate representation of the acceleration force experienced by electrons as they are attracted from the orifice. The influence of the beam voltage, represented by the intersection of the various field strength trends, suggests that minimising the orifice size lower than 4mm does not significantly impact the field strength recognised around the orifice plate. Despite these models suggesting that the electric field did not significantly vary between orifice sizes, there was still a concern that using too small an orifice would limit the maximum extractable current from the neutraliser.

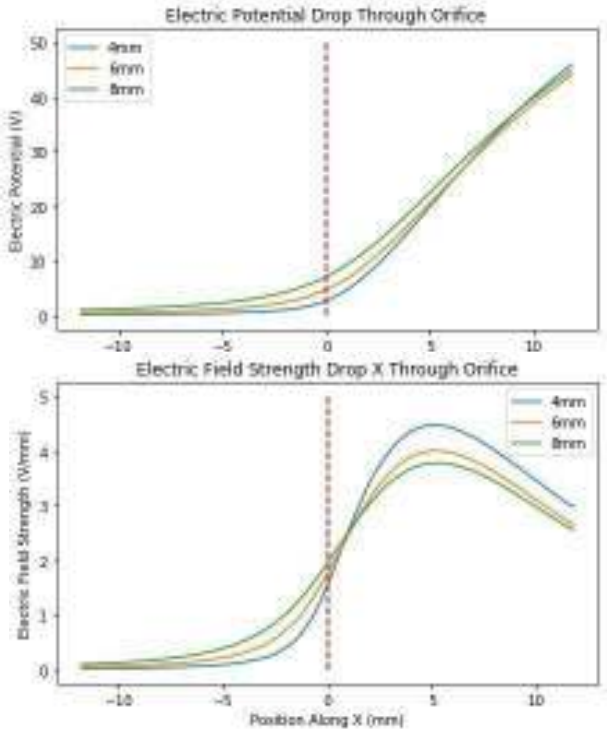

Figure 20 - Electric Potential Variation (top) and Electric Field Strength (bottom) through orifice

Debye Sheath

The plot shown in Figure 21 represents the variation in Debye sheath size with respect to the associated drop in electric potential. The sheath size was initially assumed as at least 20 times the value of the Debye radius, however, the appropriate sheath size was estimated with greater accuracy once a 'safety' range of flow rates had been established using our scripts. The correlation from the Debye sheath plot and the results from the COMSOL electric potential simulations confirmed that the orifice size should not fall below 4mm. Anything below this would potentially allow a sheath to form across the orifice, restricting the penetration of the beam voltage potential into the neutraliser.

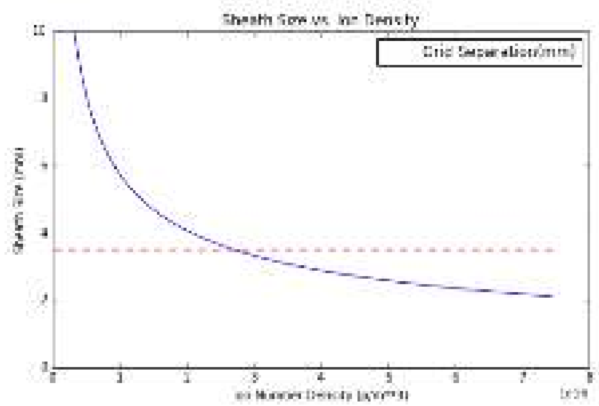

Figure 21 - Sheath Size vs Ion Density

Propellant Reservoir and Nozzles

With the electrostatic field gradient determined, the next step was achieving the chamber pressure needed to maintain an appropriate plasma density. This meant providing the neutraliser with extremely low flow rates, requiring a specific manner of propellant distribution. An inlet reservoir was fashioned with 4 individual propellant inlet nozzles, to be connected to the Argon propellant supply with a Swagelok fitting.

The inlet nozzles were designed around a required mass flow of around 0.07 mg/s throughout the discharge chamber, corresponding to a chamber pressure requirement of 1 Pa. The idea of including multiple nozzles, originally introduced by David Hoffman (a PhD student working with the XSEPT thruster), was included specifically for ease of both propellant expansion and distribution.

The main assumptions taken into consideration throughout the course of the neutraliser propellant inlet reservoir and inlet nozzles were as follows:

- The flow of the propellant at the outlet tip of the nozzle was assumed as choked (ie. M=1)
- For consistent results in estimating the associated flow rates, the neutral gas temperature was assumed as 500K and the chamber pressure around 1 Pa, matching the values used in orifice design.

The mass flow correlations determined during the orifice plate design process, such as Figure 23, showed that the propellant reservoir should act to provide between 0.7 and 4 SCCM. The deductions made from the orifice plate research drove the requirements of the propellant supply system. The nozzle outlet velocity was initially found using the electron temperature within the choked flow assumption, corresponding to a velocity requirement of 322.5m.s[1]. From this, the outlet mass flow was estimated to be around 1.25×10^{-8} kg.s^{-1}, corresponding to an outlet density requirement of 0.197×10^{-3} kg.m^{-3}.

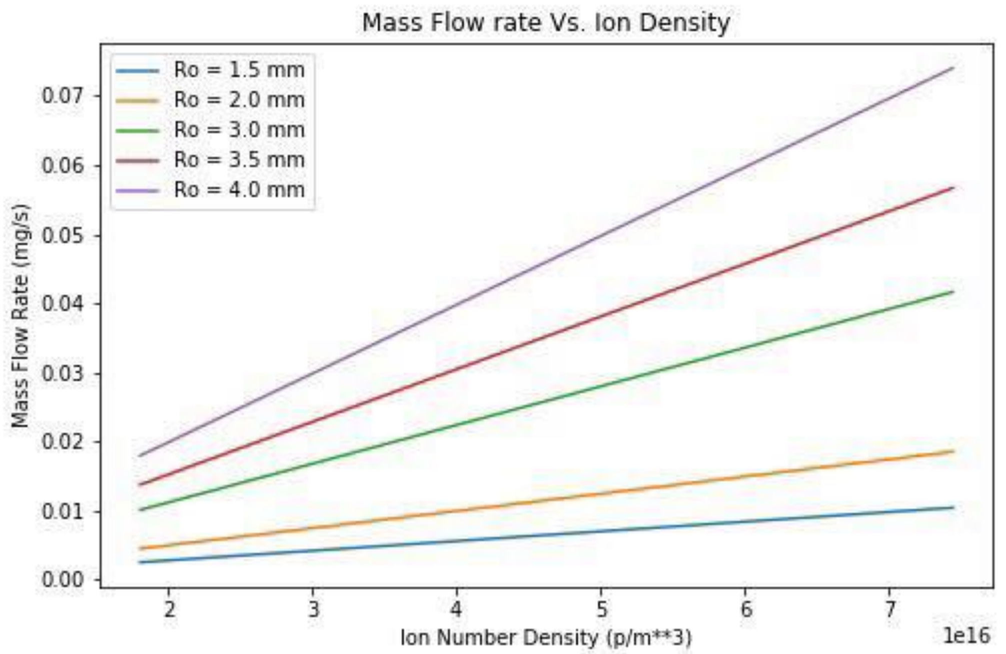

Figure 23 - A plot of mass flow versus ion density for a range of orifice sizes

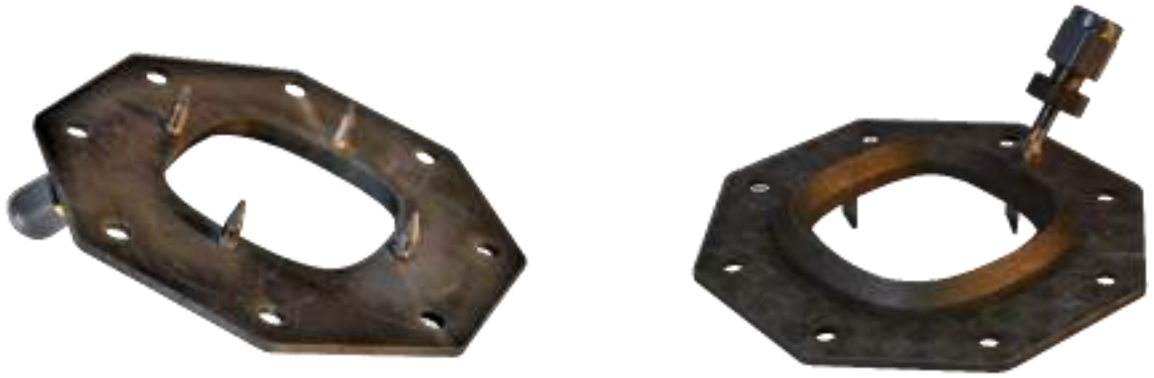

Figure 22 - The 4 propellant nozzles fixed to the reservoir plate.

The temperature ratio output of the correlated Mach number relations was also determined in order to calculate the static temperature and hence pressure at the nozzle inlet (p = ρRT at the nozzle inlet), and therefore the stagnation pressure at the propellant reservoir ($p_0 = p + 0.5\rho V^2$ between reservoir and nozzle). The neutraliser chamber pressure requirement corresponded to a propellant reservoir pressure requirement of around 6.42mbar. Achieving this allows the flow at the tip of each nozzle to become choked, and adequately expand into the neutraliser discharge chamber to achieve the pressure requirement of 1 Pa. The inlet flow analysis python scripts were then developed to iterate over specific input conditions. This determined the optimal propellant inlet nozzle dimensions to achieve a discharge chamber pressure of 1 Pa. Figure 22 shows the neutraliser fuel distribution unit after integration of the four nozzles. Figure 24 shows two propellant inlet nozzles following their manufacturing and tapping

Figure 24 - The inlet nozzles

A friction factor was also taken into consideration in order to determine any associated losses throughout the pipe, based on the velocity of the propellant and any resistance due to friction or surface roughness. The effects are considered minimalistic for this particular case as the neutraliser propellant inlet nozzles are extremely short and experience extremely low flow rates for optimal propellant expansion. These induced losses were then considered in terms of Mach number throughout the pipe, ultimately to both model such losses for a given inlet Mach number, as well as specifying whether the flow within the pipe is laminar or turbulent. However, as the flow rate is in the order of milligrams per second, the flow is assumed to be generally laminar.

Magnetic Field Design and Topology

Design Requirements

In order to generate ECR, a magnetic field must be generated with a strength corresponding to the frequency of microwave discharge used. The main requirement for the neutraliser's Magnetic Field Topology (MFT) was to achieve a field strength of 0.0875 Tesla (T) in regions where ionisation is required, as this was dictated by the 2.45GHz Microwave generator.

Generating a field of 0.0875 T was the main driver for the design of the MFT, however, an additional requirement was to maximise the ECR surface's area whilst preventing holes or gaps. The ECR surface is the surface where the magnetic field strength is equal to 0.0875 T. Increasing the surface area serves to maximise the ionisation rate and therefore increases the current which can be produced. The limitation of this is that the surface must not contain any holes, as these are regions in the ECR surface where the neutral propellant atoms can pass through freely, avoiding interaction with the regions where the Primary Electrons are located. If this were to occur, there would be a significant mass flow of un-ionised propellant flowing out of the neutraliser without passing through an ECR region and being ionised, thus reducing system I_{SP}.

A key concept justifying the efficiency of an ECR neutraliser is the use of magnetic mirroring in the design of the MFT, as used in the neutraliser of the mu10 thruster [16]. By using magnetic mirroring, the free electrons inside the neutraliser can be confined and carry out numerous ionisation processes, as illustrated in Figure 25. This electron confinement can direct the Thermal Electrons through the ECR regions, thereby turning them into Primary Electrons due to the resonant effects at this magnetic field strength. Achieving this requires a free volume for the electrons to travel through (along the magnetic field lines), with a higher magnetic flux density at each end of the confinement region. This imparts a significant force on the electrons causing them to change direction and travel back along the same path, confining them within the field [21].

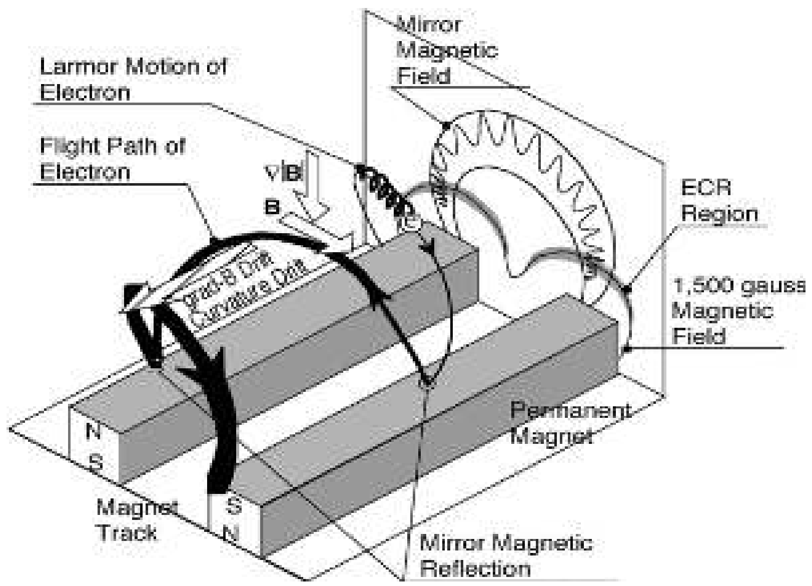

Figure 25 - Illustration of Electron Confinement by Magnetic Mirroring [16]

A final requirement for the MFT is to minimise the mass of the components used to produce the required ECR surface.

Material Selection

The two key components required to produce an optimised ECR surface are magnets, and a material with a high magnetic permeability for shaping the field as required.

Permanent magnets were selected over electromagnets, subject to an initial feasibility study, as this lowers the power requirement of the neutraliser, as well as the design complexity. Simulations were carried out on two magnetic materials - Neodymium and Samarium Cobalt magnets. The technical details of both are detailed in Table 1. Both magnet types were assessed for this application using COMSOL simulations.

Type of Magnet	**Remnant Flux Density (RFD)**	**Coercivity**	**Density**	**Maximum Operating Temperature**
Neodymium	1.3 T	11,500 Oe	7.4 gcm^{-3}	80 °c To 120 °c
Samarium Cobalt	1.1 T	9,700 Oe	8.4 gcm^{-3}	350 °c

Table 1 - Physical properties of various candidate magnet materials

To effectively shape the ECR surface, a material with high magnetic permeability is required. For this project, 99.8% pure iron was selected due to its high magnetic permeability, low material cost, as well as the ease of machinability and handling. To obtain the required relative magnetic permeability of around 5000, the 99.8% pure iron was required to undergo a magnetic annealing heat treatment process in a pure Hydrogen atmosphere.

3D Magnetic Field Simulation

COMSOL was set up to evaluate the magnetic field using an early design of the discharge chamber, and a simplified cylindrical iron yoke with a relative magnetic permeability of 5000. Optimally, annular ring magnets would be used, however, budget constraints did not allow for this option. Instead, small individual stackable magnets were optioned that could be assembled to the optimal arrangement. The simulations, an example of which is shown in Figure 26, found that:

- Higher RFD reduces the yoke mass and increases the ECR surface area.
- A 12-sided chamber required deeper magnet layers.

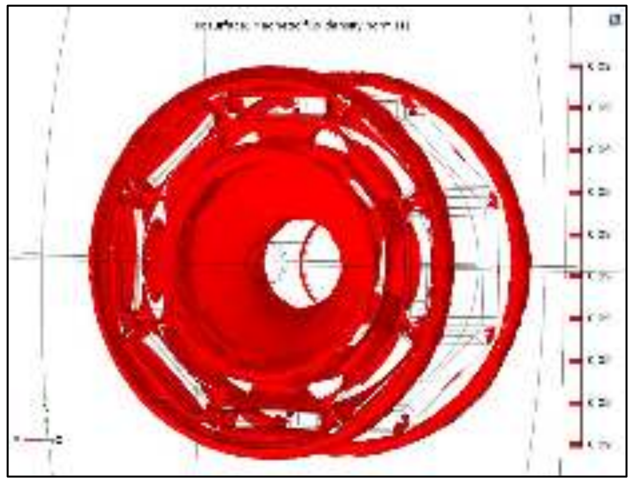

Figure 26 - The ECR surface for 4mm deep Neodymium magnets

This fed into the chamber design for magnet arrangement, with the chamber being modelled with 8 magnet rack slots. It also determined the use of neodymium, due to the improved RFD. This introduced thermal concerns which required consideration due to the lower operating temperatures of neodymium.

Magnetic Yoke Design

The iron yoke design is crucial for maximising the ECR surface area whilst minimising the mass of the neutraliser. A parametric relationship study for the various parameters which defined the shape of the central yoke was carried out to aid in design optimisation. This allowed for significant mass reduction whilst maximising the ECR surface area.

Main Yoke

Figure 27 shows a cutaway of the cylindrical yoke designed for the 'MUSES-C' mission [22]. Because of this, cylindrical yoke geometries were initially investigated with parametric relations used to optimise the design. To further improve on this conventional yoke, a new 'mushroom' yoke was designed, shown in Figure 28. The benefits of this design are:

- The antenna hole can be the perfect size for the selected antenna. With a cylindrical yoke, this would dramatically increase the wall thickness and therefore the mass of the design.
- The ECR surface area is larger than the cylindrical yokes due to the smaller antenna hole.
- It does not occupy as much space inside the discharge chamber due to the narrow stem.
- No increase in mass over the cylindrical yoke design despite the numerous advantages.

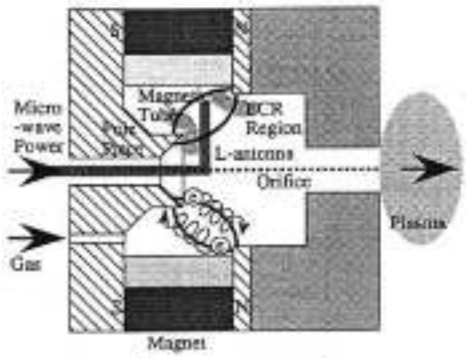

Figure 27 - ECR Neutraliser as designed for 'MUSES-C' [22]

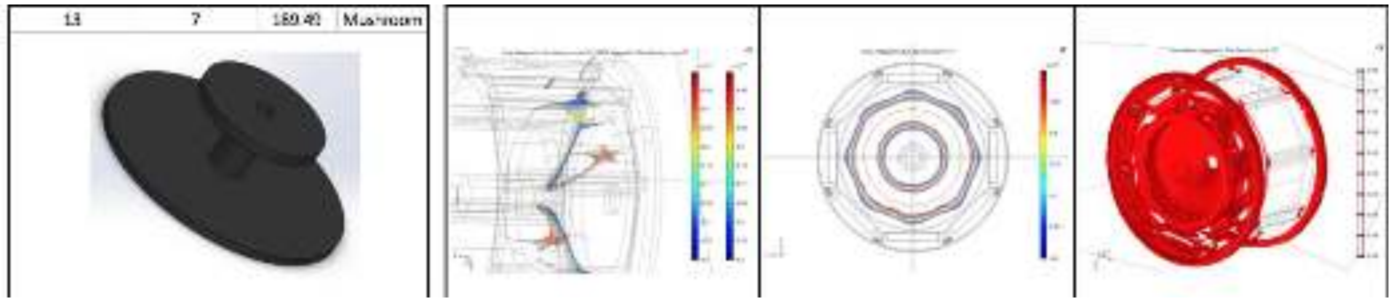

Figure 28 - Mushroom yoke field simulation (no ring yoke)

Ring Yoke

In addition to the main iron yoke, a secondary 'Ring Yoke' was designed. A Ring Yoke shapes the ECR region so that it is circular, unlike that shown in Figure 28. A circular ECR surface using a ring yoke causes ionisation to take place at a uniform distance from the fins, shown in Figure 29. It also pulls the ECR surface away from contacting the fins of the discharge chamber, allowing for uninterrupted electron confinement regions. The ring yoke is positioned at the opposite end of the discharge chamber to the main yoke, effectively making them opposite magnetic poles. This allows for the field lines to be positioned between the yokes as required.

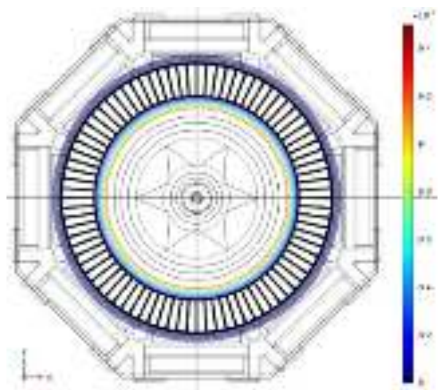

Figure 29 - Circular ECR region with Ring Yoke

Final Design

Figure 31 shows the assembly of the yokes at either end of the N45H magnet arrays. The main yoke supports the antenna, antenna insulation and antenna top shield through its core whilst still achieving the desired field strength and shape outside of the fin structure.

When simulated, the final yokes produced an ECR surface that had the maximum possible area without holes, as restricted by the strength of the selected neodymium magnets. The surface also does not meet the fins of the discharge chamber, therefore allowing the magnetic mirroring of electrons in the discharge chamber. The designed region is located between the main yoke and the ring yoke, where the antenna radiating element is situated. Having the antenna located in the ECR region leads to more efficient ECR performance due to higher electric field strengths and therefore, increases plasma generation.

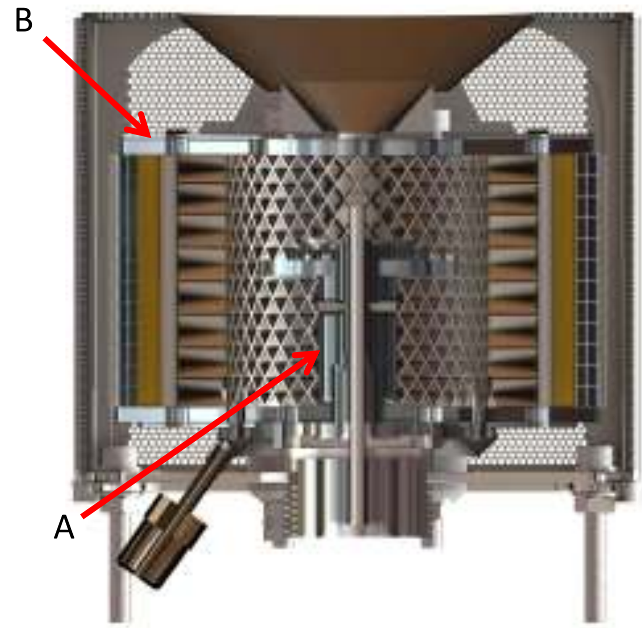

Figure 31 - Cutaway view showing the main yoke (A) and the ring yoke (B)

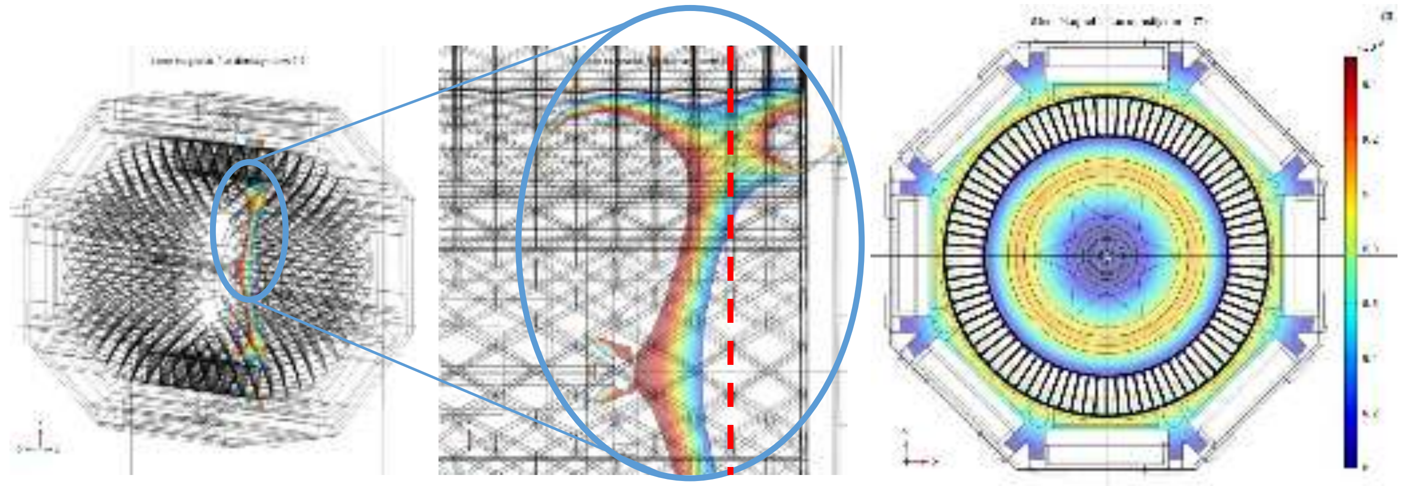

Figure 30 - Thermal slices of the ECR region. Left and centre are side slices. Right is a top slice at the dotted line.

The ECR region can be visualised as a thermal slice showing locations with a magnetic field strength of 0.0875 T, illustrated in Figure 30 by the green region. The MFT was made slightly stronger than required to account for performance loss of the magnets and the heat treatment process of the iron not producing the exact relative permeability specified.

Antenna Design

Overview

The microwave antenna is second of two components necessary for the ECR phenomenon to occur inside the neutraliser chamber, the other being the magnetic field detailed above. It provides an electric field, which is confined by the chamber walls. The neutraliser was designed to utilise a 2.45 GHz microwave generator, which was ordered prior to the project and installed shortly before testing began.

The primary driver of antenna design is to maximise the electric field strength in the ECR regions, maximising the energy available for absorption by the free electrons trapped in the magnetic mirror. The stronger this electric field, the greater the energy gain by a free electron and the greater the chance of an ionising collision occurring. This increases the total ionisation rate and plasma density which define the maximum available current that can be drawn by the Ion Beam.

The second driver of design is the radiation patterns of each antenna. The ECR region is axis-symmetrical throughout the chamber and ideally, the radiation pattern will also be axis-symmetrical to maximise the overall surface where ionisation can occur.

Figure 32 shows the relationship between the electric field strength and ionisation rate, demonstrating that the electric field has a big impact on ionisation performance such that antenna design is critical to the overall neutraliser performance.

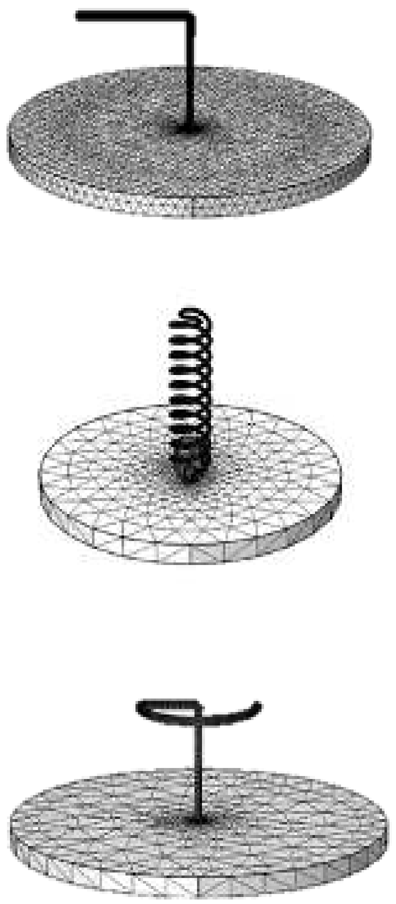

Figure 33 - Antenna Designs from previous work

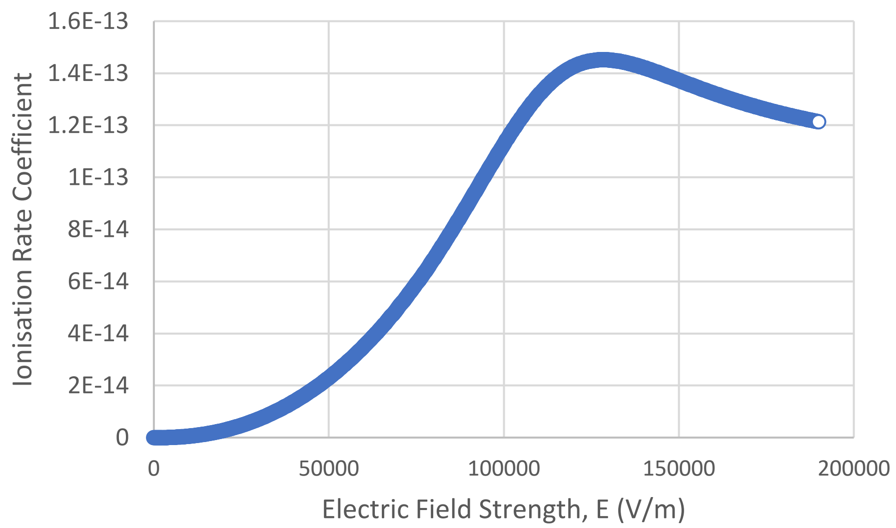

Figure 32 - Impact of the Electric field on Ionisation Performance

Design Process

The design process began by simulating and comparing the three antenna designs, shown in Figure 33, that had been put forward by the team working on the project previously [17]. Of the three designs, only the L-Shape provided a field of reasonable strength and this was carried through a design concept for our own studies.

A Parametric Design Study was carried out investigating the influence of various parameters including cross-sectional area and cross-sectional shape. These were carried out by simulating a simple 12.2 cm (Full wavelength) monopole antenna sticking upright out of a flat plate, the results were as follows:

- A greater cross-sectional area improved the electric field strength with diminishing returns seen above a 4mm diameter.
- Various cross sections were investigated for the monopole antenna including star and square shapes, however, it was found that the commonly used circular cross-section was optimal.

A second study was carried out using the L-Shape design to see the effect of stem length on overall performance. The study found that the length of the stem has minimal impact on performance and therefore the antenna radiating element could be positioned to best radiate within the ECR regions. This differs from the monopole antenna, which radiates from the stem and as such the length must be related to the wavelength.

The monopole antenna was briefly investigated with quarter wavelength (3.05cm) and half wavelength (6.1cm) options. Limitations on discharge chamber height ruled out the half wavelength antenna, whilst the quarter wavelength would radiate mostly within the central yoke. As a result, the antenna and magnetic field teams were brought together to pursue a design that would benefit both yoke and antenna designs. The difference in Electric field strengths of the monopole with and without the surrounding yoke can be seen in Figure 34.

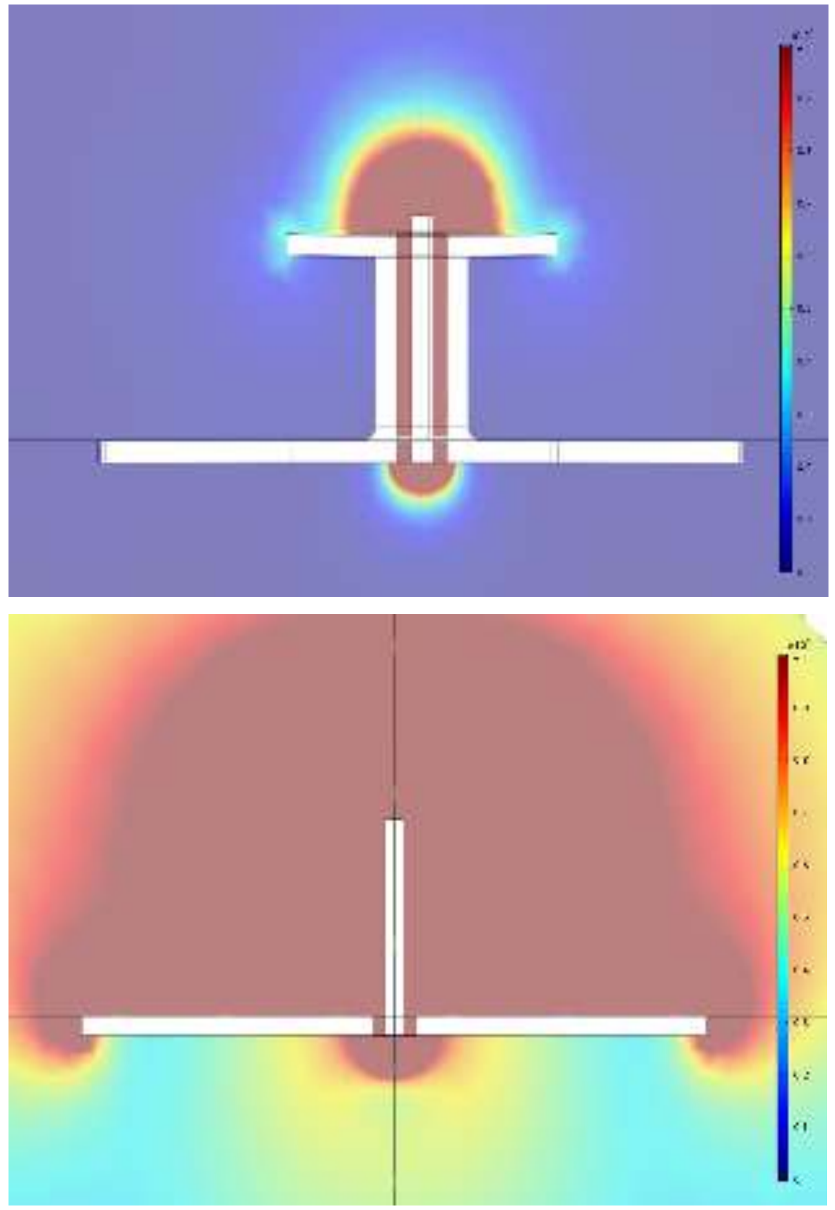

Figure 34 - The Effect of the Yoke on the Electric Field

UNIVERSITY OF Southampton

Antenna Design

The next step in the design process looked in detail at the radiating element. Multiple designs were investigated, with a number inspired by previous research and others that were envisaged independently.

As part of the review of relevant literature, a series of prior designs were found that had been tested before in the application of generating plasma. The results of this work showed that a star-shaped antenna was the best performing of the designs they tested [23], [24], whilst other promising designs included a disc shape and a cross shape. At lower powers, the disc antenna outperformed the star shape, but this was reversed at higher powers. There is a trade-off between how effective the antenna is at radiating power into the plasma and the total surface area of the antenna on which ion recombination can occur [23]. This manifested itself in a further design aim to minimise the surface area of the antenna where possible. Designs taken forward for further study included the following shown in Figure 35.

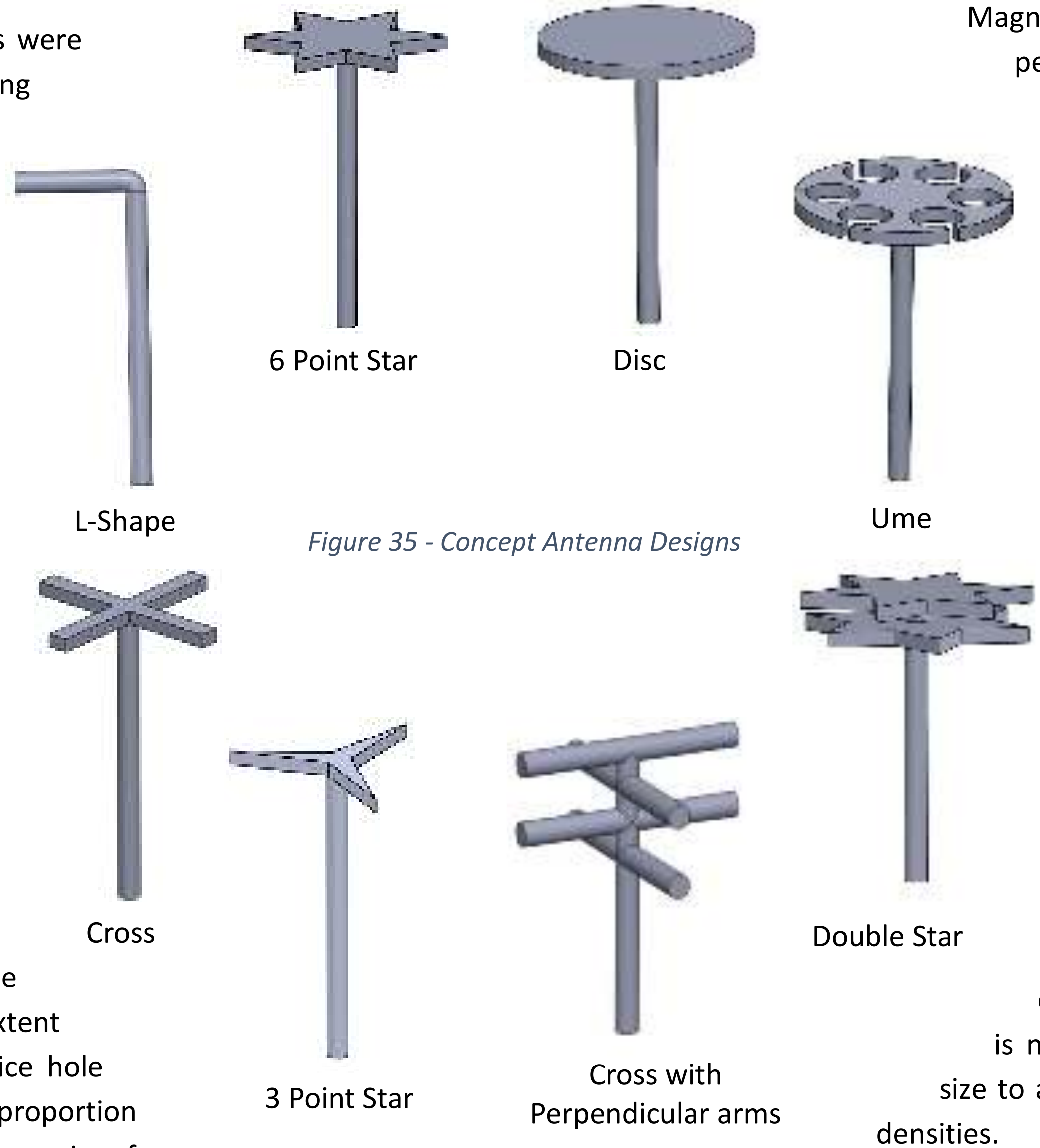

Figure 35 - Concept Antenna Designs

Noting the significant effect of the yoke on the performance of the electric field, the chamber walls and orifice were also simulated, shown in Figure 36. As expected, the electric field is almost entirely contained inside the chamber with minimal penetration of the fin structure. This is due to the 3mm fin spacing being significantly lower than the microwave wavelength of 122mm. A similar result is seen at the orifice to a lesser extent where the 8mm orifice hole blocks a significant proportion of the microwaves escaping from the chamber.

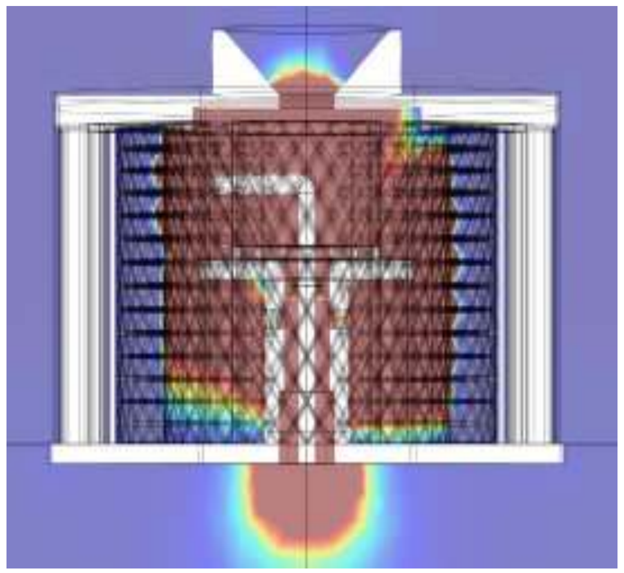
Figure 36 - Full Chamber Simulation (L – Shape)

The addition of the full chamber geometry to the simulation increased the computational requirement of the simulation significantly due to the intricate fin structure. A mesh dependency study was undertaken to try and optimise the mesh without compromising on accuracy. Optimising the mesh helped to reduce the computational cost such that all antennas could be run with full chamber simulations. The elimination of some designs was based on their radiation patterns alone but for others, it was not easy to tell with a visual analysis and required a more accurate assessment of performance characterisation.

Performance Characterisation

As the key performance parameter is the strength of the electric field in the ECR region, developing a method to combine the Antenna Electric field simulations with the Magnetic Field Simulations allowed the assessment of the overall Ionisation performance for each antenna design. A method was developed using the raw exported data from COMSOL to effectively integrate the Electric Field Strength over the ECR Surface. In order to achieve this, the internal volume of the chamber was divided into a mesh (Visualised in Figure 37) comprising of 8 million equally sized elements with each having its 3 positional coordinates (X, Y, Z), a Magnetic Field strength value (B) and an Electric Field strength value (E). Exporting this data from COMSOL into Python allowed us to run a check on every element to see if it was part of the ECR region. A boundary of 10% either side of the resonant field strength (0.07875T – 0.09625T) served to account for the off-resonance condition where sufficient energy can still be absorbed by the free electrons and ionisation can still occur. This was based on a number of different research papers arriving at roughly similar ranges [25], [26], [27]. If a mesh element is determined to be part of the ECR region then the elements electric field strength is summed together with all other ECR elements. Finally, the total is normalised by the element size to account for different mesh densities.

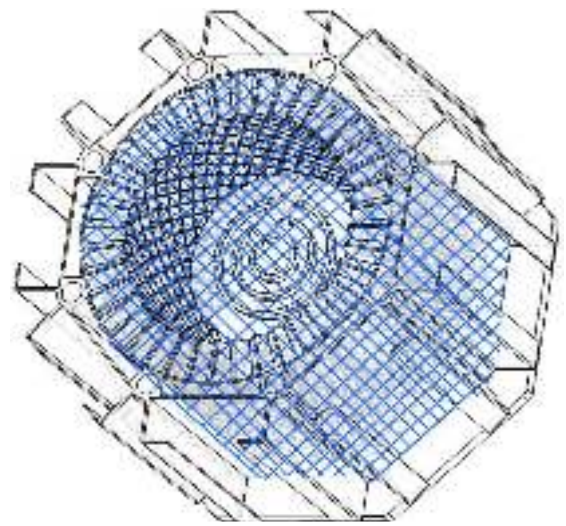
Figure 37 - Mesh Visualisation

This method of characterisation resulted in a numerical value that allowed for easy comparison between the different yoke and antenna configurations in order to maximise our ECR Performance, and therefore ionisation rate. This was taken forward to assist with the decision of optimal antenna selection.

Final Antenna Designs

The performance metric allowed for a better understanding of the electric field within the discharge chamber. This allowed progression to manufacture using numerical data

Figure 39 below shows the 3 best designs as according to the ECR Performance metric developed above. The 3 and 4 Point star designs were similar in performance, however it was decided to move to manufacture with the 3 Point star design due to a slightly improved performance metric and lower surface area. Although the L-shape antenna has a highly one directional radiation pattern as shown in Figure 39 the design was carried forward to production due to its high score in the performance metric.

Figure 38 - The final antenna options

It is important to consider that there may be some localised thermal issues with this design due to the highly energetic plasma in one region. Finally, the 6 Point Star was chosen due to also having a relatively high-performance metric, but more importantly a much more uniform radiation pattern which should lead to a more uniform distribution of plasma production within the chamber. The final manufactured components are shown in Figure 38 where you can clearly see the threaded end that fixes the antenna to the 7/16th coaxial connection at the base of the chamber.

Antenna (Image and Description)		Electric Field Side View	Electric Field Top View (0 - 1000V/m)	Electric Field Top View (0 - 10000V/m)	ECR Performance Metric Value (KVmm^2)
	3 Point star	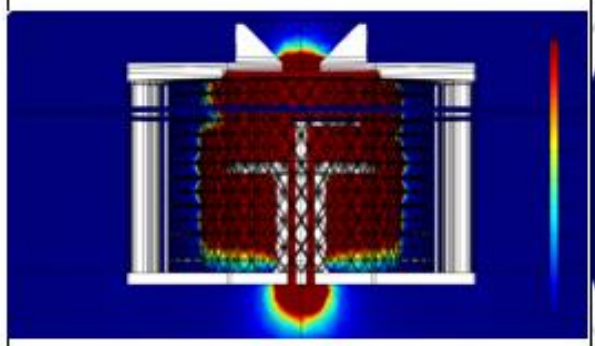	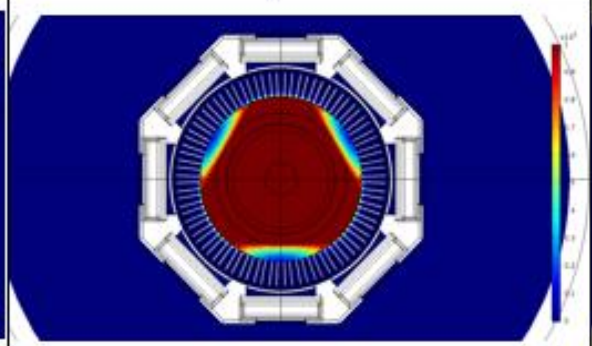	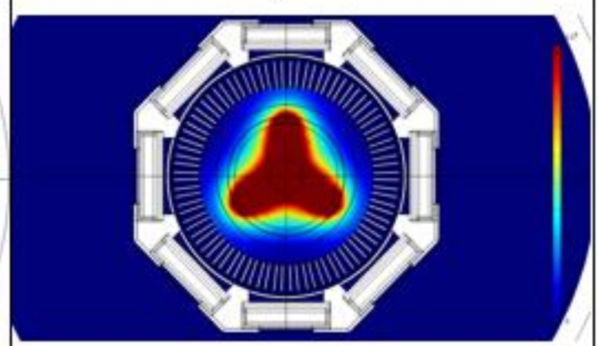	9200KVmm^2
	L- Shape	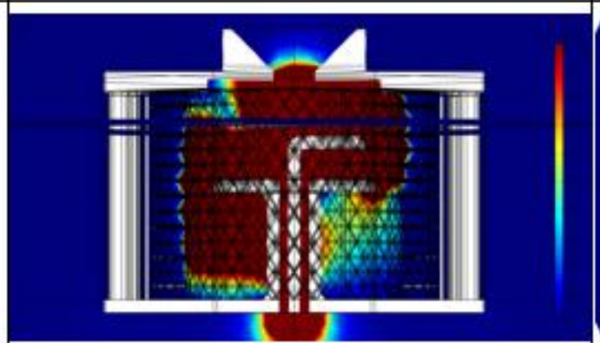	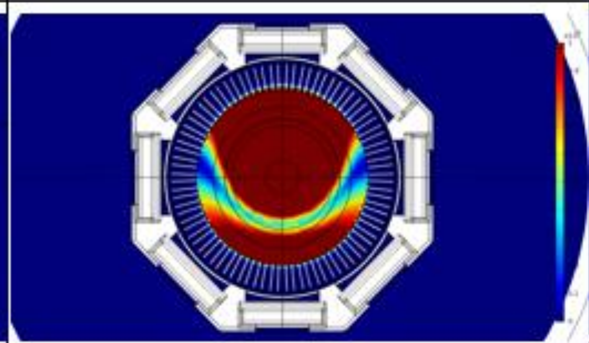	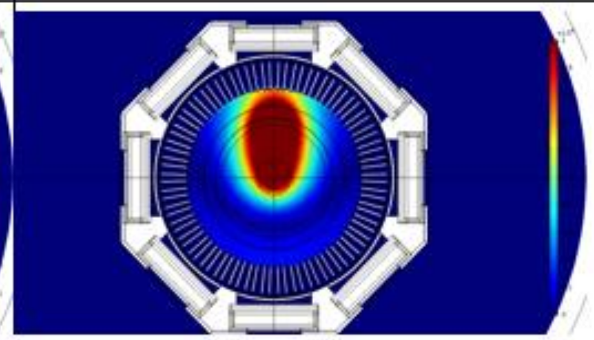	7940KVmm^2
	6 Point star	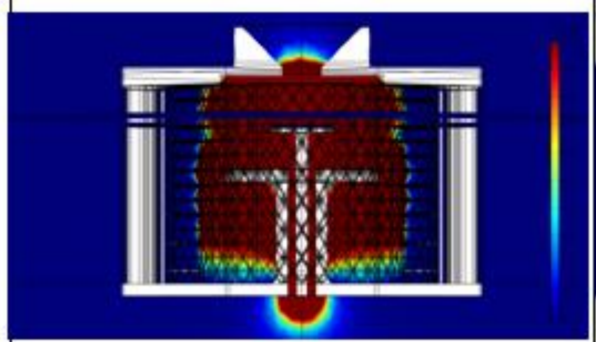	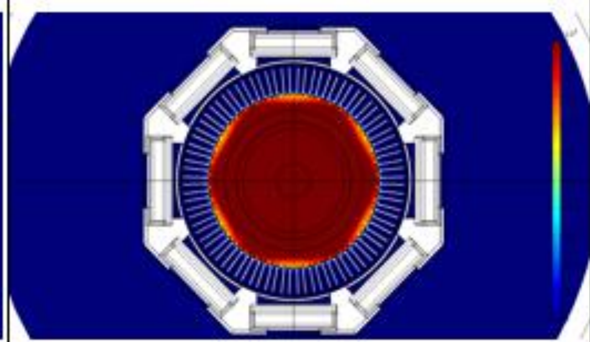	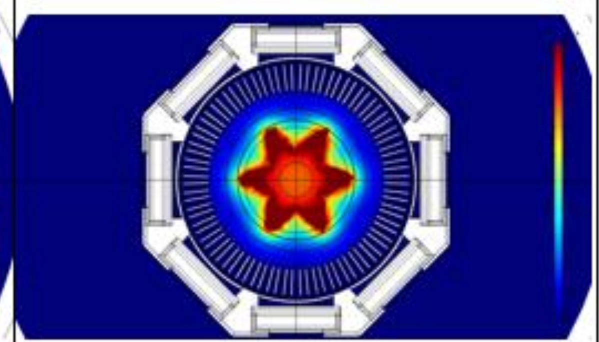	6200KVmm^2

Figure 39 - The electric field visualisations and performance metric

UNIVERSITY OF Southampton

Thermal and Electrical Considerations

Thermal Insulation

The N45H neodymium magnets that were chosen for the neutraliser have a maximum operating temperature of 120 ºC and a Curie temperature of 320 ºC. As the expected temperatures in the neutraliser exceed 250 ºC, the magnets needed to be thermally insulated to keep their temperature within the operating limit. After running a number of simulations with different insulation materials and thicknesses, the thermal insulation chosen was a Calcium Magnesium Silicate sheet of 4 mm thickness and thermal conductivities, which offered similar performance to Microtherm at a reduced cost.

This thermal insulation is made from superwool 607 HT [28] fibres bonded with a low percentage of organic binder. This material is rather powdery with air pockets, which meant that it would shrink to much lower thicknesses following a vacuum cycle. To account for this, several insulation sheets were compressed together in order to remove any air voids and achieve the right thickness. They were then wrapped in Kapton tape to protect the magnets and the chamber walls from any particulate off products.

Figure 41 shows the configuration of the insulation around the magnets. The Calcium Magnesium Silicate insulation sheet is placed in between the magnets and the chamber walls, and a 1 mm thickness PTFE sleeve surrounds the other sides of the magnets that are in contact with the chamber. The thermal simulations, performed with Ansys, were set up with this configuration for a range of temperatures for the ECR region heat source, making a total of five sets of temperature data. The simulations calculated the temperature at every point in the neutraliser during one hour of continuous operation. Figure 40 illustrates the rate at which the maximum and minimum temperatures of the magnets increase with time, for the maximum expected ECR region temperature case. It's apparent that the temperature change rate decreases dramatically with time, and therefore the temperatures obtained from the model can be taken as steady-state temperatures.

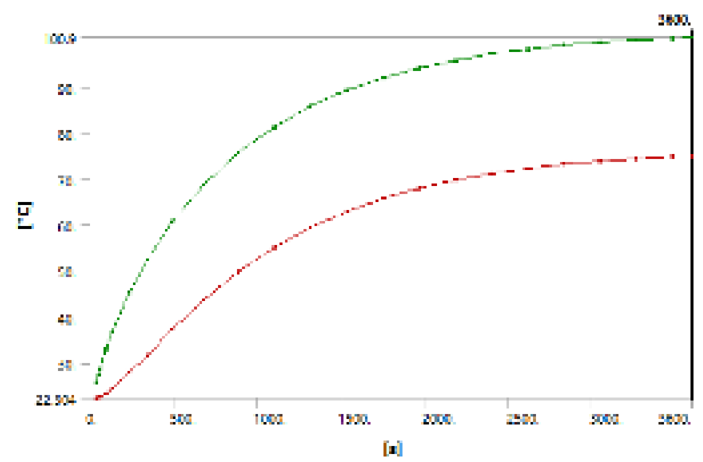

Figure 40 - Transient thermal solution for ECR temp. = 500

The predictions for magnet temperature obtained from the simulations have a maximum of 100 ºC, which means that the margin for reversible de-magnetisation is at least 20 ºC, and may be higher if the maximum expected ECR region temperatures are lower than expected. The Curie point is 320 ºC, so the margin for irreversible demagnetisation is over 200 ºC, and complete demagnetisation is therefore very unlikely.

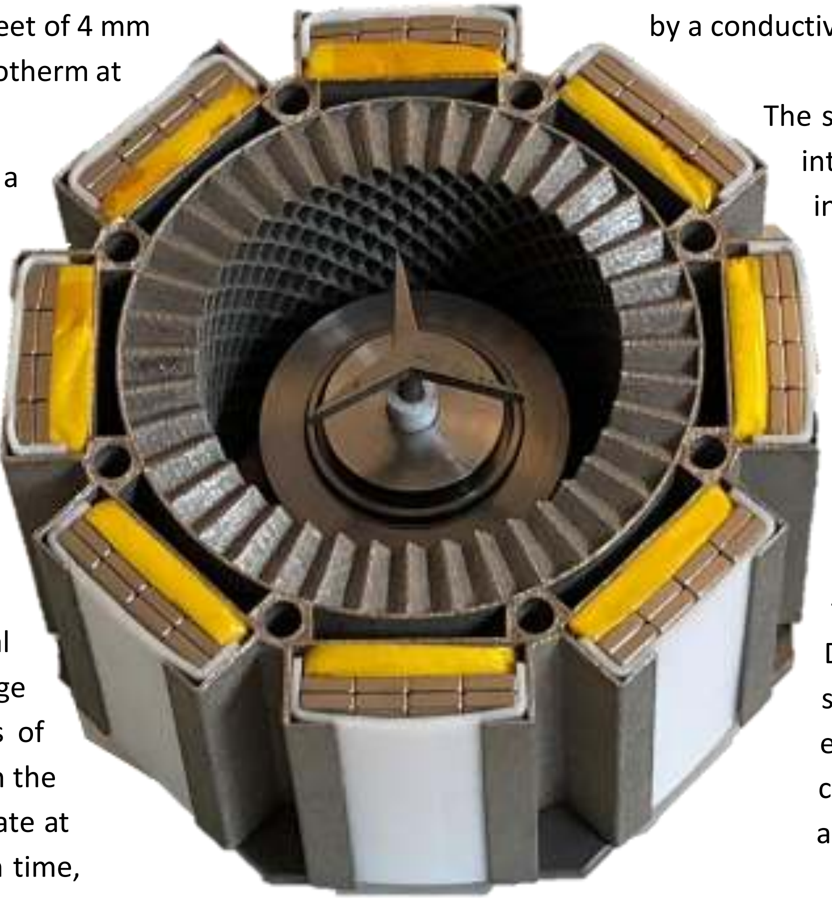

Figure 41 - Thermal Insulation covering the magnet assemblies, and the Antenna Shield in place above the main yoke and below the antenna.

Antenna Shield

One of the main constraints on the neutraliser assembly design was the electrical insulation of the key components. For the antenna, this was achieved by placing it in a protective PTFE sleeve that was then inserted into the magnetic yoke. However, due to ion re-deposition, a specially designed shield had to be implemented in place of the PTFE sleeve. This served to protect the insulation from being coated by a conductive layer creating a short between the antenna and the rest of the chamber.

The shield was designed manufactured from stainless steel for strength and was intended to be coated with plasma sprayed ceramic layer for electrical insulation. In combination with the grooves on the upper side of the yoke, it creates a protective barrier that does not allow the ambient plasma to come into contact with a significant area of the insulation layer, as shown in Figure 42. To achieve this, the distance between the shield walls must be less than the plasma Debye sheath, which is described by the equation below.

$$Debye\ Sheath, s = \lambda_D \times 20$$

Where λ_D represents the Debye length. This ensures that the plasma 'sees' the gap as a solid wall and cannot penetrate it. In this scenario, the minimum Debye sheath was calculated to be 2 mm, therefore the distance between the shield walls was set to 1 mm for safety. This setup prevents plasma from entering the grooves between the shield and the magnetic yoke, making the complete coating of the insulation layer impossible and thus ensuring that the antenna is electrically isolated from the rest of the chamber.

Due to cost constraints, the Antenna Shield was never coated with ceramic, and was substituted with PTFE during the testing period. If this design were to be taken forward, the top shield could be manufactured out of one piece of ceramic, should the budget allow, or be manufactured from steel and sprayed as was intended for this design. For short duration ground testing, this would be an appropriate interim.

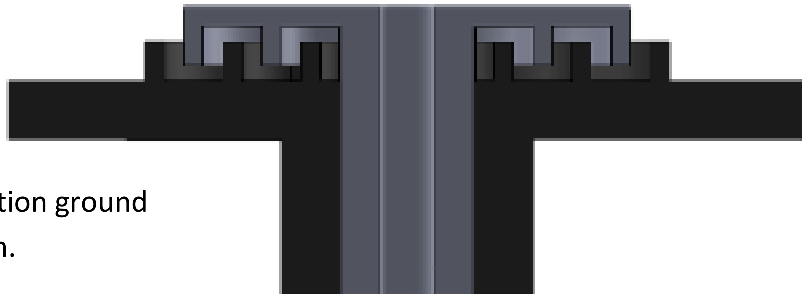

Figure 42 - SolidWorks cutaway of the Antenna Shield

Faraday Cage

The primary role of the Faraday Cage is to encapsulate the neutraliser and act as a barrier to any ambient plasma which could interfere with the operation of the neutraliser, as well as preventing any microwaves from escaping the neutraliser. The cage must interface to rest of the neutraliser assembly while remaining isolated from the internal neutraliser components. The dimensions and shape of the Faraday Cage were constrained by the design requirement of making the modular with the thruster. Thus, the height and width of the cage faces were set equal to one face of the thruster Faraday Cage.

The primary design challenge was to produce something which could be easily and reliably manufactured. To fulfil its roles, the cage required a grid of holes on each face. Although complicated geometry such as this could be manufactured additively, in the final product the hole grids would sit in 3 orthogonal planes. Thus, it was undesirable to print the cage as a single part, as this would lead to a poor build quality.

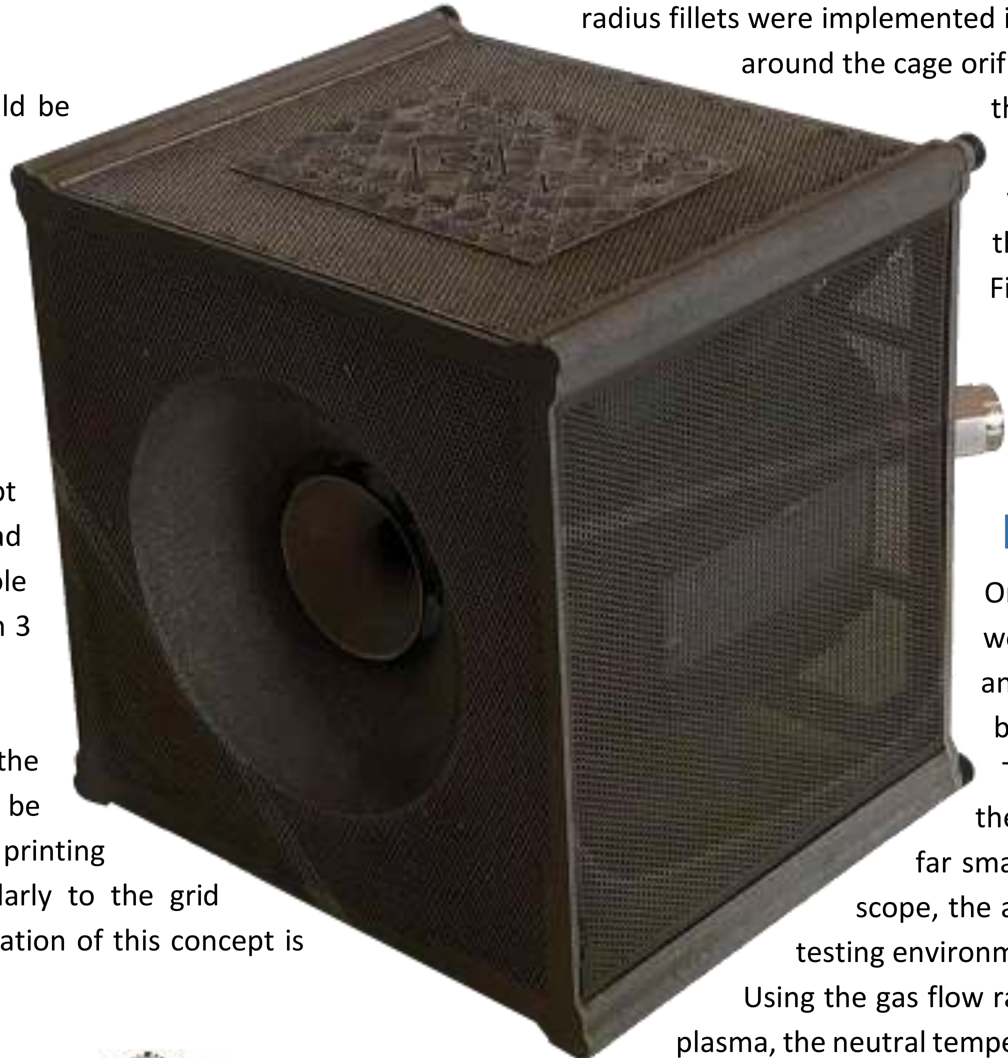

Concept

The Faraday Cage required a grid of small-scale holes on all faces except the backplate. Attempting to print these hole grids 'upwards' would lead to a poor build quality, due to the overarching nature of the hole geometry. This posed issues, as the hole geometries were required in 3 orthogonal planes.

To avoid printing complicated geometry in the wrong orientation, the design concept split the cage into separate parts. These parts would be manufactured separately and then assembled. The concept involved printing each face alone in the optimum orientation (building perpendicularly to the grid pattern). These faces would slide into a base structure. The first iteration of this concept is shown in Figure 43.

Figure 43 - The first iteration of the multi-component Faraday Cage design concept.

Detailed Design

The design of the cage progressed through several iterations. The design of the columns was altered to reduce mass, and the faces were thinned to a thickness of 0.5mm. A tapered profile on both the columns and faces (Figure 44) allowed a seamless external cage profile without the need for support columns during manufacture. Whereas before the backplate would be secured to the cage with nuts and bolts, the updated design allowed the columns to incorporate threaded holes, thus minimising geometric discontinuities on the outside of the cage and simplifying manufacture.

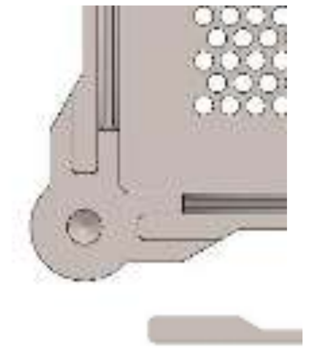

Figure 44 - Tapered profile of columns (top) and faces (bottom)

To increase the structural rigidity of the cage base, support struts and large radius fillets were implemented in the design. A nozzle profile was added around the cage orifice, which would help shield electrons as they left the neutraliser, preventing any escaping into the cage. The hole pattern was also extended to the bottom face of the cage. These features are visible in Figure 45

Figure 45 - Side profile of Faraday Cage base, showing the struts and 'nozzle.'

Hole Sizing

One of the key parameters of the cage design was the hole sizing. These would need to be small enough to act as a barrier to the ambient plasma and microwaves. Making them too small would result in unnecessary mass being added to the cage.

The size of the holes was calculated based on the Debye sheath length of the radiation to be shielded. Of the two, the ambient plasma would have a far smaller Debye length and was thus the controlling variable. For the project scope, the ambient plasma characteristics would be calculated in the context of the testing environment, that is the university vacuum chamber.

Using the gas flow rate into the vacuum chamber (from the neutraliser) and assuming a cold plasma, the neutral temperature and neutral density were calculated. From this, the electron temperature was calculated, and thus the Debye length was found to be 0.45mm. The sheath length is generally a multiple of several Debye lengths. To be safe, the hole diameter was chosen as 0.9mm, twice the Debye length.

The hole spacing was determined by the manufacturing capabilities of the SLM printer. The minimum geometry thickness which could be made was 0.2mm. To leave a margin of safety, the minimum spacing between the holes was set at 0.3mm. A sample of the hole pattern is shown in Figure 46.

Figure 46 - Hole grid detail

Back Plate and Mounting

The backplate was the main structural component of the neutraliser. It provided an interface point between the internal neutraliser components, the Faraday cage, and the test GSE. Along with these structural requirements, the backplate also had to provide electrical isolation between each of the segments mentioned and accommodate electrical connections to the neutraliser.

Backplate

The backplate design started out as a simple plate with 8 holes to accommodate interfaces to the neutraliser components. The profile of the backplate was changed to match that of the Faraday Cage, and the material between the holes was hollowed out to reduce mass. A supporting rib was added around the holes which would interface to the test GSE, to improve structural characteristics. Finally, the number of holes was reduced to 4, as extra space was required to accommodate the propellant inlet. This resulted in the final iteration of the design as shown. Initially the intention was to make use of additive manufacturing for this component, however, following discussion with the EDMC, it was advised we manufacture the back plate using traditional methods due to delays in the additive manufacturing process. As the key role of the backplate was to maintain the position of the neutraliser within the Faraday Cage, analysis of structural response allowed the component mass to be reduced.

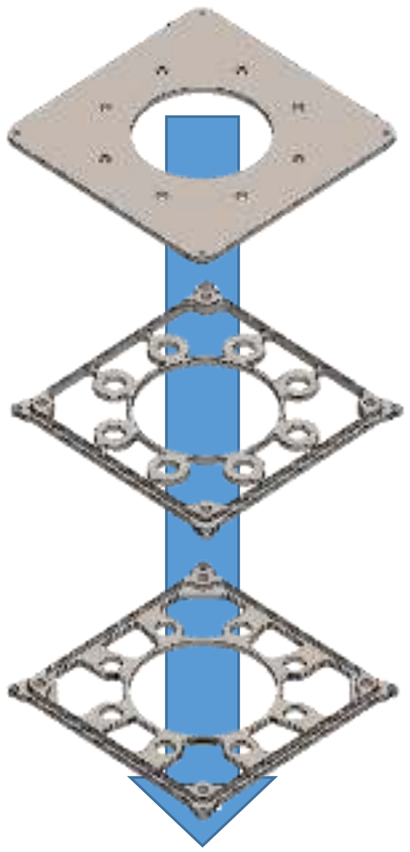

Isolation

To achieve electrical isolation between the backplate and the neutraliser, off-the-shelf ceramic bushings were employed. The bushings are formed of a male and a female part, with holes to allow a bolt to pass through. The backplate sits between the bushings, isolating it from the fastening bolt

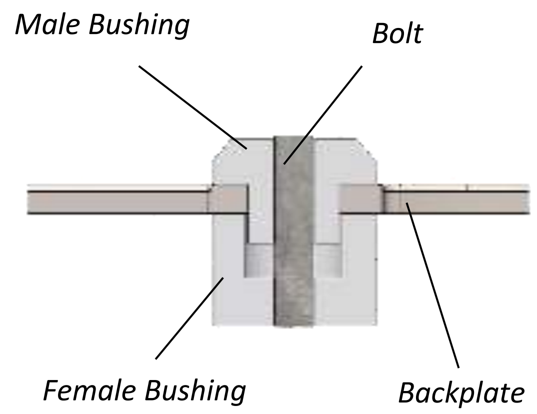

Mounting

One of the backplate's primary roles is to mount the neutraliser to the test GSE, which was designed by PhD student David Hoffman. The setup is formed of a large interface plate mounted on an assembly of Bosch Rexroth bars. The backplate must also be electrically isolated from this interface plate. This was achieved by using custom-made tapped PTFE spacers. The spacers interface to bolts protruding from the top of the backplate, with the other ends connecting to the bolts on the test setup. In this way the backplate is connected to the test setup without the connecting bolts touching, isolating the two parts. The design performed well during testing, serving to support the assembly during regular movement of the test rig, and isolated the neutraliser assembly from the test rig and faraday cage. The design steps shown in Figure 47 track the design considerations through to the final mounting.

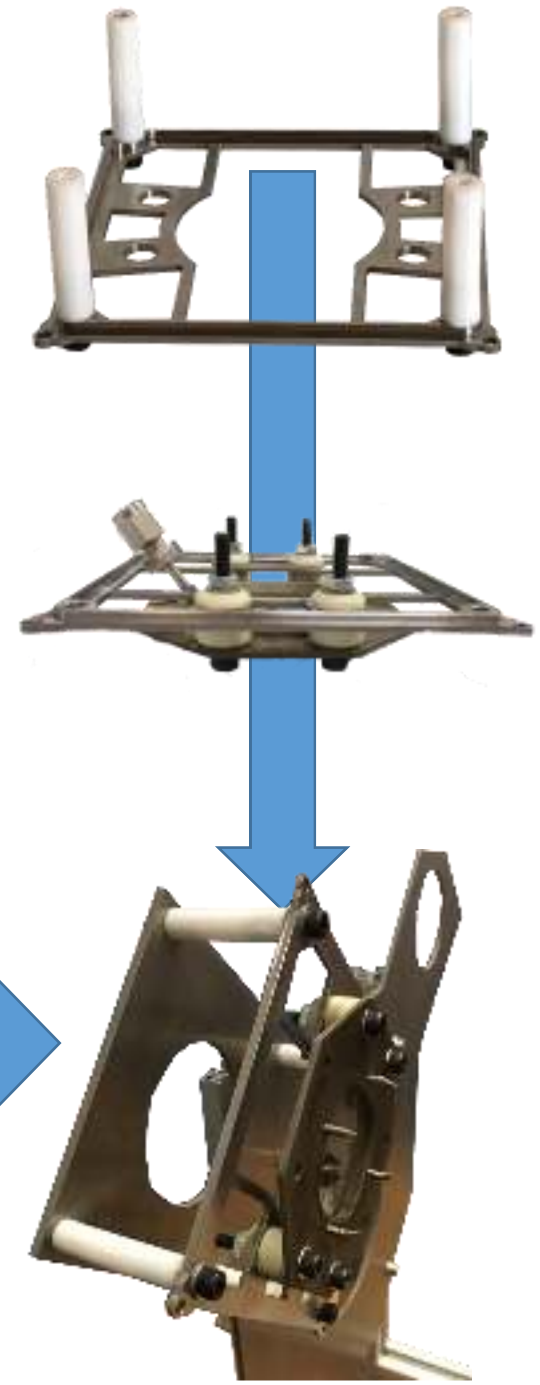

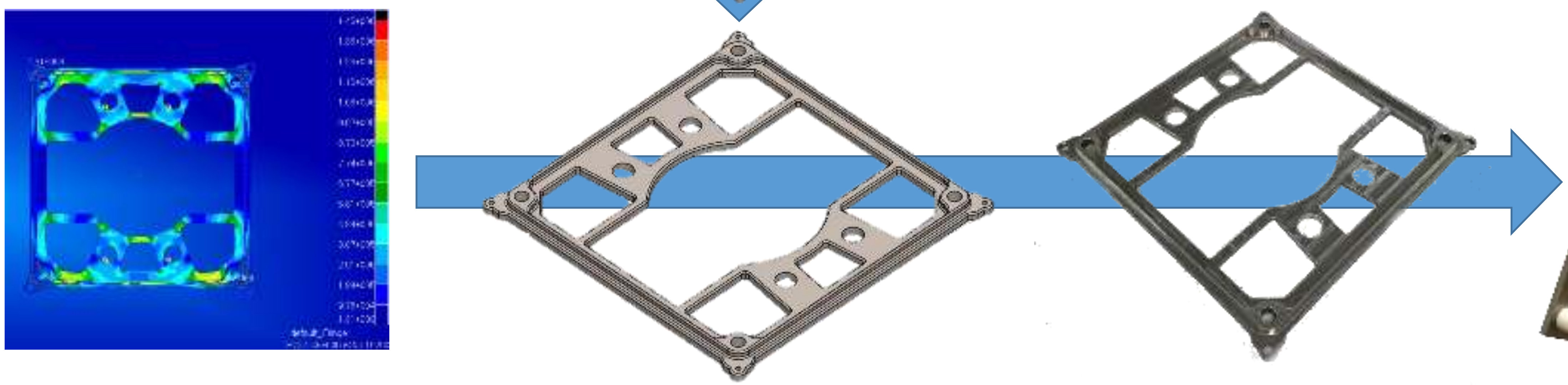

Figure 47 - Design process of the backplate, considering structural performance (left) and electrical isolation (right)

Engineering Decisions for Manufacture

The design of many of the components was influenced in some way by the manufacturing processes. As part of the project goals, additive manufacturing was to be used to produce most of the primary stainless-steel components. Both the advantages and limitations of the method were factored into the design process of these components. The iron components were not suitable for additive manufacture, and so provided their own manufacturing challenges.

Additive Manufacturing

Additive manufacturing is a technology under continual development with the potential to manufacture components that could not be practically or realistically produced by traditional methods. By using less material to print each part compared with traditional machining, cost of components is reduced significantly. For this project, an additive manufacturing method known as Selective Laser Melting (SLM) was used to produce components in 316L stainless steel, using an M2 Cusing Concept Laser. In SLM, a CAD model of the component is split into layers. For each one, a layer of stainless steel powder is deposited by the printer, and a laser fuses this powder into a solid at the points where the geometry is required. This process repeats layer-by-layer to build up the component. However, there are some limitations to the technology:

- There is a maximum build angle for geometry (45°), above which support material is required to build the geometry. This support material increases the cost and time of manufacture.
- Any trapped volume must have some sort of opening, otherwise, the powdered material cannot be removed.
- The final component must be cut away from the build base, which can lead to warping.
- The printer may not produce holes as perfect circles. For any holes requiring tapping, a smaller pilot hole should be printed and then drilled out for tapping.

Orifice Plate

The design of the orifice plates included a nozzle-like profile radiating from the orifice. The original design implemented this nozzle with a supporting wall around it. The intermediary volume was hollowed out to save mass, creating a trapped volume. However, the trapped volume had no opening, thus the powder deposited by the printer during the building process would be irremovably trapped within. To avoid this issue, the design instead made use of 8 columns, which would support the nozzle profile without a trapped volume. The progression of the design is shown in Figure 48.

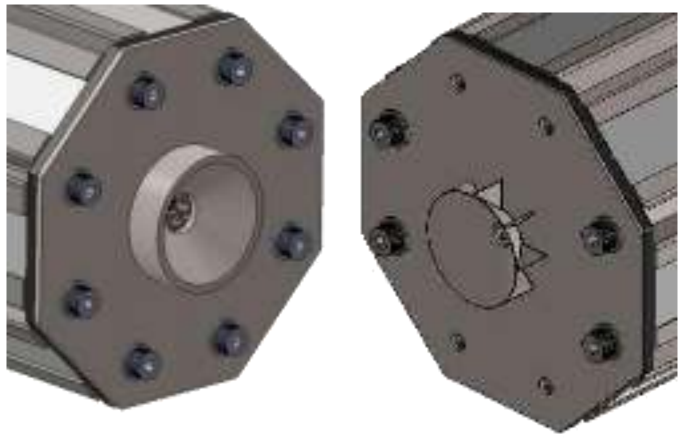

Figure 48 - Original (left) and final (right) designs of the orifice plate

Discharge Chamber

The complicated geometry of the discharge chamber walls necessitated the use of additive manufacturing. The design consisted of several crisscrossing grids which formed the internal surface of the chamber. To avoid any support columns, the grids were designed at an angle of 54° to the horizontal, safely above the minimum limit. The remainder of the chamber was also designed with a constant cross-section in order to minimise any manufacturing issues.

Reservoir Plate

The propellant delivery system required an airtight seal between the propellant reservoir and the nozzles. This was achieved by exploiting the ability of the SLM printer to create trapped volumes. The raised reservoir ring and the plate were printed as a single piece, with the nozzle holes providing an orifice through which the excess powder could be drained. The reservoir ring was designed at a steep enough angle to avoid the use of support columns. A cross section of the plate reservoir design is shown in Figure 49. The cross-section shows the profile of the reservoir ring, the interface to the propellant inlet, and one of the nozzle holes. Such a design would not be possible with traditional manufacturing methods.

Figure 49 - Cross-sectional design of the reservoir plate

Faraday Cage

Complicated grid geometry on the faces of the Faraday Cage necessitated an innovative design approach. Printing the cage as a single part would result in poor build quality of the grids on the vertical faces. To bypass this issue, the cage design was split into parts, with each of the vertical faces printed separately, and then assembled. The optimum printing orientation for these grids is shown in Figure 50.

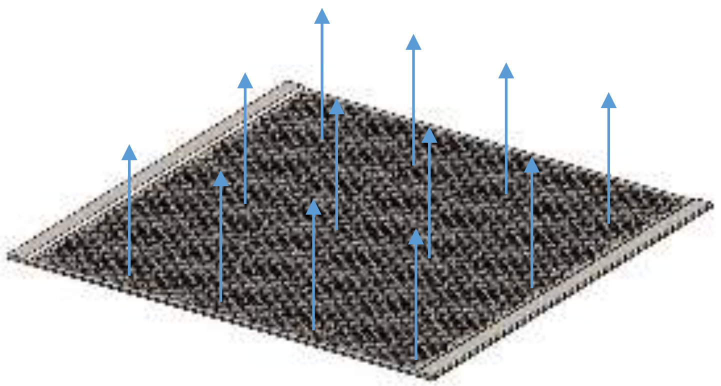

Figure 50 - Optimum print direction of Faraday Cage hole grids

Iron Yokes

The yokes were the only main component which could not be additively manufactured. Instead, they would be machined from 99.8% iron, a material chosen for its magnetic characteristics. The manufacturing limitations of the material impacted the design of the yoke, which in turn influenced the design of several other components. A 'split yoke' concept (where the yoke would be manufactured in two halves) was rejected, as this would double our material usage and technician time compared to a single piece design. This led to the decision to join the antenna and coaxial port with a threaded connection. The nozzles were introduced into the design as sufficiently small holes could not be drilled in the iron. The iron components required a post-manufacture vacuum heat treatment process to develop the magnetic properties as required.

Manufacture

The manufacturing part of the project can be broadly split into 3 categories: Additive manufacturing, traditional manufacturing, and workshop tasks. A secondary aim of the project was to demonstrate the feasibility of using additive manufacturing to produce the neutraliser, and this was the main manufacturing method employed. For some other components, it was quicker and cheaper to either make them by traditional methods, or in one of the student workshops.

Additive Manufacturing

Additive manufacturing would take place at the EDMC using the M2 Cusing concept laser. A snapshot of the printing process is shown in Figure 52. There was a significant delay in starting manufacture, as the printer was set up to produce aluminium components. Using aluminium for the neutraliser components was not an option due to the high sputter rate of the material. The switch to stainless-steel was not made until the end of January, significantly pushing back the manufacturing schedule. Most of the additively manufactured components were produced without any issues. However, the nozzles had to be reprinted with a larger diameter hole, as the 0.2mm diameter hole was not built accurately. Due to their small size, they were easily accommodated in the EDMC print schedule. Two stages of the printing process of the Faraday cage base are shown in Figure 51. The change in geometry between the base of the cage (left) and the upper parts of the structure (right) can be seen.

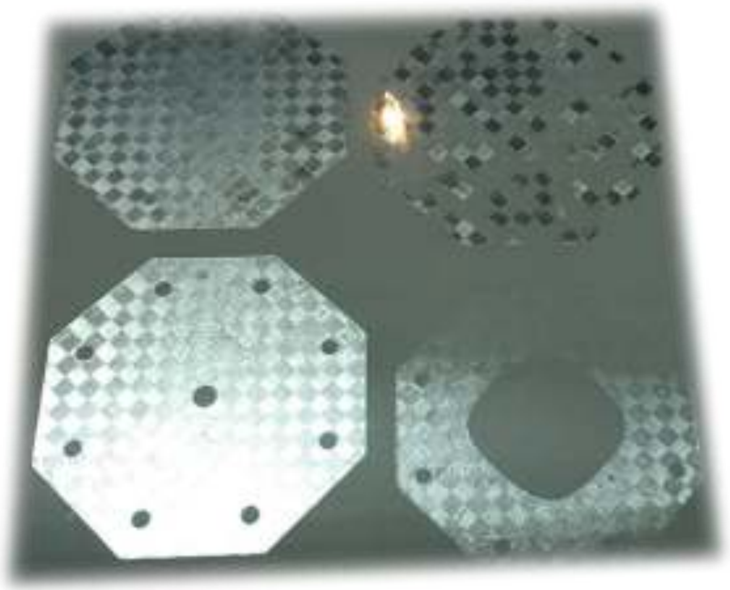

Figure 52 - The printing of the orifice plates and reservoir plate

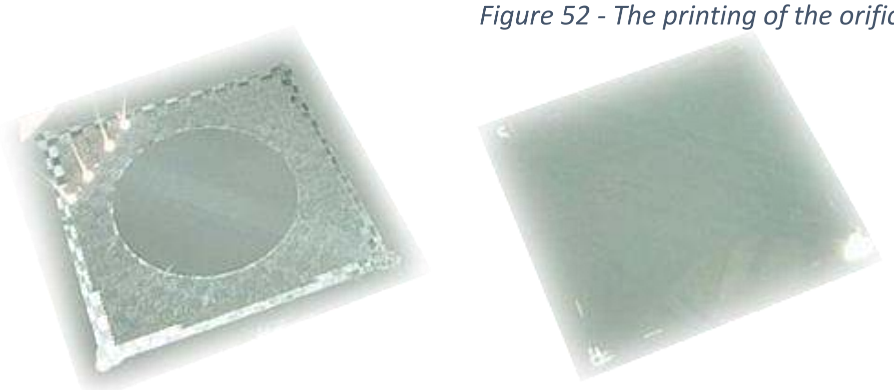

Figure 51 - Two stages of the printing Faraday Cage base. Initial (left) and final (right) stages.

Traditional Manufacturing

Despite the convenience of additive manufacturing, simple components can still be produced quicker and at a lower cost by more traditional methods. For some of our components, there was no reason to use the SLM printer, which was in high demand and had longer lead times. For the backplate, the profile of the component was easily cut out of a stainless-steel plate using a waterjet cutter. The L-shaped antenna was quickly produced by bending a stainless-steel rod.

The iron components had a stringent material requirement, to be iron of 99.8% purity. This material was not stocked by the EDMC, so an alternative source was identified. To bring out the magnetic properties of the iron, a vacuum heat treatment was required. The facilities for this heat treatment process were not available at the university, so an external provider was used instead.

Workshop Tasks

Many of the smaller secondary components and manufacturing tasks did not require specialist technician knowledge for manufacture. To save time and money, these components and tasks were fulfilled by members of the GDP team. These tasks included:

- Lathing, drilling, and tapping the PTFE spacers connecting the neutraliser to the test GSE.
- Drilling out and tapping holes in additively manufactured components.
- Drilling out and threading an off-the-shelf coaxial port, to create a threaded connection with the antennae.
- Laser-cutting PTFE sheets and folding them into sleeves.
- Compressing and packaging the thermal insulation for the magnets.
- Manufacturing additional orifice plates with smaller orifice sizes.
- Manufacturing additional antennae.
- Cutting down stainless steel tubes to act as alternative anodes during testing.
- Cutting down Bosch Rexroth bars to extend the test GSE assembly.
- Cutting down and altering the test-interface plate

Some of these tasks are shown in Figure 53.

Figure 53 - Left to right: Folding the PTFE sleeves, lathing the PTFE rods, manufacturing an alternative testing anode.

Test Setup

The neutraliser was tested in the main vacuum chamber at the universities David Fearn Electric Propulsion Laboratory (Figure 54). The chamber consists of two sections, A large 2m diameter by 4m cylinder with a second smaller cylinder attached on the end. A sliding gate valve separates the two chambers and allows for easy pass-through between the chambers without having to do a full pump cycle. Three pump types are used in conjunction to bring the pressure in the chamber down to near vacuum, two roughing pumps provide the initial pumping capability bringing, the chamber down to a suitable pressure where the turbomolecular pumps and cryopanels (In the case of the large chamber) can be turned on. The turbopumps operate much like any other turbo-machinery, a series of rotating blades are used to impart momentum on any gas molecules that happen to meet the first set of blades, the molecules are then passed back through a series of blades and finally out the exhaust. Finally, in the case of the large chamber, two cryopanels that are held at approximately 20 Kelvin are used to freeze out the remaining molecules, particularly Nitrogen. This array of pumps allows the chamber to achieve pressures as low as 7×10^{-8} millibar with no flow rate into the chamber and maintain pressures as low as 10^{-6} when low (1 – 10 SCCM) flow rates are used. The small chamber on the other hand without a cryopanels can achieve 10^{-6} millibar without any flow and between 10^{-5} – 10^{-4} millibar when the same low flow rates are used. Due to a malfunctioning gate valve the two chambers had to be operated independently of one another, the majority of our testing was carried out in the small hatch due to the limited testing time available, of which a significant amount would have been taken up by the longer pump cycle of the main chamber.

Figure 54- Large Vacuum Chamber in the David Fearn Electric Propulsion Laboratory

The configuration of the test rig can be seen in Figure 55 with the electrical configuration also shown. All electrical connections from the neutraliser ran to a terminal block on the back of the rig to keep the cabling tidy and for ease of changing configuration of the neutraliser. Both the Faraday Cage (Yellow/Green) and chamber (Brown) were grounded to the inside of the vacuum chamber, separate wiring systems were used to allow for the possible biasing of the chamber during a later stage of testing. Finally, the anode plate (Blue) used to draw the beam current was passed through an electrical feed on the chamber door and then run through to the main ground support equipment (GSE). Both the coaxial connector for the microwave supply and the argon fuel line were passed straight through the respective feed-throughs on the chamber door. A similar interface design for the XSEPT thruster can also be seen in Figure 55.

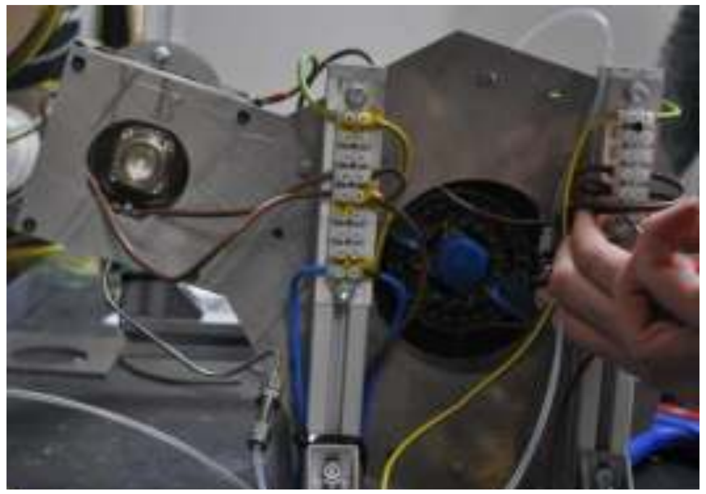

Figure 55 - Electrical Interface for the test rig

Figure 56 shows the ground support equipment used during testing, starting at the bottom of the rack we used a 0 – 300V DC power supply to provide the required voltage to the anode. 2 units up is the mass flow system. Fed by an argon bottle the unit drops the pressure through a series of regulators and valves to 4 bar before feeding it into a computer-controlled mass flow regulator allowing the mass flow to between 0 – 40 SCCM. The second blue power supply is a lower voltage unit (0 -30 V) which was initially used to power a small tungsten filament which would act as a source of free electrons through thermionic emission when heated. This was used to test the anode setup by seeing if we could draw these electrons through the anode. The source of free electrons from the filament was also used to help with the initial ignition of the neutraliser. The anode power supply only read the current to 10mA as the smallest division, so a 6-digit multi-meter was placed in series with the anode which allowed us to read down to a microamp scale. This is shown sat above the main rack. Finally sat again on top of the main rack was the microwave generator, waveguide and triple stub tuner. The microwave power was set using a highly sensitive rotary dial on the front of the unit while the triple stub tuner was used to minimise the reflected power as much as possible.

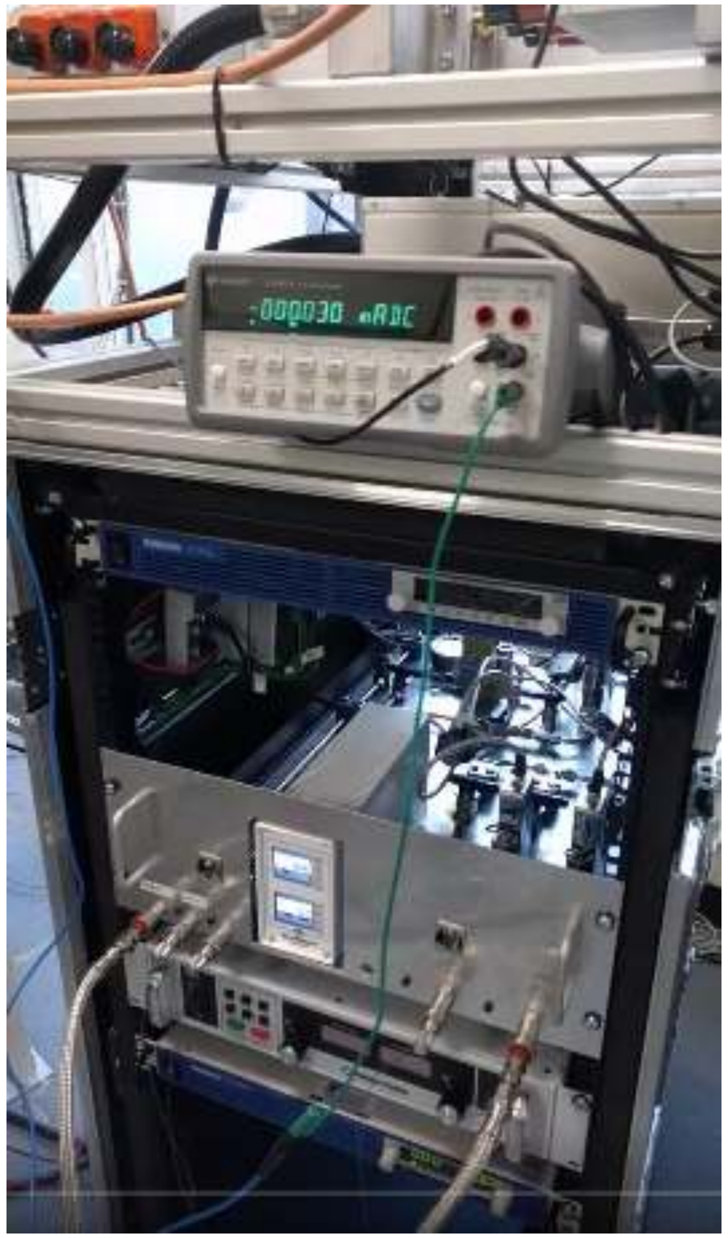

Figure 56 - Ground Support Equipment

In order to make sure the lab was operated safely, attention was paid to the oxygen sensors placed in the lab due to the use of pressurised gas. Provided with the microwave supply was a “wand” used to measure the microwave power per square metre, this was monitored continually to ensure that outside the vacuum chamber any microwave leakage was kept below 5 W/m^2 as outlined by European Regulation.

Commissioning and Testing

The Test Procedure

Testing began with ignition tests performed using the L-shape antenna and an 8mm orifice as this would theoretically provide the easiest to ignite configuration, due to the highly concentrated electric field of the L-shape design. Initial ignition testing was performed with a microwave power sweep conducted between 0 and 100 W and the mass flow rate varied between 0 and 40 SCCM. The anode was held at 50 V during these tests. Unfortunately achieving ignition was initially unsuccessful, even with the use of the filament described previously. The neutraliser was disassembled in order to diagnose the issue and, after obtaining a Gauss meter to measure the axial magnetic field, it was quickly determined that the magnetic field was not behaving as expected. This turned out to be due to the magnet arrays having been arranged incorrectly, with each row of magnets having opposite polarity such that the field lines cancelled out. After rearranging the magnets such that each array had a global north and south, the field was remeasured and the resonant strength of 0.0875 T (0.875 kG) was quickly found in the expected location (Figure 58), effectively verifying our simulation models of the Magnetic Field Topology. With the corrected magnetic field, initiating the plasma discharge became possible. The first successful ignition occurred with the L-shape antenna at 22 W microwave power and a flow rate of 2 SCCM. Completing the ignition testing as intended resulted in a reliable ignition condition being obtained at 30 W and 3 SCCM. This condition was used for all ignitions using the L-shape antenna.

Figure 58 - Verification of the Magnetic Field Topology

Subsequent testing focused on obtaining a full data set for each orifice plate with a power sweep from 0 to 100 W, at flow rates between 0 and 40 SCCM. This was first conducted for the 8 mm orifice and then repeated for the 6 mm orifice plate. Based upon the increase in beam current measured when moving from 8 to 6 mm, a further 4 mm plate was manufactured by hand as an additional configuration. The 8 mm tests showed a distinct saturation of the beam current at flow rates above 5 SCCM so the subsequent 6 and 4 mm tests were done at flow rates between 0 and 5 SCCM.

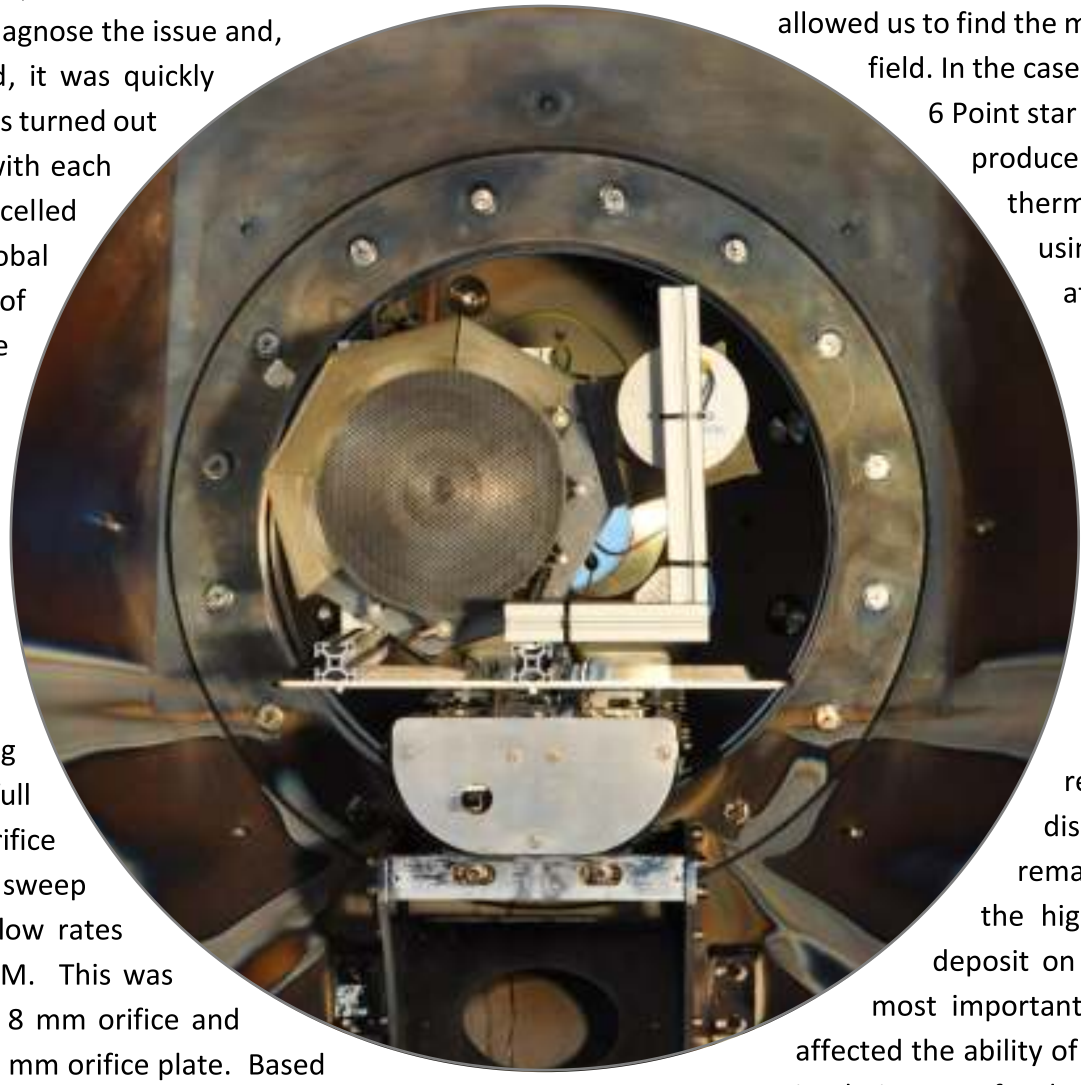

Figure 57 - The test set up inside the vacuum chamber

Having collected data for the different orifice plate sizes the next set of tests investigated the performance of each antenna design. The first attempts igniting the plasma using both the 3-point and 6-point star antennas were unsuccessful. Checking our simulation models, there was a discrepancy between these models and the L-shape model, regarding how the coaxial connection was modelled. Therefore, these simulations were invalid and provided an inaccurate measure of the design's performance. Simulating these with the corrected setup showed a significantly weaker electric field than initially expected and compared to that of the L-Shape. It was therefore not surprising the plasma did not ignite under the same conditions. Simulating the L-Shape antenna at the ignition condition allowed us to see the electric field radiation pattern and strength in the ECR region that produced ignition. Running further simulations on the star designs allowed us to find the microwave power that would be required to achieve the same electric field. In the case of the 3-point star this was found to be at around 200 W and for the 6 Point star it was nearer 380 W. The microwave generator had the capability to produce up to 1 kW continuous power so, while keeping a close eye on thermal stickers placed on the neutraliser, ignition was attempted again using the new predictions. Success was achieved using both antennas, at 180 W for the 3-point star and 350 W for the 6-point star. Although initial models were incorrect, this correlation between the updated model and reality suggests that the new model is suitable to be used for future improvements to the antenna design. No further testing was conducted on these antennas as it was unsustainable to operate at these high powers for long durations due to thermal limitations.

One of the biggest issues encountered during the testing process was the inability to repeat results. It is believed that the lack of repeatability is down to one, or a combination, of the following three reasons. First was the PTFE surrounding the antenna, upon disassembly of the neutraliser it was clear that the amount of PTFE remaining had decreased significantly, almost certainly due to melting at the high temperatures surrounding the antenna. This left a significant deposit on multiple critical surfaces including the antenna, fin structure and most importantly the anode plate. This deposit left on the anode significantly affected the ability of the anode electric field to penetrate the orifice, as described in the simulations run for the orifice plate design. Lower currents were measured as this deposit built up and a substantial increase was observed after removing the deposit from the anode with Acetone. The second identified reason was the control of the microwave generator. It was observed that a significant change in the beam current can occur for just a 1 W change in microwave power. The microwave generator only provides both the forward and reflected power as integer values, meaning a reading of 5 W could be anything between 4.5 W and 5.5 W, between which a significant change in beam current could occur. This meant the 5 W measurement for one configuration could have been taken at 4.5 W and a second configuration at 5.5 W. As a result the data could not be easily repeated.

The microwave power was tuned for every reading to try and minimise reflected power, which was again given as an integer value. This results in a second parameter of control that could introduce an additional 0.5W error. The third and final reason identified was thermal degradation of the magnetic field during long-term operation. Thermally activated stickers placed on the outside of the magnet array hit temperatures of 110 degrees during longer duration tests suggesting that temperatures on the inward facing side of the magnets may well have hit temperatures more than 120 degrees, where reversible degradation begins to occur. As the magnet temperature increased through the region of reversibility, the ECR surface would have shrunk and therefore the ionisation rate and beam current would drop accordingly.

New thermal stickers were placed on both sides of the insulation to give a better assessment of the thermal performance. The Neutraliser was left operating at constant conditions for a 1 hour run at a 15 W microwave power. It was anticipated that a temperature gradient would be seen across the insulation, with the side facing the chamber indicating a higher temperature than that of the magnets. Unfortunately, this was not the case as both stickers showed identical results with a peak temperature of 82 degrees Celsius. This was not the peak temperature reached in all tests due to the short duration and low power but acted as a test to determine the thermal performance. A small temperature gradient may have existed that was not measurable due to the step size of the thermal stickers, however, the insulation did not behave as required. This was anticipated during the manufacturing phase, as it was suspected that the materials thermal properties came from the air content within. The compression of multiple layers to achieve the required thickness and remove the air before entering the vacuum likely affected the thermal properties. This was obviously not suitable for a vacuum environment and will need to be replaced in a future iteration.

After cleaning the anode plate, it was clear that the anode could have a significant impact on the result of each test and should be investigated further. Measurements were repeated for both the 8 and 6 mm orifice plates, ensuring that the anode plate was thoroughly cleaned between each cycle in the vacuum chamber. The effects of anode voltage and anode shape were also investigated, with the use of a cylindrical tube which would better represent the ion beam of the thruster. This is due to the greater surface area allowing a greater current to be drawn.

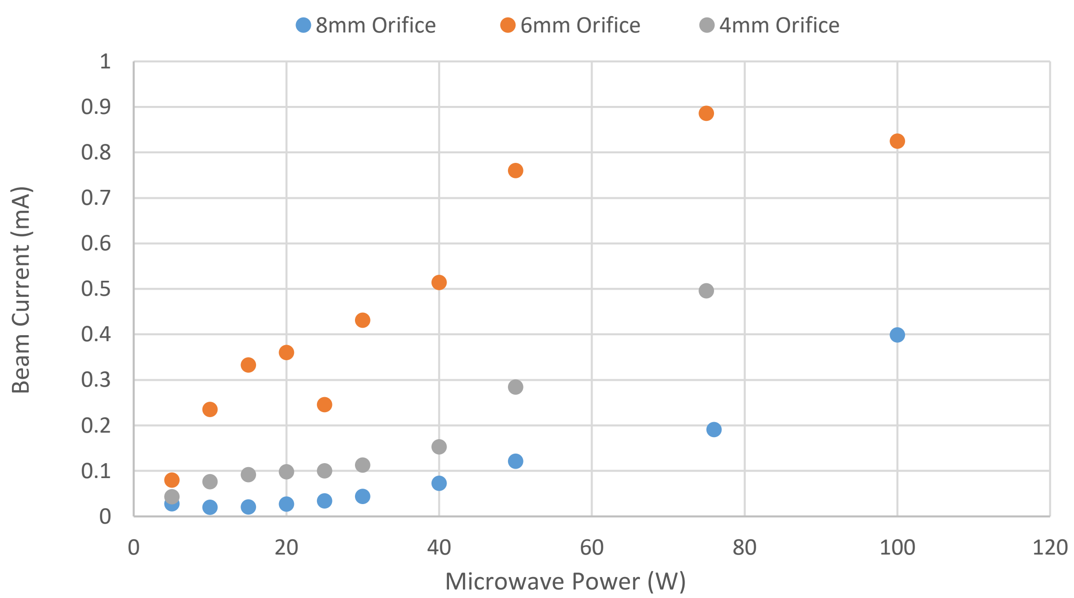

Figure 59 - The effect of the Orifice Plate on Beam Current (Dirty Anode / 1 SCCM

Results

Figure 59 and Figure 60 clearly show the effect of the orifice plate on the beam current. Figure 59 shows the case described previously with a PTFE deposit formed on the anode, while Figure 60 shows the case after cleaning. The results in Figure 59 initially suggest the 6mm orifice plate allows for the greatest current, however, there is a clear difference in trend between the 8 and 4mm configuration and that of the 6mm. This is almost certainly due to the 6 mm orifice being the first of these three configurations tested, when deposit build-up on the anode would have been lower. Figure 60 provides a much greater insight into the effect of the orifice, even though only two orifice sizes were tested under these conditions. Clearly the trends shown for both orifice plates align strongly, with a rapid increase in current between 0 to 20 W microwave power, plateauing until around 50 W, before giving another strong increase in current. It is anticipated that this is due to a change in plasma mode, moving from "glow mode" to "plume mode". In glow mode the electrons are pulled out of the neutraliser chamber by the anode plate, while the plasma stays primarily enclosed in the chamber. At certain operating conditions this will transition to plume mode, where a plume of plasma will exit the chamber and form a bridge between the chamber and the anode plate. The strong trend alignment between the 8 and 4mm orifice sizes in Figure 59 is notable, and although the values are inaccurate, the trend is still useful. This suggests that if the 4 mm was tested again under the conditions in Figure 60, a similar improvement to the beam current would likely be seen from 6 to 4 mm, as was seen from 8 to 6 mm. The likely explanation for this increase in beam current with a reducing orifice size, is the increased pressure in the discharge chamber, and hence an increased number of neutral atoms. The greater the number of neutral atoms, the more likely it is that a collision with a highly energetic primary electron will occur. This in turn increases the ionisation rate, and hence a higher beam current is observed. Figure 61 shows the change in beam current with and without a PTFE deposit on the anode. It also illustrates the improvement seen by switching to the cylindrical anode, due to its greater surface area. It is immediately obvious that results taken under the dirty anode condition can only be interpreted for the trends they present, as the numerical values of any results are clearly inaccurate.

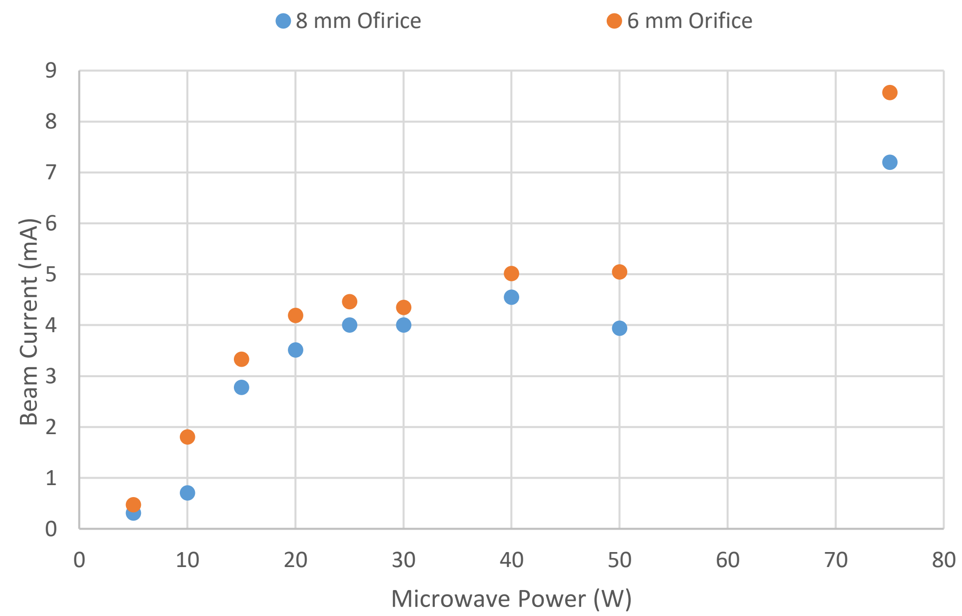

Figure 60 - The effect of the Orifice Plate on Beam Current (Clean Anode / 1 SCCM Flow Rate / L-Shape

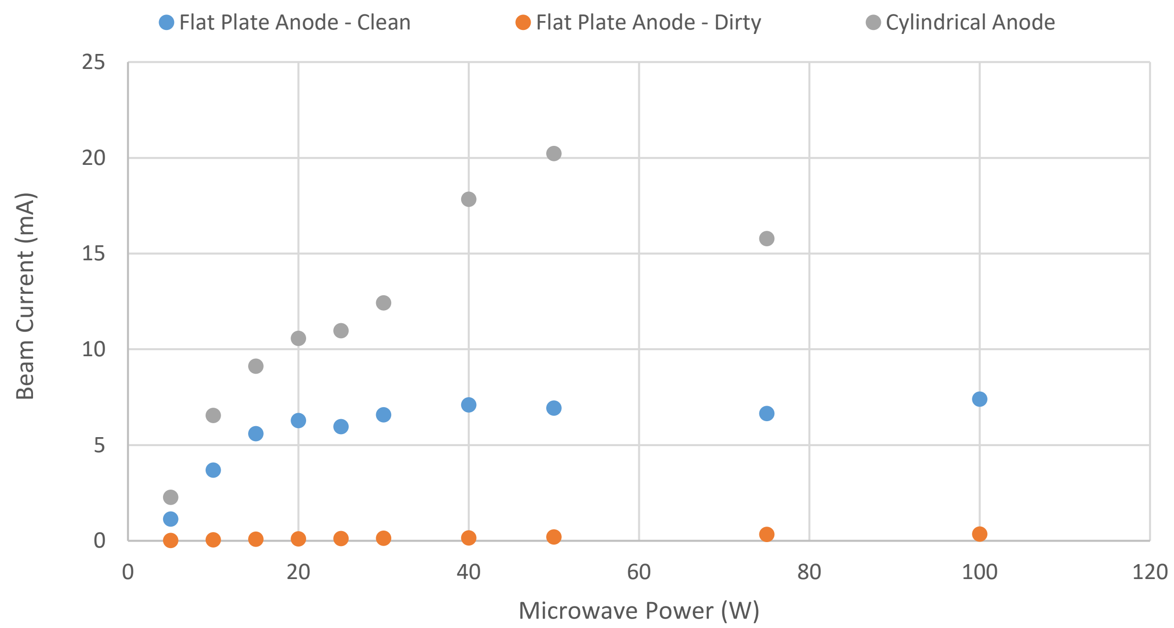

Figure 61 - The effect of anode configuration on Beam Current

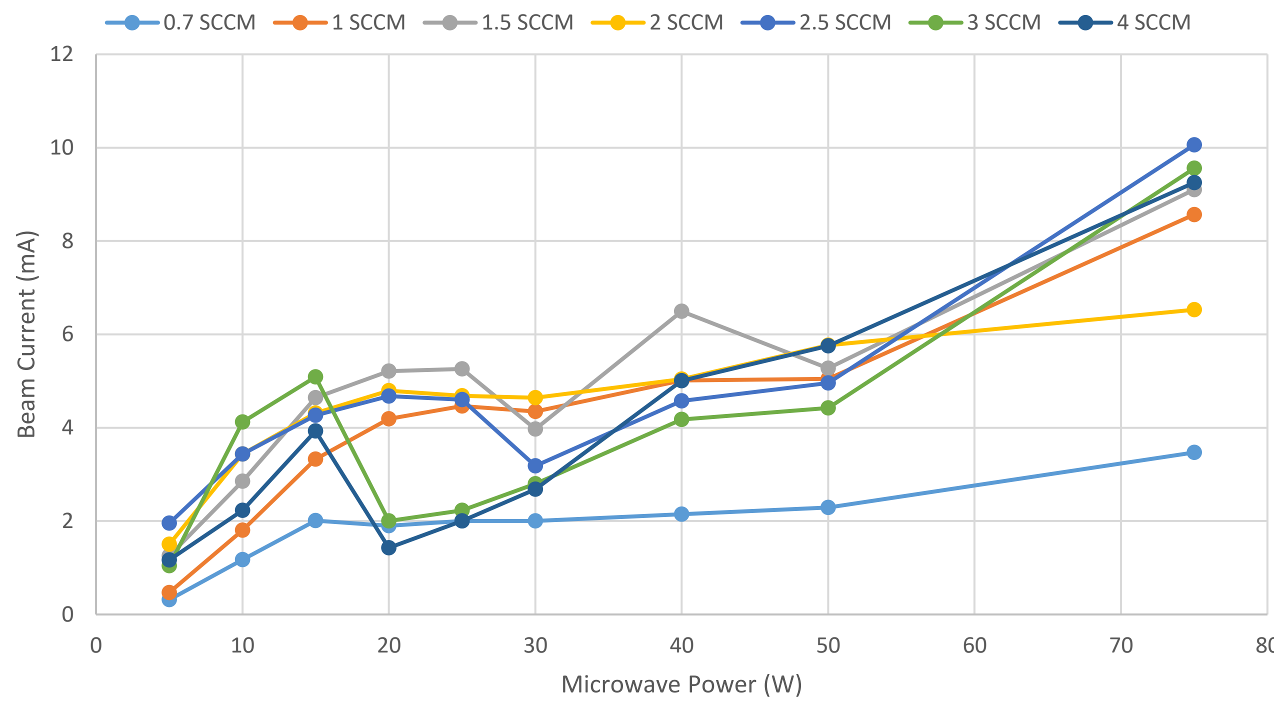

Figure 62 - The variation in beam current measured for varying flow rates

Continuing with the implications of the anode, Figure 63 shows the beam current has a strong dependence on the anode voltage with a clear quadratic relationship. This was an anticipated result as the greater potential of the anode would allow the electrostatic field to penetrate further into the chamber. This gives a greater proportion of the electrons in the plasma visibility of the electrostatic field. The stronger potential of this field would also attract a greater proportion of electrons.

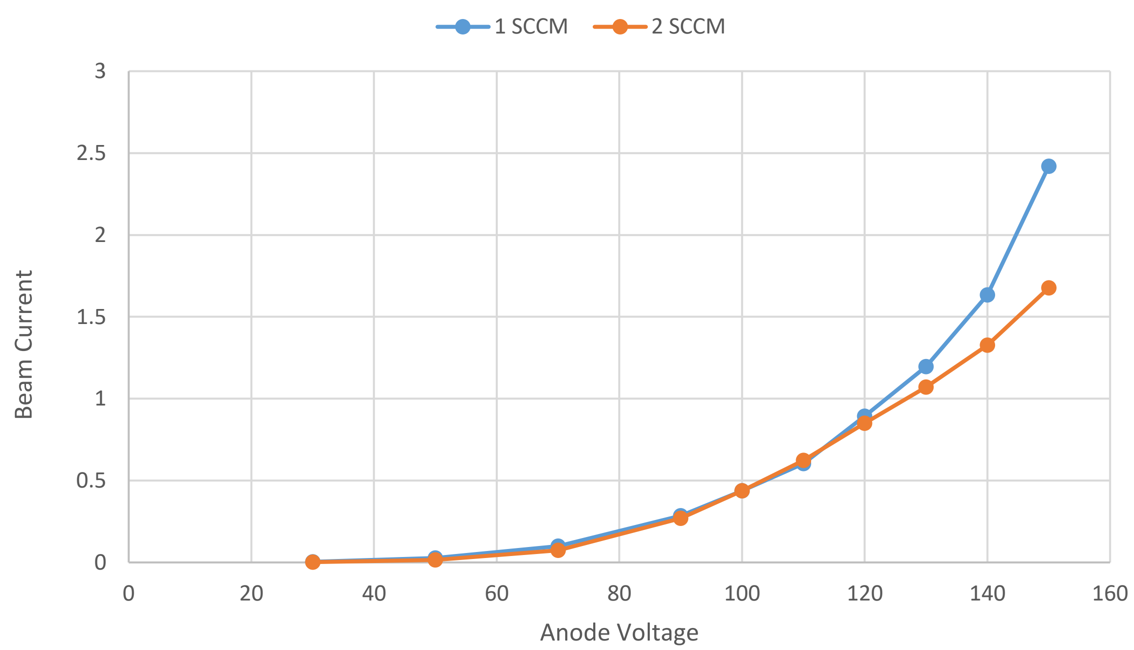

Figure 63 - The Effect of Anode voltage on Beam Current

Figure 62 presents an interesting result by looking at the effect of mass flow rate on the beam current. In general, the trends presented hold for all the mass flows tested. A recurring trend can be seen, with a rapid increase in beam current occurring between 0 – 15 W microwave power. This is followed by a period of relatively stable current between 20 and 50 W microwave power. Some fluctuations are seen in this region and it is believed this is due to instability of the 'plasma bridge' between the discharge chamber and anode in this transitional regime. With the operation now firmly in the plume mode, the increasing beam current continues between 50 – 75 W. This change in plasma mode is signalled by a sudden drop in current before then continuing to rise again. Interestingly this mode change seems to occur at lower microwave powers when at higher flow rates. The higher flow rate increases the total number density within the discharge chamber, meaning the likely hood of a collision occurring increases. Whilst the average energy of electrons is reduced due to the lower microwave power, it is believed that the increased number of collisions outweighs the effect of the lower average energy and as such the transition from flow to plume mode occurs earlier.

In general, the mass flow rate appears to have a relatively small effect on the measured beam current above a certain point (clearly 0.7 SCCM is inadequate). It is anticipated that with an improved design and increased ionisation rate, a greater distinction would be seen here. It is worth noting that a greater flow rate would be required to keep the plasma "fed" as more electrons are drawn out of the neutraliser in this case.

Transient Response

Figure 64 and Figure 65 present the transient response observed during testing. Both figures show a significant time for the beam current to stabilise after making a change to the input conditions. Notably, they show opposite trends, with the beam current tending to decrease from its initial value at higher microwave powers, while a steady climb is observed at lower powers. In the case of Figure 64, this is believed to be due to heating of the magnets at higher powers and, as described earlier, a shrinking of the ECR region leading to a steady decrease in the beam current. As the magnet temperature stabilises the ECR region stops shrinking and the current stabilises below the initial value.

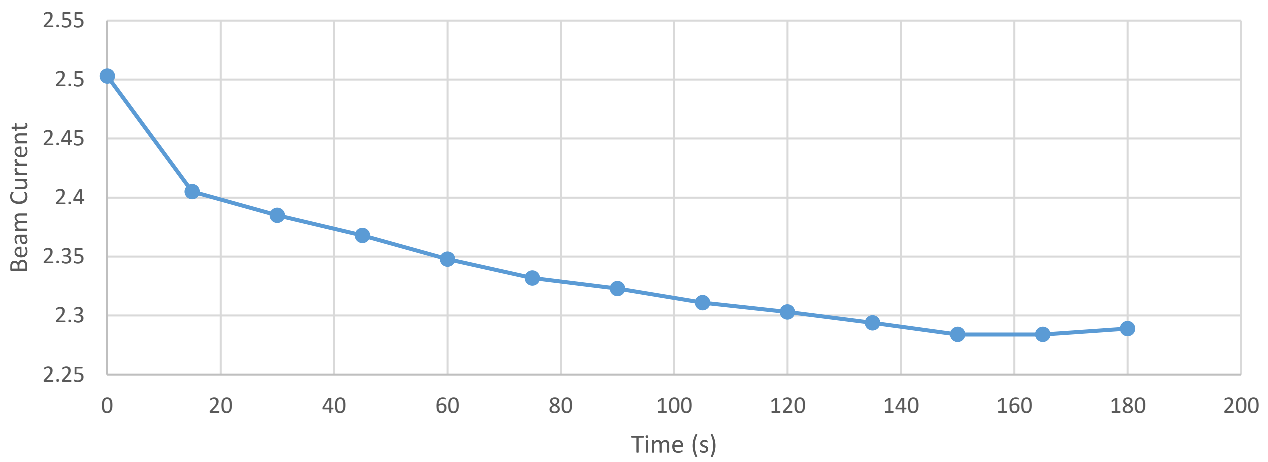

Figure 64 - 50 W Performance Drop Off – 0.7 SCCM

On the other hand, the increasing trend in Figure 65 can be explained by a different mechanism. At higher ionisation rates there is a greater proportion of primary electrons which are used to ionise neutral atoms, creating further thermal electrons which can then also undergo the resonance process, gaining energy and causing further collisions. As such the beam current steadily builds over time before levelling out at the equilibrium condition, when electrons are being drawn out and produced at the same rate. It is possible that at low currents, and hence low ion densities, a sheath could form across the orifice. This would shield the plasma inside the chamber from the electric field produced by the anode plate, and would limit

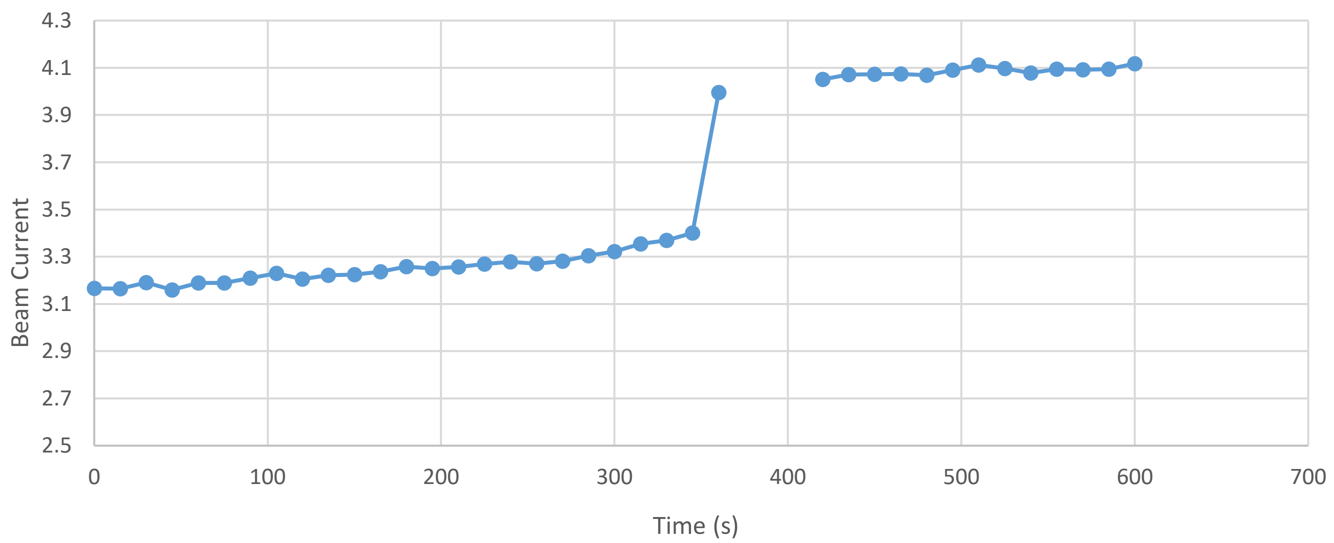

Figure 65 - 10W Performance Jump - 3 SCCM

maximum current. As the current and ion density gradually increase, this sheath reduces in size and at a certain point would stop covering the orifice, allowing the electric field produced by the anode to penetrate the chamber. It Is believed this could explain the sudden jump seen in Figure 65.

Observations

As well as taking direct measurements of the beam current, several visual observations were made using a mirror attached to the test setup, providing an excellent view of the orifice plate.

- Colour shift – Figure 66 shows a significant change in colour as the microwave power was increased while running at lower mass flow rates. This was associated with an increase in the proportion of double ionisations under these conditions.

- Flickering – On a different occasion it was noticed that the plasma varied between two distinct brightness levels but without a significant change in colour. The current also jumped between two distinct values in sync with this colour change. This is believed to be a repeated creation and breaking of the "plasma bridge". Increasing the microwave power by as little as 2 W removed the flickering with the brighter colour and higher current being sustained. On the other hand, decreasing the microwave power in a similar manner causes the plasma to stabilise in the lower intensity, lower current mode.

Figure 66 - A change in colour observed during testing with the cylindrical anode

Final Design Proposal

The final design proposal is displayed here, with an internal cut away showing the parts in place. The specification we set at the beginning of the project set out that:

- The Neutraliser should aim to produce a beam current of 1 Amp.
- The Neutraliser should be capable of integrating with the thruster design space.
- The Neutraliser should be designed to use argon as propellant.
- The Neutraliser's propellant flow rate should be minimised to reduce the impact on the overall specific impulse.
- The Neutraliser should be designed to operate with a microwave power supply of 2.45GHz.

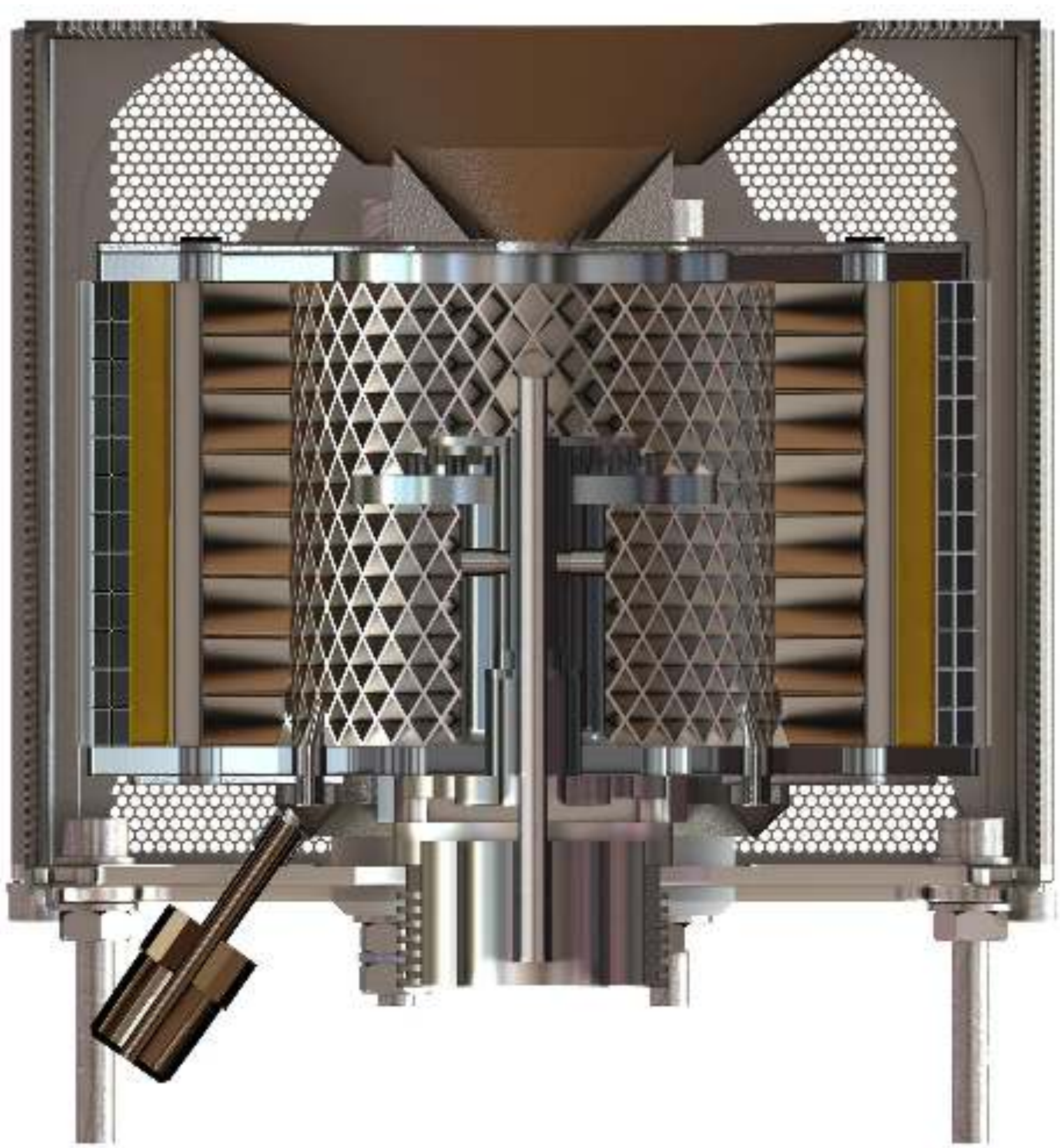

Final Mass	1743g
Final Dimensions (mm)	91.5 H x 109.35 W x 109.35 D
Final Cost (£) (material and component)	1715.14
Maximum Current (tested)	86.044 mA
Final Part count	12 Bespoke Designs 17 Bespoke Components (per configuration) 24 Bespoke Components Manufactured
Number of components additively manufactured	17
Propellant Flow @ Maximum Current	4 SCCM
Microwave Power @ Maximum Current	150 W

Beam Current Prediction Tool

This section presents an extension of the ECR performance characterisation developed for antenna design, bringing it closer to a comprehensive model of the entire neutraliser system. This is done through the use of the freely available BOLSIG electron Boltzmann equation solver [29], as a method of determining the average electron energy and the use of ionisation cross sections to relate this electron energy to the probability of an ionisation event occurring.

Based upon the same mesh as the ECR performance characterisation the average electron energy is determined based upon the reduced electric field strength (E/N) of the individual mesh element. A number of key assumptions had to be made for the method to apply:

- Magnetic and Electric field strength is constant within a mesh element
- Average Electron energy is constant within a mesh element
- 10% off-resonance condition
- Neutraliser is operating in a steady state
    - Ionisation Rate = Beam Current, i.e. electrons are being produced at the same rate they are being drawn from the neutraliser. Plasma density is constant.
    - Ionisation Rate = Ion recombination rate + Incoming flow rate, i.e. the plasma remains "fed" with sufficient neutral propellent atoms. Neutral Number Density remains constant.
- Neutral Number Density ≅ Total Number Density (Ion/Electron number density are orders of magnitude lower than Neutral number density)
- Only primary ionisation events occur (Ar^{+}), there is no further ionised states of Argon present (Ar^{2+})

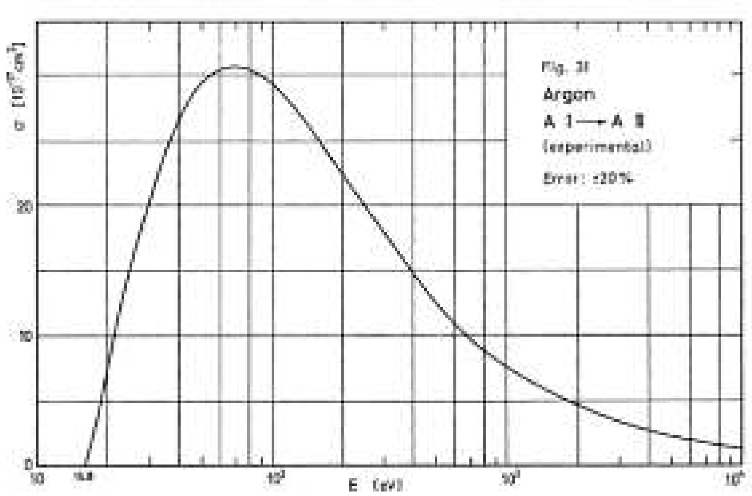

Figure 67 - Ionisation Cross-section of Argon [33]

Using freely available ionisation cross-section data [30], [31] the probability of an ionisation event can be determined based upon the average electron energy, shown in Figure 67, and hence this can be related directly to the ionisation rate. This calculation process is carried out within the BOLSIG solver and more details about how it works can be found in the journal paper it is based on [32]. In order to speed up computation, the relation between reduced electric field strength and ionisation rate coefficient was tabulated and linearly interpolated to find the rate coefficient for each mesh element, as opposed to running the solver for each element. This tabulated dataset is shown in Figure 68

The ionisation rate coefficient represents the number of ionising collisions a single primary electron undergoes during one second for a given neutral number density. In order to calculate the overall ionisation rate, the ionisation rate coefficient must first be multiplied by the neutral number density and the element volume, i.e. the total number of neutral propellent atoms within each mesh element. This is easily derived from the incoming flow rate and orifice back pressure. This then gives the number of ionising collisions caused by a single primary electron per second within the element. The final step is to sum these values for each mesh element and multiply by the electron number density, in order to arrive at the final ionisation rate. This can then be simply converted to beam current under the assumptions outlined earlier by multiplying by the fundamental charge.

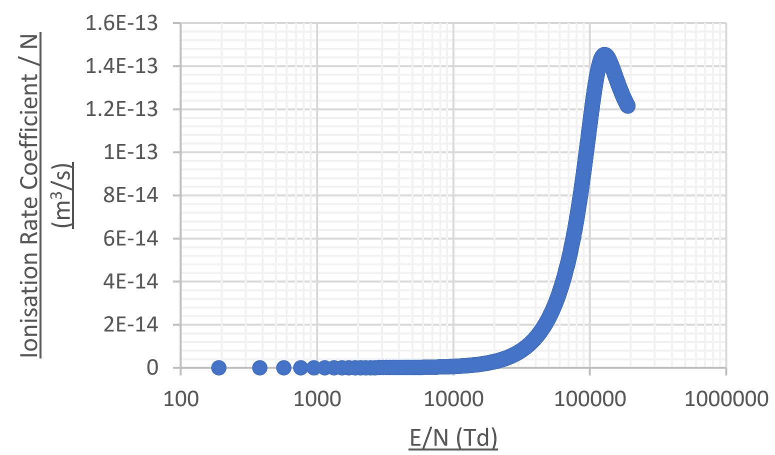

Figure 68 - Ionisation Rate coefficient Tabulation

Unfortunately, efforts to develop an analytical/theoretical method for determining the Ion/electron number densities within the plasma have not been successful. However, this data can be gathered experimentally using the method outlined in the discharge chamber section, using the measured beam current as opposed to the target current. For low currents, it is assumed that the discharge surface area appears as a solid wall as the low-density plasma cannot "see" inside the grid structure. For higher currents, the full surface area of the grid structure is considered. All our experimental measurements assumed the first of these methods.

The inclusion of a Langmuir probe within the test setup would also provide a method of measurement for these important parameters. It is envisaged that through further extensive testing, the relationship between the ECR performance characterisation and the ionisation fraction can be determined. This can be used to estimate the electron number densities for a range of configurations. This approach can then be used to characterise the performance of future designs over a range of operating conditions. Using different cross-section data, the method should also be expandable to include different propellent options such as Xenon. An example of the output can be seen in Figure 69.

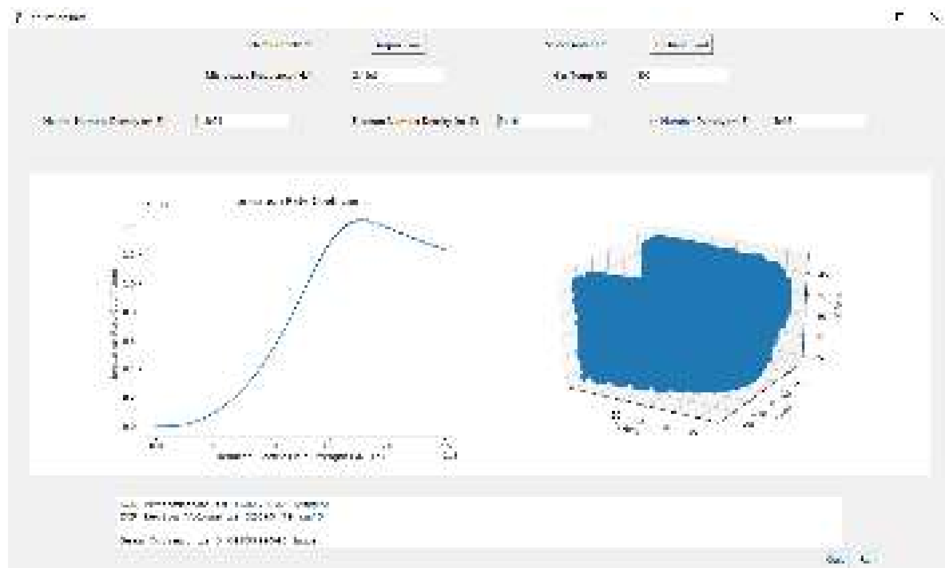

Figure 69 - GUI showing example result

Project Review

When the project began, the primary concern was reaching the testing phase and presenting an operational Neutraliser to verify our design.

Gaining insight into the issues with the thruster GDP project during the 2016/17 academic year allowed the team to identify areas of concern in the design process. Crucially, the most notable issue was manufacturing on time and to budget (Appendix B), which were taken into account within the project plan from the start. As the design process was broken into five distinct sections, each can be reviewed of its own accord.

Identifying research and understanding concepts

The first phase of the project ran smoothly, as demonstrated by the successful operation and testing of the Neutraliser. The challenge was attempting to conceptually understand the processes involved, without observing a physical model. Whilst this was not an option, it may have been beneficial in this stage to operate a hollow cathode in the vacuum chamber to fully appreciate the limitations of the component we were designing a replacement for. Whilst the application of the Microwave Neutraliser has been well considered, understanding the limitations of a hollow cathode from physical experience may have been beneficial. Additionally, during this phase the understanding the physics involved in plasma generation, particularly with the team coming from an exclusively aerospace/spacecraft systems engineering background. This made some concepts challenging to learn with enough depth in order to implement them effectively in the design, early in the project. The collective understanding of the processes involved has developed over the course of the project however an increase in prior understanding would be useful.

Requirements and new approaches

The requirements were set out indirectly by the design decisions taken in the 2016/17 project, which outlined the thruster specifications. This meant the design was set for propellant choice, microwave power and size. This worked well as it enabled design to progress quickly by setting the design specifications early. The Microwave power supply installed for this project was custom manufactured to specification and decided prior to the start of the project, such that the 2.45GHz frequency was a specification that had to be met. The neutraliser geometry allowed more design freedom, and utilising additive manufacture allowed for a novel solution to increase the surface area within the discharge chamber.

Design, Simulate and Analyse

It was set out in the early stages of the project that the designs would be submitted before the Christmas break in anticipation of the large lead times incurred by high demand for additive manufacturing in the EDMC. This resulted in a design and simulation period of around 8 weeks during the first semester to allow time for review prior to submission. As a result, the detail of analysis was limited, as was the number of cycles through the design process. If submission for manufacture had not been made prior to Christmas, the Neutraliser would not have been completed in time for the testing slot, because of manufacturing delays beyond our control. It is a trade-off that had to be made early in the project to reach testing.

Manufacture, Assembly and Test

As anticipated, manufacture took a significant amount of time. Submission was made to the EDMC on the 16th of December, with enough parts available to assemble for testing by the 16th of March. Despite a significant proportion of the project plan assigned to manufacture with the inclusion of overruns, manufacturing time was significantly extended due to a change in printing material and maintenance problems. When components were received back, small amounts of further machining were required (tapping and finishing), however the review prior to submission for manufacture had been worthwhile as the final assembly was completed as intended on the first attempt without issue. Testing was confined to the booking within the vacuum chamber during the first two weeks of April. An additional delay in the installation of the microwave power supply pushed the first test back by an additional week, however, this did allow time to assemble the neutraliser on the test rig with the ground support equipment attachments. This allowed commissioning of the microwave supply to occur using the Neutraliser as a test piece to tune the supply, with ignition occurring shortly after. Because of the unknown behaviour of the neutraliser ignition and operation, progressive updates were made to the testing scheme as the operation was better quantified.

Identify improvements

The continual testing of the neutraliser with a series of interchangeable components allowed better prediction of the operational behavior and verification of the models. Testing of the different antenna shapes confirmed the ignition powers for each, and the current data obtained for a range of potentials, microwave powers and flow rates allowed assumptions in early modelling to be corrected and updated.

There are a number of recommendations that have been made for each component, and further developments to improve the performance of the existing neutraliser, or design a new iteration implementing the models developed using experimental data from this project.

Further development

Having completed one iteration of the design phase and reached testing, we are well placed to provide developments and further recommendations.

The first recommendation is to pick up directly from where this project leaves off. Because of the number of components that can be interchanged, and the external variables; microwave power, flow rate and anode voltage, there are many weeks' worth of testing still required to fully realise the potential of the neutraliser.

Secondly, it would be worthwhile modifying the interior of the second discharge chamber to increase the spacing between the fins or remove them entirely. Comparing this with the existing chamber would allow a better understanding of the processes occurring in the chamber and identifying the true ion number density. In doing so, it would serve to inform further development of an updated discharge chamber. Further development would involve developing a sheath-size model to provide a more accurate representation of the size of the sheath at a given ion density. This may involve making estimates of plasma potential, which should be done for both the original expected operating range and the estimates of ion density derived from test results. This will help further optimise the chamber design and gauge whether the original 'Debye length x 20' estimate, made in the original design, was valid. Important insights into the behaviour of the plasma could be gained from the use of testing with a Langmuir probe. This could provide more accurate results for experimental ion density, plasma potential and Electron Temperature, all of which would allow for updates to the chamber design based on real recorded data, rather than assumptions. It may also be worthwhile re-designing variations of the chamber to produce 250-500 mA, to see if this could be achieved with the maximum estimates of ion density from our results.

Developing a full 3D simulation of Electric Field penetrations through the orifice and into the chamber, overlaid with the ECR model, would give a better insight into how the external anode and orifice size affects the motion of electrons inside the chamber. This could be done as a simpler collision-less model, or a Monte-Carlo simulation including collision probabilities between electrons and ions. A full Monte-Carlo simulation may also garner further insight into potential ionisation rates in the neutraliser and is a step closer to a complete model of the entire neutraliser system. A 3D CFD model showing pressure distributions through our final design, given different mass flows, may give insight as to why the system is not behaving quite as expected.

By extension, there is concern that a significant amount of propellant is leaking from around the reservoir plate, which may be limiting the pressure in the chamber and therefore the performance of the neutraliser. It may be beneficial performing flow analysis tests on the isolated propellant injection system, to ensure there is no significant leakage through the threaded interface between nozzles and reservoir plate. It would also be beneficial to take pressure readings inside the neutraliser at differing flow rates, to verify the flow model and assess the impact of general leakage from the discharge chamber that may be affecting performance. Ultimately this is more challenging but would allow improved data for future modelling.

Due to budget restrictions, it was not possible for this project to use bespoke annular ring magnets for the creation of the magnetic field. Use of these in future iterations would remove the additional structure used around the discharge chamber, for mounting arrays of magnets, therefore decreasing the mass of the system. The depth of these ring magnets could also be decreased compared to the current arrays of magnets used, due to the complete coverage around the outside of the discharge chamber that these would provide. Both these factors would allow a bigger discharge chamber volume, in turn allowing a larger ECR region and increased area for ion recombination. The use of bespoke magnets with an increased remnant flux density would allow for smaller iron yokes to be employed. By having a smaller main yoke, the distance between the yokes could be increased and therefore the ECR surface area would increase. Without stronger magnets, this is not possible without holes forming in the surface.

There is scope for antenna improvements with a well-designed star shape, as this has been proven by other research as a viable consideration. The ignition of all three antennas demonstrated that the modelling was correct and further research could be carried out. In testing, connecting the Microwave power supply to a computer to allow more precise control would be beneficial when testing low power ranges, due to the low resolution of the dial control. Finally, an improved thermal material around the antenna would allow higher power operation, which may provide a further increase in neutralisation current.

A more accurate thermal analysis could be carried out using better estimates for temperature in the ECR region and thermal input from the microwave power source. This could potentially be done by using a plasma physics software such as Starfish or PTSG to calculate the temperature of the neutral gas in the discharge chamber at a range of microwave powers. An improved thermal insulation such as Microtherm would allow for continuous operation at higher microwave input power. Microtherm was not selected initially due to cost constraints, which led to the use of Calcium Magnesium Silicate sheet. Further investment in the project could allow for more appropriate material to be used in future iterations. Finally, the addition of insulation between each yoke and the magnet arrays would assist in temperature regulation of the magnets.

Across all components, cutting out unnecessary mass makes the ECR neutraliser far more attractive as an alternative to hollow cathodes in future electric propulsion systems. Many components were designed and manufactured for operation, and components such as the orifice plate, reservoir plate and yokes could afford significant reductions in thickness and volume, also bringing the cost per part down. The neutraliser faraday cage could be designed to accommodate both the thruster and neutraliser, whilst the incorporation of annular magnets would also offer additional reductions. To do this effectively would require the construction of a structural model for testing, to verify simulations and design iterations. Certain components, such as the ceramic spacers would be unsuitable for this, as it was found that overtightening of these would result in cracking.

These recommendations offer several changes and iterative updates over the current model, that would make the project worthwhile continuing and developing further. There is enormous potential, we hope that it is fully explored.

Bibliography

[1] A. C. Clarke, "Extra-Terrestrial Relays," *Wireless World,* pp. 305-308, October 1945.

[2] C. d. Dorides, "Towards a more connected society and economy," The Parliament Magazine, 19th January 2018. [Online]. Available: https://www.theparliamentmagazine.eu/articles/opinion/towards-more-connected-society-and-economy. [Accessed 10th May 2018].

[3] SpaceX, "Merlin Engines," SpaceX, 31st August 2015. [Online]. Available: http://www.spacex.com/news/2013/03/26/merlin-engines. [Accessed 10th May 2018].

[4] NASA, "Space Shuttle Main Engines," 16th July 2009. [Online]. Available: https://www.nasa.gov/returntoflight/system/system_SSME.html. [Accessed 10th May 2018].

[5] ABS, "ABS-3A," 2018. [Online]. Available: http://www.absatellite.com/satellite-fleet/abs-3a/. [Accessed 10th May 2018].

[6] ESA, "GOCE," [Online]. Available: http://www.esa.int/Our_Activities/Operations/GOCE. [Accessed 10th May 2018].

[7] NASA, "NASA - Ion Propulsion," 7th August 2017. [Online]. Available: https://www.nasa.gov/centers/glenn/about/fs21grc.html. [Accessed 10th May 2018].

[8] D. M. Goebel and I. Katz, "Fundamentals of Electric Propulsion: Ion and Hall Thrusters," March 2008. [Online]. Available: https://descanso.jpl.nasa.gov/SciTechBook/series1/Goebel__cmprsd_opt.pdf. [Accessed 11th May 2018].

[9] J. E. Foster and M. J. Patterson, "Discharge Characterization of 40cm-Microwave ECR Ion Source and Neutralizer," in *39th Joint Propulsion Conference*, Huntsville, 2003.

[10] D. M. Goebel, I. Katz, J. Polk, I. G. Mikellides, K. K. Jameson, T. Liu and R. Dougherty, "Extending Hollow Cathode Life for Electric Propulsion in Long-Term Missions," in *Space 2004 Conference and Exhibit*, San Diego, 2004.

[11] H. Kuninaka, K. Nishiyama, Y. Shimizu, I. Funaki, H. Koizumi, S. Hosoda and D. Nakata, "Hayabusa Asteroid Explorer Powered by Ion Engines on the way to Earth," in *International Electric Propulsion Conference*, Ann Arbor, 2009.

[12] P. Fortescue, G. Swinerd and J. Stark, Spacecraft Systems Engineering, Chichester: Wiley, 2011.

[13] P. B. de Selding, "Eutelsat, ESA Taking a 'Quantum' Leap Toward Fully Software-defined Satellite," Space News, 9th July 2015. [Online]. Available: http://spacenews.com/eutelsat-esa-taking-a-quantum-leap-toward-fully-software-defined-satellite/. [Accessed 11th May 2018].

[14] I. Funaki, K. Nishiyama, H. Kuninaka, K. S. Y. Toki and H. Toki, "20mN-class Microwave Discharge Ion Thruster," in *27th International Electric Propulsion Conference*, Pasadena, 2001.

[15] K. Gibbs, "Motion in magnetic and electric fields," School Physics, 2016. [Online]. Available: http://www.schoolphysics.co.uk/age16-19/Atomic%20physics/Electron%20physics/text/Electron_motion_in_electric_and_magnetic_fields/index.html. [Accessed 7th May 2018].

[16] H. Kuninaka, K. Nishiyama, I. Funaki, S. Y., Y. T. and K. J., "Assessment of Plasma Interactions and Flight Status of the HAYABUSA Asteroid Explorer Propelled by Microwave Discharge Ion Engines," *IEEE Transactions on Plasma Science,* vol. 34, no. 5, pp. 2125-2132, 2006.

[17] N. Beena, B.-T. J, L. Calnan, T. Cockerill, S. Curtis, A. Fforde and Z. Llamas, "Argon Electron Cyclotron Resonance Gridded Ion Thruster," University of Southampton, Southampton, 2017.

[18] MIT OpenCourseWare, "Overview of the physics in the plasma sheath," 2015. [Online]. Available: https://ocw.mit.edu/courses/aeronautics-and-astronautics/16-522-space-propulsion-spring-2015/lecture-notes/MIT16_522S15_Lecture9.pdf. [Accessed 15 May 2018].

[19] P. Chabert, "What is the size of a floating sheath," *Plasma Sciences and Technology,* vol. 23, no. 26, 2014.

[20] A. D. Herman and A. D. Gallimore, "An ion thruster internal discharge chamber electrostatic probe diagnostic technique using a high-speed probe positioning system," *Review of Scientific Insturments,* vol. 79, no. 1, 2008.

[21] R. Fitzpatrick, "Magnetic Mirrors," University of Texas, 31 03 2011. [Online]. Available: http://farside.ph.utexas.edu/teaching/plasma/Plasmahtml/node21.html. [Accessed 7th May 2018].

[22] H. Kuninaka, S. Satori, I. Funaki, Y. Shimizu and K. Toki, "ENDURANCE TEST OF MICROWAVE DISCHARGE ION THRUSTER SYSTEM FOR ASTEROID SAMPLE RETURN MISSION MUSES-C," in *International Electric Propulsion Conference*, Cleveland, 1997.

[23] N. Yamamoto, H. Kataharada, T. Chikaoka, H. Masui, H. Nakashima and Y. Takao, "Effect of Antenna Configuration on Thrust Performance in a Miniature Microwave Discharge Ion Engine," in *International Electric Propulsion Conference*, Princeton, 2005.

[24] Y. Ke, X. Sun, X. Chen, L. Tian, T. Zhang, M. Zheng, Y. Jia and H. Jiang, "Analysis of the primary experimental results on a 5 cm diameter ECR ion thruster," *Plasma Science and Technology,* vol. 19, no. 9, 2017.

[25] P. Roychowdhury, L. Mishra, H. Kewlani and S. Gharat, "Hydrogen Plasma Characterization at Low Pressure in 2.45 GHz Electron Cyclotron Resonance Proton Ion Source," *IEEE Transactions on Plasma Science,* vol. 45, no. 4, pp. 665-671, 2017.

[26] L. A. Berry and S. M. Gorbatkin, "Electron cyclotron resonance microwave ion sources for thin film processing," in *International Conference on the Application of Accelerators in Research and Industry*, Denton, 1990.

[27] S. Samukawa and T. Nakamura, "Dependence of Electron Cyclotron Resonance Plasma Characteristics on Magnetic Field Profiles," *Japanese Journal of Applied Physics,* vol. 30, no. 11B, pp. 3147-3153, 1991.

[28] RS Components, "Calcium-Magnesium Silicate Thermal Insulating Sheet, 2 m x 610 mm x 4 mm," [Online]. Available: https://docs-emea.rs-online.com/webdocs/1581/0900766b815817e4.pdf. [Accessed 15 May 2018].

[29] G. Hagelaar, "BOLSIG+," 2018. [Online]. Available: https://www.bolsig.laplace.univ-tlse.fr/. [Accessed 17 May 2018].

[30] Y. C, S. J. Buckman and A. V. Phelps, "Measurement of free-free emission from low-energy-electron collisions with Ar," *Physical Review,* vol. 27, no. 3, p. 1345, 1983.

[31] LxCat, "Data Center," 2018. [Online]. Available: http://www.lxcat.laplace.univ-tlse.fr. [Accessed 17 May 2018].

[32] G. J. M. Hagelaar and L. C. Pitchford, "Solving the Boltzmann equation to obtain electron transport coefficients and rate coefficients for fluid models," *Plasma Sources Science Technology,* vol. 14, pp. 722-733, 2005.

[33] W. Lotz, "Electron-Impact Ionization Cross-Sections and Ionization Rate Coefficients for Atoms and Ions," *Astrophysical Journal Supplement,* vol. 14, pp. 207-238, 1967.

Acknowledgements

The team would like to thank:

Dr Angelo Grubisic, for supervising the project with unparalleled enthusiasm and passion, and his guidance in taking the project from concept to reality.

Dr Min Kwan Kim, for assisting in supervision of the project, and significant assistance in plasma modelling and dynamics.

David Hoffman, for his patience and time working with the team to successfully develop the thruster and neutraliser assembly.

Kepston Ltd for their generous contribution towards the heat treatment of the main yoke and ring yoke.

The EDMC for their patience and skill with our designs and producing components of outstanding quality.

Mike Pollard (IP 2016/17) for the research provision his project enabled.

The GDP of 2016/17, for getting the Gridded Ion Thruster project off the ground and facilitating the progress this project has achieved.

Appendix A – Project Plan

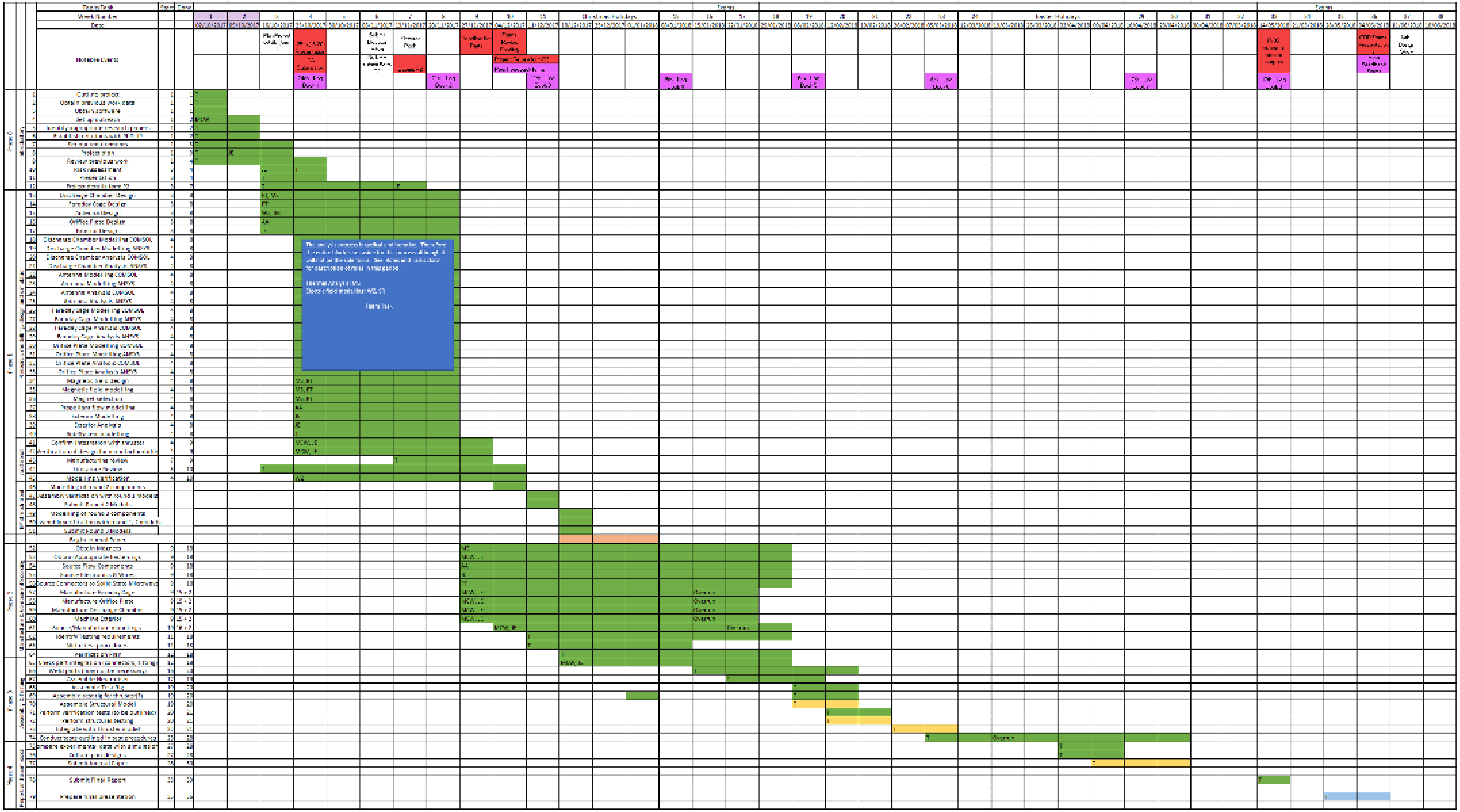

Appendix B – Budget Spreadsheet

Item	Description	Manufacturer	Supplier	Unit cost (£)	# Of	Total Cost (£)	Unit cost (£)	# Of	Total Cost (£)
NEUTRALISER				MATERIAL			TECHNICIAN		
1	Discharge chamber (48mm)	EDMC	EDMC	109,00	1	109,00	150,00	1	150,00
2	Discharge chamber (54mm)	EDMC	EDMC	122,36	1	122,36	150,00	1	150,00
3	Antenna (L)	EDMC	EDMC	10,00	1	10,00	30,00	1	30,00
4	Antenna (3 point star)	EDMC	EDMC	31,00	1	31,00	150,00	1	150,00
5	Antenna (6-point star)	EDMC	EDMC	31,00	1	31,00	150,00	1	150,00
6	Orifice plate 6mm	EDMC	EDMC	37,00	1	37,00	150,00	1	150,00
7	Orifice plate 7mm	EDMC	EDMC	37,00	1	37,00	150,00	1	150,00
8	Orifice plate 8mm	EDMC	EDMC	37,00	1	37,00	150,00	1	150,00
9	Main yoke + ring yoke (+treatment)	Tennant Metallurgic Group	KEPSTON Limited	633,60	-	633,60	1600,00	1	1600,00
10	Propellant inlet reservoir	EDMC	EDMC	37,00	1	37,00	150,00	1	150,00
11	Propellant inlet nozzle	EDMC	EDMC	-	4	35,00	150,00	1	150,00
12	Neobdymium Magnets	-	-	-	-	113,36	-	-	-
-	-	-	-	ASSEMBLY MATERIAL COST (£)		1233,32	ASSEMBLY TECHNICIAN COST (£)		2980,00
FARADAY CAGE				MATERIAL			TECHNICIAN		
13	Faraday cage base	EDMC	EDMC	230,00	1	230,00	150,00	1	150,00
14	Faraday cage face	EDMC	EDMC	-	3	56,00	150,00	3	150,00
15	Faraday cage face plaque	EDMC	EDMC	36,00	1	36,00	150,00	1	150,00
16	Faraday cage backplate	EDMC	EDMC	10,00	1	10,00	320,00	1	320,00
-	-	-	-	ASSEMBLY MATERIAL COST (£)		332,00	ASSEMBLY TECHNICIAN COST (£)		770,00
OFF-THE-SHELF				MATERIAL			TECHNICIAN		
17	Ceramic Bush Male	Lewvac	Lewvac	-	8	-	-	-	-
18	Ceramic Bush Female	Lewvac	Lewvac	-	10	11,00	-	-	-
19	M3x30 Hex Socket Bolt	Orbital Fasteners	Orbital Fasteners	-	4	0,05	-	-	-
20	M4 Washer	Orbital Fasteners	Orbital Fasteners	-	16	0,04	-	-	-
21	M4 Nut	Orbital Fasteners	Orbital Fasteners	-	12	0,04	-	-	-
22	M4 x 80 Hex Socket Bolt	Orbital Fasteners	Orbital Fasteners	-	4	7,70	-	-	-
23	M4 x 30 Hex Socket Bolt	Orbital Fasteners	Orbital Fasteners	-	4	0,92	-	-	-
24	PTFE Sleeve	-	-	-	2	7,65	-	-	-
26	PTFE Rod	-	-	4,00	1	4,00	-	-	-
27	Insulation	-	RS	-	1	74,00	-	-	-
28	M3x25 Bolts	Orbital Fasteners	Orbital Fasteners	-	4	0,04	-	-	-
29	Swagelok SS-2-TA-1-2 Fitting	Swagelok	Swagelok	-	1	5,10	-	-	-
30	Coaxial Port	Telegärtner	Karl Garntner GMBH	19,64	2	39,28	-	-	-
-				COST OF COMPONENTS (£)		149,82	-		
				TOTAL MATERIAL COST (£)		1715,14	TOTAL TECHNICIAN COST (£)		3750,00